AN ANALYSIS OF THE AERODYNAMICS OF A FIBER OPTIC MORTAR PROJECTILE

by

Edward A. Robertson

Thesis submitted to the Faculty of the
Virginia Polytechnic Institute and State University
in partial fulfillment of the requirements for the degree of

MASTER OF SCIENCE

in

Aerospace Engineering

APPROVED:

James F. Marchman, III, Chairman

Eugene M. Cliff

Dana A. Walker

April, 1989

Blacksburg, Virginia

AN ANALYSIS OF THE AERODYNAMICS OF A FIBER OPTIC MORTAR PROJECTILE

by

Edward A. Robertson

James F. Marchman, III, Chairman

Department of Aerospace Engineering

(ABSTRACT)

In December of 1987 tests were conducted in the Virginia Tech Stability Wind Tunnel on a full-scale model of a fiber optic mortar projectile. The desired model configurations were sting-mounted on the Stability Tunnel STO-1 strain gauge balance. The sting was mounted on a streamlined vertical pylon which provided remote rotation in both pitch and yaw while maintaining the center of the balance along the tunnel centerline. The model inputs included the six-component force and moment data in body coordinates and the pressure data from the five pressure taps located within the model. The tunnel inputs were the static temperature, static pressure and dynamic pressure. The angle of attack and yaw angle were input manually by the tunnel operator. The data analysis for the preliminary test program was intended to define the aerodynamic qualities of various components and configurations to aid in the redesign of the projectile.

ACKNOWLEDGEMENTS

I would like to thank the skilled men in the workshop for their aid in fulfilling the requests of the professors for various laboratory classes.

Frank, Joe and Kent

I would also like to acknowledge the abilities of fellow graduate student, Subrahmanyam Kuppa, and the wind tunnel engineering technician, Greg Bandy. Without their support the aerodynamic research might never have been completed.

Finally, special thanks to Dr. James F. Marchman, III, Dr. Eugene M. Cliff and Dr. Dana A. Walker, the members of my graduate committee.

TABLE OF CONTENTS

LIST OF FIGURES

LIST OF FIGURES (continued)

LIST OF FIGURES (continued)

TABLE OF REFERENCE DATA

Small Fins (F1):

Sref	=	0.1166 sq. ft.	Total planar surface area (4 fins)
Asurf	=	0.4667 sq. ft.	Total wetted surface area (4 fins)
c	=	1.40 inches	Chord
b	=	10.70 inches	Total fin span
Re	=	156,000	Chord Reynolds number

Large Fins (F2):

Sref	=	0.3412 sq. ft.	Total planar surface area (4 fins)
Asurf	=	1.3650 sq. ft.	Total wetted surface area (4 fins)
c	=	2.486 inches	Geometric mean chord
b	=	14.60 inches	Total fin span
Re	=	279,000	Chord Reynolds number

Wings:

Sref	=	1.1614 sq. ft.	Total planar surface area (4 wings)
Asurf	=	4.6453 sq. ft.	Total wetted surface area (4 wings)
c	=	2.504 inches	Geometric mean chord
b	=	38.12 inches	Total wing span
b*	=	33.40 inches	Span with body diameter deducted
Re	=	278,000	Chord Reynolds number
AR	=	13.34	Aspect ratio (based on b*)

TABLE OF REFERENCE DATA (continued)

Body:

Aref	=	0.1215 sq. ft.	Area of body cross section
Dref	=	4.72 inches	Body reference diameter
Re	=	525,000	Reynolds number based on diameter

Tunnel:

q	=	11.40" H2O	Reference dynamic pressure
V	=	235 ft/sec	Flow velocity

INTRODUCTION

In December of 1987 tests were conducted in the Virginia Tech Stability Wind Tunnel on a full-scale model of a fiber optic mortar projectile. The tests were conducted by Subrahmanyam Kuppa and Edward A. Robertson, graduate students in the college of Aerospace Engineering, under the supervision of Dr. James F. Marchman III, Professor of Aerospace Engineering and Director of the Stability Wind Tunnel. Greg Bandy, the wind tunnel engineering technician, and two undergraduate students in Aerospace Engineering assisted in the testing.

STABILITY WIND TUNNEL

The Virginia Tech Stability Wind Tunnel (Figure 1) is a closed-circuit, continuous flow, subsonic testing facility. Flow impetus is produced by a five-bladed, fourteen-foot diameter propeller driven by a six-hundred horsepower DC electric motor. The flow passes from the propeller through an air exchange tower which moderates the effects of fan pressure pulses in the test section. The air exchange tower also provides an atmospheric total pressure reference. Prior to entering the test section the flow encounters seven steel anti-turbulence screens. The fine, square-mesh screens produce a uniform test section flow with low free

stream turbulence. The tunnel is equipped with several interchangable test sections which provide versatility by allowing variations in model mounting techniques and air flow conditions. The test section used in the fiber optic mortar projectile (FOMP) experiment has a six-foot square cross section with twenty-two feet of useful testing length. With this test section the capability exists to generate curved flow pressure gradients. For the FOMP tests, however, the walls were adjusted to provide uniform, straight flow. The test section is equipped with a round, plexiglas window which allows the tunnel operator to view the model from the control center. Several fluorescent fixtures mounted on plexiglas ceiling panels illuminate the test section.

The Virginia Tech Stability Wind Tunnel is capable of generating a flow with a maximum Reynolds number per foot of 1,330,000. Under standard atmospheric conditions the corresponding maximum test velocity is approximately 175 miles per hour.

MODEL DESCRIPTION

The FOMP model had a cylindrical main body divided into six sections. From fore to aft these sections were the nose, the forebody connector, the wing slot section, the

aftbody connector, the fin slot section and the fiber optic bobbin. The wings and fins were attached with machine screws to the body. A photograph of the fully configured model is provided in Figure 2.

The model body was designed in sections to allow the simulation of various configurations encountered in a launch and flight sequence. The FOMP sequence starts with a mortar launch with the wings and fins confined within the smooth, cylindrical body. Shortly after launch, the fin slot cover is jettisoned and four fins rotate and lock into flight position to provide longitudinal stability. The fins are actuated to allow pitch, yaw and roll control during the climb and attack phases.

At the end of the climb phase the wing slot cover is jettisoned and the set of four wings is deployed. In the attack phase the wings produce the majority of the lift forces required for high-acceleration targeting maneuvers. The attack phase is completed when the projectile impacts with the intended target.

During its flight the FOMP trails an optic fiber that carries targeting information from the projectile to the base station. The base station returns commands to the fin actuators along the optic fiber. Locating the targeting computer in a reusable launch platform reduced the

complexity and cost of the FOMP design as compared to an autonomous projectile design. Each self-guided projectile would require a separate computing module shielded from vibrations and electronic countermeasures.

The design of the projectile nose involved both optical and aerodynamic considerations. The nose is intended to be the window for the detection of targeting data by receptors housed in the nose and forebody. An increase in the radius of curvature of the nose would reduce the lens distortion of the optical signals. But aerodynamic considerations favor a nose with a relatively small radius of curvature to minimize the generation of drag in the high-pressure stagnation region.

In order to determine the aerodynamic effects of a variation in the radius of curvature, two noses were tested. One nose had a hemispherical shape with a 2.36-inch radius of curvature (Figure 3a). Designated the 2.36" nose, its profile blended smoothly with the forebody connector. The other nose had a 3.00-inch radius of curvature frontal surface intersecting a cylindrical section that mated with the forebody connector (Figure 3b). Designated the 3.00" nose, it was chosen to be the baseline nose for the FOMP tests. The two noses were designed to be interchanged without affecting the total body length.

The forebody connector was a simple cylinder of length 11.75 inches that joined the nose with the wing slot section (Figure 4). The diameter of 4.72 inches shown in Figure 4 was the standard outer diameter for all body components in the cylindrical launch configuration. Besides providing the proper spacing between the nose and the wing slot section, the volume within the forebody connector was intended to house optical reception equipment, wing deployment apparatus and any additional payload.

The wing slot section was modeled by two separate components to reflect the changes in the FOMP body configuration during the flight sequence. One component was a simple cylindrical section of length 14.20 inches designed to represent the shell that encloses the wings during the launch and climb phases (Figure 5a). Configurations using the cylindrical section were designated "wing slots covered" (WSC). The other component represented the wing slot section in the attack phase, after wing deployment (Figure 5b). In the wing slot region the component had a square cross section with sides of approximately 3.42 inches in length. Configurations using the post-deployment section were designated "all slots open" (ASO). The FOMP model was tested extensively in both WSC and ASO configurations to determine the variations in the aerodynamic performance of

the body during the flight sequence.

The length of the wing slot section limited the span of the wings to approximately twenty-five inches using a standard wing design. In order to achieve a longer wing span a collapsible wing design was created with a spring-loaded tip section sliding from the interior of the root section. The collapsible wing was modeled using a solid aluminum wing with a root chord of 2.625 inches and a tip chord of 2.300 inches (Figure 6). When deployed the total wing span was 38.12 inches with a root section span of 24.88 inches. Both the root and the tip sections had a rectangular planform with a NACA 0012 airfoil section. The wing had no taper, sweep or twist. The chord of the wing was aligned with the longitudinal body axis.

The aftbody connector was a cylindrical section 10.63 inches in length similar in design and purpose to the forebody connector (Figure 7). The aftbody connector joined the wing slot section with the fin slot section. In the flight design the forebody connector provides space for fin deployment and actuating equipment.

The fin slot section was modeled by a single component representing the post-fin deployment stage (Figure 8). Because the fins are deployed a short time after launch and because no trim control is available before fin deployment,

it was decided that the benefits of including a cylindrical "fin slots covered" section were overshadowed by the increase in the cost and complexity of the test matrix. The fact that the fin slots were open for all of the tests explains the use of the WSC and ASO designations for the FOMP slot status.

Two sets of control surfaces were tested in order to determine the trim requirements of the FOMP. The small fins, denoted F1, were designed to fit within the fin slot section without resorting to a complex collapsible design (Figure 9a). The small fins had a chord of 1.40 inches and a span of 10.70 inches. The large fins, denoted F2, employed a collapsible construction identical in nature to the sliding wing design with a root chord of 2.60 inches and a tip chord of 2.30 inches (Figure 9b). Using the collapsible design, the fin slot section was able to accomodate a total fin span of 14.60 inches. Both fin designs utilized a NACA 63-015 airfoil section and had a rectangular planform with no sweep, taper or twist. The airfoil chord was aligned with the body longitudinal axis at zero fin deflection using a reference tab on the fin slot section. Alignment grooves were machined into the base of the fin to provide precise four-degree increments of fin deflection from minus sixteen to plus sixteen degrees. A

positive fin deflection was defined as clockwise as viewed from the tip.

The final component of the FOMP model was the fiber optic bobbin. It consisted of a spool, around which the optic fiber was wound, and a protective shell. Two bobbin designs were tested in order to determine the effects of bobbin length on FOMP aerodynamics. The long bobbin, designated B1, was 13.25 inches in length (Figure 10a). It employed a proven tapered spool design resulting in a total model length of 55.0 inches. The short bobbin, designated B2, was only 8.25 inches in length (Figure 10b). Its flat spool design provided the same optic fiber storage space as the long bobbin, but resulted in a total model length of 50.0 inches. Both bobbin designs are capable of storing approximately five kilometers of optic fiber.

EXPERIMENTAL PROCEDURE

Wind tunnel tests were conducted using a full-scale model of a fiber optic mortar projectile. The desired model configurations were sting-mounted using the Stability Tunnel STO-1 balance. The six-component strain gauge balance was originally constructed at the NASA Langley Research Center and has since been rebuilt by Modern Machine and Tool Company, a division of Dynamic Engineering, Inc. in Newport News, Virginia. Prior to the implementation of the FOMP test matrix, calibration checks were conducted to verify the calibration factors supplied by Dynamic Engineering.

The sting was mounted on a streamlined vertical pylon which provided remote rotation of the model in both yaw and pitch using an electrically powered gear and chain drive. During rotations the position of the balance center was maintained at the tunnel centerline.

The angle of attack output at the control center was calibrated using an electronic inclinometer mounted on the base of the sting. The yaw angle was set by visually aligning marks on the pylon turntable surface with a fixed reference location.

Data from the tests were recorded on 5.25-inch floppy diskettes by a Hewlett-Packard 9836 minicomputer interfaced with a 200-channel Hewlett-Packard 3052 voltmeter/scanner

data acquisition system. The model inputs included the six-component force and moment data (in body axes) and the data from the five pressure taps located within the model. The angle of attack and the yaw angle were input via the keyboard by the tunnel operator. The tunnel inputs were the static temperature, static pressure and dynamic pressure.

DATA REDUCTION

The tunnel inputs were used to calculate the air density, viscosity and velocity. The test Reynolds number based on the diameter of the model body was also calculated.

The pressure inputs were used to calculate a factor known as the "base drag." The base drag is a measure of the axial force that results from the gauge pressure distribution at the base of the model. Due to flow separation in the base region, the data obtained from scale tests of projectiles is not easily scaled to flight Reynolds numbers. In order to simplify the scaling procedure the base drag factor is deducted from the measured axial force in scale tests. The results are then scaled to flight Reynolds numbers and the effect of the base flow is reintroduced. Typically the scale tests must be supplemented by base pressure readings from tests at flight Reynolds numbers (Reference 1).

Four pressure taps, spaced evenly around the inner surface of the bobbin annulus, were mounted at the base of the model (Figure 11). The fifth pressure tap was located inside the nose of the model in a cavity which extended to the bobbin annulus. Each of the pressure readings was converted to a pressure coefficient by first subtracting the tunnel static pressure, then dividing the resulting quantity by the tunnel dynamic pressure. The pressure coefficients of the four annular taps were averaged to form the annular pressure coefficient (Cpa). The pressure coefficient calculated from the nose tap input was designated the cavity pressure coefficient (Cpc). In the FOMP tests the base drag coefficient (BDC) was calculated using the following formula:

$$BDC = (Cpa*Sann + Cpc*Scav) / Aref$$

The quantities Sann and Scav refer to the annular and cavity planar areas at the base of the bobbin as shown in Figure 11. The quantity Aref is the cross sectional area of the projectile body.

The force and moment data were nondimensionalized using the model body diameter (Dref) and cross sectional area (Aref) as references. Because the model was sting mounted, the force and moment data were obtained in body coordinates. As shown in Figure 12, the body X-axis was defined along the

longitudinal axis of the model. The body Y-axis was placed in the standard "right wingtip" orientation to define a longitudinal XY-plane of symmetry for the FOMP model. The body Z-axis was oriented in the proper sense for a right-hand coordinate system. The body axis data coefficients of particular interest in the zero yaw tests were the axial force coefficient (CA), the normal force coefficient (CN) and the pitching moment coefficient (Cm).

A second axis system was defined for the FOMP tests with the X'-axis directed upstream parallel to the free stream velocity vector. This stability axis system could be considered a "tunnel-fixed" system with the Y'-axis oriented perpendicular to the right wall (facing upstream) and the Z'-axis oriented perpendicular to the tunnel floor. The stability axes are shown along with the body axes in Figure 12. Note that for a zero angle of attack the stability axes coincide with the body axes in zero yaw tests. The stability axis lift coefficient (CL) and drag coefficient (CD) data were of primary interest in the zero yaw tests.

The forces and moments were received in body axis coordinates and the base drag was deducted from the axial force measurement. The force and moment data were then converted to coefficient form and transformed into stability coordinates. The tranformation procedure was simplified by

the fact that the FOMP was not tested in roll. Both the body and stability axis coefficients as well as the base drag coefficient were recorded for each of the runs.

X-CONFIGURATION

As can be seen in Figure 2, the FOMP wings and fins were not aligned with the body axes shown in Figure 12. The wing and fins were instead oriented at forty-five degree angles to the Y- and Z- body axes in what is known as an X-configuration. As can be seen in Figure 13, the convention is to actuate all four fins in order to generate a controlling moment about a single body axis in the X-configuration. The set of fin deflection equations for pitch, yaw and roll control is indeterminate until the fin bias setting is defined. The FOMP design utilized a zero fin bias which resulted in four equal fin deflections for a given elevator, rudder or aileron setting. The zero fin bias also minimized the largest individual fin deflection required for a given control setting. The equations for elevator, rudder and aileron deflections are provided in Figure 13 for a zero bias system (Reference 2). Until fin stall limits are reached it is possible to linearly combine sets of elevator, rudder and aileron deflections to generate multiple controlling moments.

FOMP TEST MATRIX

The test matrix divided the experiment into sets of four pitch/yaw runs for each model configuration. Each FOMP configuration was tested in pitch from minus four to plus sixteen degrees in two degree increments for fixed yaw angles of zero and eight degrees. Tests were also conducted in yaw from minus four to plus sixteen degrees in two degree increments for fixed angles of attack of zero and eight degrees.

Dry runs were conducted with a simple body alone configuration to certify the performance of the data acquisition hardware and software. Discrepancies noted in the normal force readings were found to be due to an oversight in the model assembly procedure. During assembly on the sting the projectile had assumed a slight "banana" shape due to a combination of fit tolerance and component weight. After realignment the FOMP model tested satisfactorily in final dry runs.

The test sequence started with body alone tests of the eight possible nose, wing slot and bobbin combinations. Subsequent test configurations utilized only the body with the 3.00" nose which was designated the "baseline body." The test sequence continued with body/fin (BF) and body/wing (BW) tests for long and short bobbin configurations. The BF

tests were conducted for both WSC and ASO configurations with zero fin deflection. The final series of runs involved elevator and aileron fin deflections for the long and short bobbin body/wing/fin (BWF) configurations.

The aerodynamic effects of the nose, the wing slot and the bobbin were obtained from the body-alone test results. Comparisons of the data for two configurations with all but one component in common yielded the incremental effect of the configuration change on the aerodynamic performance of the body. The wing and fin performances were obtained by taking the difference of the test results for two corresponding configurations, only one of which included the wings or fins in question. For example, the "baseline body alone" data could be deducted from the "body/fin" data to determine the incremental contibution of the fins to the aerodynamics of the FOMP. The wing and fin calculations yielded absolute performance contributions rather than the relative contributions between two component designs found for the nose and bobbin. There are several combinations of configurations which could be used to obtain the wing and fin performances. It is possible to estimate some component interactions by contrasting the performance results obtained from different sets of configurations.

BOUNDARY LAYER TRIP DISKS

The FOMP tests were conducted at a dynamic pressure of 11.40 inches of water or 59.3 pounds per square foot. Based on the average test atmospheric conditions the corresponding flow velocity was approximately 235 feet per second (160 MPH). The design flight dynamic pressure is 1.961 times larger than the test dynamic pressure. Under similar atmospheric conditions the flight velocity would be approximately 328 feet per second, forty percent higher than the test velocity. Using the same reasoning, the flight Reynolds number would be forty percent higher than the test Reynolds number based on diameter of 525,000. The primary focus of concern, however, was on the test chord Reynolds number of the wings and fins.

The test chord Reynolds number for the small fins was approximately 160,000 and for the large fins and wings was approximately 280,000. At flight speeds the corresponding Reynolds numbers would reach 224,000 and 392,000, respectively. The difference between the test and flight chord Reynolds numbers spans a critical region in the low Reynolds number flight regime.

Experiments at Virginia Tech have shown that the stall behavior of typical airfoils is highly dependent on Reynolds number at test Reynolds numbers below approximately 500,000.

The Reynolds number dependency is due to variations in the laminar-to-turbulent transition and flow separation characteristics of the airfoil.

For scaling reasons, roughness elements known as "trip disks" were added to model surfaces. The lines of trip disks were placed at locations representing the predicted transition regions of the projectile at flight velocities. The trip disks were added by applying punched adhesive tape to the wings, fins, forebody connector and 3.00" nose. A polyester resin was then mixed with a catalyst and smoothed over the tape to fill the holes. After curing, the excess resin was removed using sandpaper. The height of the trip disks then matched the thickness of the adhesive tape.

Trip disks were placed at one-tenth chord of the wings and fins on both the pressure and suction surfaces. On the body, trip disks were applied about the circumference of both the forebody connector and the 3.00" nose near the connector/nose joint. The height of the trip disks was chosen based on boundary layer momentum thickness calculations for each component under test conditions. The cylindrical trip disks were added to produce sharp laminar-to-turbulent transition regions on the model.

Fixing the transition regions was of particular importance for the wings and fins due to the low chord

Reynolds number flow of the FOMP tests. It was believed that the increase in boundary layer turbulence induced by the trip disks would eliminate erratic low Reynolds number airfoil behavior, thus simplifying the scaling procedure.

The method of using surface roughness to fix transition, however, has also been shown to adversely affect the lift and drag performance of airfoils. Standard surface roughness has been shown to decrease the maximum coefficient of lift of an airfoil for a given Reynolds number. For situations in which flow separation is not a predominant factor, standard surface roughness also results in an increased drag coefficient due to larger skin friction forces. The magnitude of the roughness effect increases as the transition strip is moved towards the airfoil leading edge (References 3 & 4).

DETERMINING FOMP AIRFOIL PERFORMANCE

In order to determine the performance of the FOMP wing airfoil relative to published airfoil data, several corrective steps were required.

First, it was necessary to transform the body axis data into lift and drag coefficients based on a stability axis system. The data acquisition software was modified by Subrahmanyam Kuppa to automatically calculate and store both

body and stability axis data.

Second, the coefficient data had to be converted to reflect the wing planform reference area. After the lift contribution of the wings was calculated, an area factor consisting of the ratio of body reference area to wing planform area was applied to the lift coefficient data. Note that the wing planform area did not include the fuselage area between the wings. The process of obtaining the wing CL contribution by calculating the performance differential between two configurations resulted in the the deduction of the entire body lift contribution. Including the fuselage area, therefore, would have incorrectly reduced the apparent lift coefficient produced by the wings.

Two additional corrections to the wing data involved the positioning of the body in the X-configuration. First, the overall lift contribution calculated for the wings was the sum of the lift vectors from each of the four wings. From a stability axis standpoint, therefore, the lift coefficient generated by each wing (CLw) was one-fourth of the total lift coefficient. But in order to compare the FOMP wing data to published results, the force vectors must be evaluated from a planform reference. As shown in Figure 14, each surface generated both lift and sideforce at a given angle of attack. Considering the situation from a

planform reference, the lift vector for each individual wing is the vector sum of the lift and sideforce components. The planform lift coefficient (CLi) can be calculated using the equation:

$$CLi = CLw / \cos(45^\circ) \quad (1)$$

The geometric basis for the planform calculations is shown in Figure 14.

The second effect of the X-configuration involved the effect of body pitch on the flow over the wings. As noted previously, the angle of attack for the FOMP tests was measured with respect to the longitudinal axis of the body. With the projectile in an X-configuration an effective angle of attack (αe) must be calculated for the wings as shown in Figure 15 for a zero yaw condition. In Figure 15 the wind velocity vector, V, is shown at a positive angle of attack to the XYZ body axes. For a lifting surface oriented along the Y-axis, the magnitude of the flow vector defining the planform angle of attack would be simply $/V/\sin(\alpha)$.

The X'Y'Z' axes shown in Figure 15, the X-configuration planform axes, were obtained by rotating the body axes forty-five degrees about the X-axis. For a lifting surface oriented along the Y'-axis, a positive body pitch would result in both normal and spanwise flow, each of magnitude $/V/\sin(\alpha)\cos(45^\circ)$. The effective angle of attack for a

wing in the X-configuration can thus be defined:

$$\alpha e = \arcsin [\sin(\alpha)\cos(45^\circ)]$$

For angles of attack of less than twenty degrees a close approximation to the above equation is:

$$\alpha e = \alpha \cos(45^\circ) \quad (2)$$

The spanwise components of flow induced by the X-configuration are shown in Figure 16. Note that for a positive angle of attack the direction of spanwise flow is towards the tip for the upper two wings and towards the root for the lower two wings on both the suction and pressure surfaces. The typical direction of spanwise flow on a wing at zero yaw and a positive angle of attack is towards the root on the suction surface and towards the tip on the pressure surface due to the pressure differential.

The superposition of the X-configuration and pressure induced spanwise flows is provided in Figure 17 for a positive angle of attack. Note that some flow patterns are reinforced while others are inhibited.

It has been proven that spanwise flow contributes to premature flow separation in an adverse pressure gradient by increasing the thickness of the boundary layer (Reference 5). As noted previously, the X-configuration spanwise flow component is directly dependent on the projectile angle of attack. The lift and drag performance of the FOMP wing set

can therefore be expected to diverge slightly from published airfoil data, particularly at high angles of attack when flow separation becomes a dominant factor. Furthermore, considering the flow patterns shown in Figure 17, a valid argument can be made for the likelihood of differential stall between the upper and lower wing sets in an X-configuration.

The FOMP airfoil data was converted to infinite aspect ratio using the procedure outlined in the NACA Technical Note #3911 (Reference 6). A factor consisting of the two-dimensional lift curve slope divided by the three-dimensional lift curve slope was applied to the wing lift data.

DATA AND RESULTS

Some particular areas of interest in the preliminary test program included the aerodynamic effects of variations in the nose, wing slot section and bobbin geometry. The intention was to narrow the design possibilities for the nose and bobbin components to arrive at a more efficient final design. It was also necessary to determine the body aerodynamic variations associated with the deployment of the wings during the flight sequence. The data for the nose, wing slot section and bobbin are provided for an angle of attack range of minus four to plus sixteen degrees in body axis coefficients from zero yaw, body alone tests.

The effect of the nose design on FOMP aerodynamics was determined by plotting the body-alone data for the 2.36" and 3.00" nose configurations versus angle of attack. Figures 18a and 18b are plots of the nose effect on the axial force coefficient (CA) for the WSC long and short bobbin configurations, respectively. The plots for both bobbin types show that the 3.00" nose produced substantially larger axial force coefficients than the 2.36" nose at all angles of attack. For the long bobbin configuration the CA increment between the 3.00" and 2.36" nose data ranged from a minimum of approximately 0.08 to a maximum of nearly 0.20.

Considering the same data on a percentage basis, the 3.00" nose configuration CA results were from 35% to 114% larger than the 2.36" nose results. For the short bobbin plots the CA increment ranged from approximately 0.10 to 0.20. Because of the higher overall CA magnitude due to the short bobbin, the 3.00" nose configuration CA results were only 25% to 65% larger than corresponding 2.36" nose data.

The magnitude of the nose effect on the body axial force coefficient was unexpectedly large, comparable to the effect of leading edge radius variation on airfoil performance. The nose effect on the normal force coefficient (CN) and pitching moment coefficient (Cm), however, was quite small.

In Figures 19a and 19b plots of CN versus angle of attack are provided for long and short bobbin configurations, respectively. The 3.00" and 2.36" nose CN curves are nearly identical, showing only slight differences at high angles of attack.

The long and short bobbin plots of Cm versus angle of attack are provided in Figures 20a and 20b, respectively. Again, the 3.00" and 2.36" nose plots are nearly identical for each of the bobbin configurations.

Rather than pointing to substantial variations in flow separation patterns, the data seems to indicate that the

nose effect is due simply to "form drag." The differences in the pressure distributions resulting from a variation in the nose radius of curvature have a strong effect on the generation of axial force. The CN and Cm data similarity for the two noses appears to rule out any signifigant flow separation effects, however.

The effect of the wing slot section variation on body aerodynamics was determined by contrasting the baseline body-alone data obtained from WSC and ASO tests. Figures 21a and 21b show the plots of the wing slot effect on CA versus angle of attack for long and short bobbin configurations, respectively. For both bobbins the ASO wing slot configuration produced a larger axial force coefficient at all angles of attack. The magnitude of the wing slot CA increment was greater for the long bobbin configuration than for the short bobbin configuration at angles of attack below six degrees. This disparity can be explained by considering the turbulence shed by the complex ASO geometry. An increase in the boundary layer turbulence would have a greater cumulative effect on the long bobbin axial force coefficient than the short bobbin axial force coefficient due to the correspondingly larger skin friction contribution.

At angles of attack of six degrees or higher the wing slot CA effect is nearly identical for the two bobbin configurations. It is believed that the predominant factor in the wing slot CA increment at higher angles of attack was the difference in flow separation between the square ASO and circular WSC cross sections. The larger zone of flow separation for the ASO configuration resulted in a larger axial force coefficient at any given angle of attack.

The plots of the wing slot effect on CN for long and short bobbin configurations are provided in Figures 22a and 22b, respectively. At low angles of attack there is little difference in the normal force coefficient generated by the ASO and WSC configurations. At angles of attack of six degrees or higher the magnitude of the wing slot CN increment increased in direct proportion to the angle of attack for both the long and short bobbin configurations.

The wing slot data was rearranged to reveal the effect of bobbin variation on FOMP body performance. The bobbin effect on CA is plotted in Figures 23a and 23b for the WSC and ASO configurations, respectively. Surprisingly, the short bobbin configurations developed substantially larger axial force coefficients than the long bobbin configurations at all angles of attack. The CA increment for the WSC configurations ranged from a maximum of approximately 0.19

at minus four degrees to about 0.08 at plus sixteen degrees. The CA increment for the WSC configurations translates to a relative percentage difference ranging from approximately 13% to 70% between the long and short bobbin data. For the ASO configurations, the CA increment at minus four degrees was reduced from the WSC value of 0.19 to approximately 0.11. It is believed that the narrowing of the long and short bobbin CA performance differential can be attributed primarily to the effect of the increase in boundary layer turbulence on the skin friction that was generated by the two bobbin configurations. But, despite the effects of skin friction on the two ASO configurations, the short bobbin configuration still developed larger axial force coefficients than the long bobbin configuration.

It is believed that the bobbin CA performance differential was caused by differences in the aft turbulent separation zones for the two bobbin configurations. According to the pressure data obtained during the tests, the long bobbin produced a fuller pressure recovery in the base region than did the short bobbin.

The annular and cavity pressure coefficients for the long and short bobbin WSC baseline body alone tests are provided in Figure 24. The cavity pressure coefficients were roughly equal for the two bobbin configurations and

remained constant with angle of attack. The annular pressure coefficient plots, however, show that the short bobbin generated lower base pressures than the long bobbin. The combination of larger axial force coefficients and more negative base pressure coefficients is believed to result from larger base flow separation regions for the short bobbin body configurations.

Figures 25a and 25b are plots of the bobbin effect on CN versus angle of attack for WSC and ASO baseline body configurations, respectively. As expected, the long bobbin configurations produced larger normal force coefficients than the short bobbin configurations at high angles of attack. The CN increment was quite small, however, and is attributed entirely to the additional five inches of total body length present in the long bobbin configurations.

Reviewing the body-alone data presented in Figures 18a through 25b, two basic conclusions can be drawn. First, it is clear that the body axial force coefficient is highly dependent on the design of the nose and bobbin components employed in the configurations. Second, it is apparent that the change from a WSC to ASO configuration during flight will have a significant effect on both the axial and normal force coefficients generated by the FOMP body.

Considering WSC configurations at a zero angle of attack, for example, the combination of the long bobbin and 2.36" nose produced a CA of 0.176 while the combination of the short bobbin and 3.00" nose produced a CA of 0.511, over 2.9 times as large. The corresponding CA measurements at an angle of attack of six degrees were 0.246 and 0.512, the short bobbin and 3.00" nose combination again producing more than twice the axial force of the long bobbin and 2.36" nose pairing.

The WSC body alone data was converted to stability coordinates and plotted in a lift versus drag format. Provided in Figure 26, the CL versus CD curves reveal virtually the same performance information as the previous body axis plots, but in a more compact form. The most efficient body configuration was the long bobbin and 2.36" nose combination. It generated the largest lift-to-drag ratios and the smallest zero-lift drag coefficient. Replacing either the long bobbin or the 2.36" nose with their counterparts had an equally detrimental effect on the lift-to-drag ratio and zero-lift drag coefficient of the projectile body. The least efficient body configuration was the short bobbin and 3.00" nose combination.

The second major area of interest in the FOMP test program involved the performance of the wings and fins.

Tests were conducted on body/wing/fin (BWF) configurations to determine the control capability of the small and large fins in pitch and roll. All of the data presented in subsequent elevator deflection, fin effectiveness and wing effectiveness plots are from tests made with a yaw angle, beta, of zero degrees (designated Be0).

The four BWF configurations tested were the long bobbin and small fin (B1F1Be0), the short bobbin and small fin (B2F1Be0), the long bobbin and large fin (B1F2Be0), and the short bobbin and large fin (B2F2Be0).

The Cm versus alpha plots for the B1F1Be0 and B2F1Be0 BWF configurations are provided in Figures 27a and 27b, respectively. The generally positive slope of the Cm curves indicates that the small fin configurations are statically unstable in pitch at most angles of attack. In order to determine the actual contribution of the fins, the Cm fin effectiveness was calculated for the B1F1Be0 and B2F1Be0 configurations by subtracting the corresponding BW data from the BWF data plotted in Figures 27a and 27b.

The Cm fin effectiveness results are plotted in Figures 28a and 28b, respectively. The average Cm increment per degree of angle of attack for the small fins was calculated to be in the range of -0.10 to -0.11 at moderate angles of attack for elevator deflections of plus four through minus

sixteen degrees. The results for the elevator deflection calculations indicated a similar range of Cm increment per degree of elevator deflection for conditions in which the sum of the magnitudes of the elevator deflection and angle of attack did not exceed approximately sixteen degrees.

It appears that for the X-configuration design with fully actuated fins, the fin Cm increment per degree of elevator deflection is, in most cases, equivalent to the fin Cm increment per degree angle of attack. The exceptions occur when a change in the model angle of attack significantly alters the fin/body or fin/wing interference effects. An example, which will be discussed subsequently, is the effect of wing downwash on the fins. It will be shown that the magnitude of the downwash effect on the fins increases rapidly with angle of attack. For a given angle of attack, however, the downwash effect would remain constant with respect to elevator deflection. Under such conditions, the fin Cm increment per degree of elevator deflection would differ from the fin Cm increment per degree of angle of attack.

The inability of the small fins to overcome the destabilizing influence of the FOMP body in pitch is directly related to the magnitude of the normal force coefficients generated by the fins. The CN versus angle of

attack plots for the B1F1Be0 and B2F1Be0 BWF configurations are provided in Figures 29a and 29b, respectively. Corresponding CN fin effectiveness results are plotted in Figures 30a and 30b. Calculations indicate that the small fins generated an average CN increment per degree of elevator deflection of about 0.03.

To determine the accuracy of the fin effectiveness data, the CN elevator deflection increment was multiplied by the distance from the small fin hinge to the center of gravity, 17.14 inches, and then divided by the length Dref. The result was a Cm increment of -0.109 per degree of elevator deflection which is within the approximate range described previously.

In order to determine the trim conditions for the B1F1Be0 and B2F1Be0 BWF configurations, plots of CN versus Cm were constructed. Trim conditions were defined as points of zero pitching moment. The possible effects of the optic fiber on the pitch behavior of the projectile were neglected. Two points of zero pitching moment occur on the plots provided in Figures 31a and 31b. The trivial trim condition occurred for an angle of attack and elevator deflection of zero degrees. The second trim location occurred at an angle of attack of approximately 9.5 degrees for a plus four degree elevator deflection. As noted

previously, neither trim location defines a statically stable flight attitude.

Similar plots and calculations were made for the large fin configurations. The Cm versus angle of attack plots are provided in Figures 32a and 32b for the B1F2Be0 and B2F2Be0 BWF configurations, respectively. The Cm curves exhibit a negative slope at most combinations of angle of attack and fin deflection which indicates that the large fin configurations are statically stable in pitch. Corresponding Cm fin effectiveness plots for the B1F2Be0 and B2F2Be0 configurations are provided in Figures 33a and 33b, respectively. For the range of elevator deflections and angles of attack shown in Figures 33a and 33b, the average Cm increment per degree of elevator deflection varied from -0.31 to -0.38. The large fins, therefore, produced several times the controlling moment of the small fins per degree of elevator deflection.

Figures 34a and 34b show plots of CN versus angle of attack for the B1F2Be0 and B2F2Be0 BWF configurations, respectively. The corresponding CN fin effectiveness plots are provided in Figures 35a and 35b. The CN plots for the B1F2Be0 configuration in Figures 34a and 35a exhibit unevenly spaced CN increments with respect to elevator deflection and are highly inconsistent with the uniformly

distributed curves for the B2F2Be0 configuration. The Cm fin effectiveness data for the two configurations match quite well, however, with uniform Cm increments for the elevator deflections that were tested. It is therefore extremely doubtful that the CN discrepancy was caused by an error in the fin deflection setting. Due to the presence of the inconsistency, however, only the B2F2Be0 configuration test results were used for large fin trim calculations. The CN fin effectiveness plots in Figure 35b show that an elevator deflection of minus sixteen degrees for the large fins produced a normal force coefficient of -1.57 at a zero angle of attack, a CN increment of approximately 0.10 per degree of elevator deflection. The CN reading of -1.57 is comparable to the CN developed by the WSC baseline body configurations at an angle of attack of plus sixteen degrees.

In order to determine the trim conditions for the B1F2Be0 and B2F2Be0 BWF configurations in pitch, the elevator deflection results were plotted in a CN versus Cm format. The plots are provided in Figures 36a and 36b, respectively. Trim conditions were calculated by using the technique of linear interpolation to arrive at a zero pitching moment solution. For the angle of attack range of minus four to plus sixteen degrees, the B2F2Be0

configuration produced only one trim location in pitch other than the trivial solution. The trim condition occurred for an angle of attack of 8.50 degrees and an elevator deflection of minus four degrees. The corresponding normal force coefficient at trim was 4.796.

The wings were designed to produce the majority of the normal force required for high-acceleration maneuvering. The location of the wing quarter-chord coincided with the designated center of gravity of the FOMP. Since the location of the wing center of pressure can be reasonably estimated to be at the quarter-chord for small angles of attack, it would safe to conclude that the wings would have little influence on the FOMP pitching moment coefficient.

The wing performance was calculated by deducting ASO baseline body alone data from corresponding BW data. The plots of the Cm wing effectiveness computed from both long and short bobbin configurations are provided in Figure 37a. As expected, the wings are shown to have practically no effect on the pitching moment coefficient of the FOMP for angles of attack of six degrees or less. At higher angles of attack the wings produced a rapidly increasing Cm contribution. Such an increase in the pitching moment coefficient is generally the product of a forward shift in the center of pressure location resulting from trailing edge

flow separation. It is believed, however, that the positioning of the wings in the X-configuration might also have contributed to the increase in pitching moment coefficient.

Plots of CN wing effectiveness versus angle of attack are provided in Figure 37b. The plots for both the long and short bobbin configurations show nearly perfect agreement, indicating that the test procedure produced reliable and repeatable results. The CN contribution of the wings reached a maximum of 5.015 at an angle of attack of fourteen degrees, approximately two-thirds of the total normal force coefficient generated by the B2F2Be0 configuration at the same angle of attack for a zero fin deflection condition.

The body coefficient wing effectiveness data was also plotted in the more familiar lift and drag coefficient format in Figures 38a through 38c. Note that the coefficients are based on the body area reference, not planform reference, and are provided without the application of any "correction factors." The CD wing effectiveness plots given in Figure 38a show that large increases in the drag coefficient, an indicator of stall, occurred for a body angle of attack of between ten and twelve degrees. The CL wing effectiveness plots, provided in Figure 38b, show that the wing lift curve became nonlinear for angles of attack

above ten degrees. The maximum coefficient of lift for the wings was reached at an angle of attack of approximately fourteen degrees.

The lift-to-drag ratio of the wings, calculated from both long and short bobbin configuration test data, is plotted in Figure 38c. The largest lift-to-drag ratio for the wings was approximately 11.7 at an angle of attack of eight degrees. Calculations for the B1F2Be0 BWF configuration with zero fin deflection indicate that the overall lift-to-drag ratio for the projectile reached a maximum of approximately 5.10 at the same angle of attack.

As stated previously, research has shown that the addition of surface roughness, particularly leading edge roughness, can substantially affect the lift and drag performance of an airfoil. The NACA 0012 airfoil data provided in Figure 39 shows the effect of standard surface roughness at a chord Reynolds number of 6,000,000. The airfoil with the roughened surface stalls at a much lower angle of attack and exhibits a reduced maximum coefficient of lift as compared to the smooth airfoil. The lift curve slope, however, is virtually unaffected by the addition of surface roughness.

In order to determine the performance of the wing airfoil relative to published airfoil data, the CL wing

effectiveness data shown in Figure 38b was corrected as discussed in the experimental procedure to reflect the effects of the X-configuration [Equations (1) and (2)] and the effects of finite aspect ratio. The FOMP airfoil lift data for a test Reynolds number of 278,000 was then plotted versus angle of attack in Figure 40 along with selected NACA 0012 data from Reference 7 for test Reynolds numbers ranging from 170,000 to 3,180,000.

As previously described, the FOMP wing employed a NACA 0012 airfoil with a line of trip disks placed at one-tenth chord to fix the wing transition region. In Figure 40 it may be noted that the lift curve slopes for the FOMP wing data and the published NACA data are approximately equal. Furthermore, the FOMP wing lift curve exhibits the premature stall characteristics and reduced maximum coefficient of lift that is expected from a roughened airfoil surface. Clearly the FOMP wing results, after making the appropriate X-configuration and aspect ratio corrections, are consistent with published results for similar surface roughness and Reynolds number conditions. It remains unclear what effect, if any, the spanwise flow induced by the X-configuration had on the performance of the FOMP wings and fins.

Calculations were made from B1F2Be0 BWF and BF configurations to determine the wing downwash effect on the

lift performance of the large fin in pitch. The two sets of fin effectiveness results corrected for the X-configuration and finite aspect ratio are provided in Figure 41. The effect of the wing downwash was to reduce the effective angle of attack of the fins. The magnitude of the downwash effect was directly dependent on the FOMP angle of attack. At low angles of attack the wing/fin interference was quite small. At the maximum FOMP angle of attack of plus sixteen degrees, the effective large fin angle of attack was reduced by approximately 39.2%, from 11.31 degrees to 6.88 degrees.

CONCLUSIONS

Of particular interest in the preliminary test program were the effects of variations in the geometry of the nose, the fiber optic bobbin and the wing slot section on the aerodynamics of the FOMP body.

During the body alone runs two types of noses, one with a 3.00" radius of curvature and one with a 2.36" radius of curvature, were tested. The variation in the nose radius of curvature was shown to have little effect on the normal force coefficient and pitching moment coefficient generated by the projectile body for angles of attack ranging from minus four to plus sixteen degrees. The magnitude of the body axial force coefficient, however, was found to be highly dependent on the radius of curvature of the nose. Configurations utilizing the 3.00" nose produced substantially larger axial force coefficients than corresponding 2.36" nose configurations in pitch. The design considerations for improving the aerodynamic efficiency of the FOMP, therefore, are in direct opposition to the design considerations for reducing the distortion of targeting signals received by optical receptors housed in the nose.

Two bobbin designs were tested in order to determine the effects of bobbin length on the aerodynamics of the

FOMP. The long bobbin employed a tapered spool design which resulted in a total body length of 55.0 inches. The short bobbin employed a more compact, flat spool design which resulted in a total body length of 50.0 inches. Judging from the viewpoint of skin friction, it was expected that the short bobbin configurations would produce less axial force than the long bobbin configurations. But tests showed that both the WSC and ASO long bobbin configurations produced smaller axial force coefficients than corresponding short bobbin configurations at all angles of attack. It is believed that the differences in the axial force performance of the two bobbin designs were caused by variations in the aft turbulent separation zones. According to the annular pressure data collected during the tests, the long bobbin design developed a fuller pressure recovery in the base region. The normal force coefficient data for the two bobbin configurations showed only the small differences that would normally be associated with a variation in the length of a projectile.

The stability axis data for the WSC body alone runs showed that the most efficient body configuration was the 2.36" nose in combination with the long bobbin. The lift-to-drag ratio and zero-lift drag coefficient produced by the projectile body were adversely affected by similar margins

with the substitution of either the short bobbin or the 3.00" nose. The combination of the 3.00" nose and the short bobbin was the least efficient body configuration, producing a zero-lift drag coefficient approximately 2.9 times larger and a lift-to-drag ratio 1.5 to 2.5 times smaller than the most efficient WSC configuration.

The effect of the wing slot section variation on body aerodynamics was determined by contrasting the baseline body alone data obtained from WSC and ASO tests. The ASO configurations produced larger axial force coefficients than corresponding WSC configurations at all angles of attack. In addition, the ASO configurations produced larger normal force coefficients at angles of attack of six degrees or higher. The test results show that replacing the WSC section with the ASO section had a greater effect on the axial force coefficients produced by the long bobbin configurations than by the short bobbin configurations at low angles of attack. It is believed that the exposure of the wing slots to the free stream significantly increased the boundary layer turbulence and thus the production of skin friction aft of the wing slot region at low angles of attack. The predominant factor in the wing slot effect at angles of attack above six degrees is believed to have been differences in the flow separation characteristics of the

WSC and ASO sections. The larger zone of flow separation produced by the ASO section resulted in larger axial and normal force coefficients for the ASO configurations.

Another major area of interest concerned the performance of the FOMP in pitch for the two types of fins employed in the elevator deflection tests. Plots of the pitching moment coefficient versus angle of attack showed that the small fin configurations were generally statically unstable in pitch. The large fin configurations, however, were shown to be statically stable in pitch for most combinations of angle of attack and elevator deflection.

The wings were designed to produce the majority of the normal force required for maneuvering. Wing effectiveness calculations for the B2F2Be0 configuration showed that the wings generated approximately two-thirds of the total BWF normal force at an angle of attack of fourteen degrees for a zero fin deflection condition. In the FOMP design, the wing quarter-chord was located at the center of gravity of the projectile to minimize the pitching moment influence of the wings. But the Cm wing effectiveness plots showed that the wings produced a significant destabilizing pitching moment at high angles of attack. The increase in Cm at high angles of attack was presumably the result of a forward shift in the center of pressure location due to trailing edge flow

separation. But it is believed that the positioning of the wings in the X-configuration might have contributed to the rapid increase in Cm at high angles of attack.

In order to determine the lift performance of the wing airfoil relative to published airfoil data, the CL wing effectiveness was calculated by subtracting ASO baseline body alone data from corresponding body/wing data. An area factor was applied to the results to compensate for the disparity between the wing planform reference area and the body reference area. Since each wing produced side force as well as lift at a given angle of attack, it was also necessary to make geometric corrections to the stability lift data to reflect the "lift" produced from a planform reference. In addition, the effective angle of attack was calculated for the wing planform based on the angle of attack of the projectile body and the geometry of the X-configuration. The data was then corrected to infinite aspect ratio using the procedure given in NACA TN #3911.

The wing lift curve was expected to exhibit premature stall and a reduced maximum lift coefficient due to the presence of the trip disks used to fix the flow transition region. It was also expected that the spanwise flow induced by the X-configuration would contribute to premature stall by increasing the thickness of the boundary layer on the

wings. As noted previously, the upper and lower wing sets encountered contrasting spanwise flow situations for a given angle of attack and could reasonably be expected to exhibit some variation in lift performance. But because the lift coefficients could be obtained only for the entire set of four wings, it was not possible to determine if any individual variations in wing lift performance were present. The lift curve slope obtained for the wing NACA 0012 airfoil matched well with published results. The FOMP wing lift curve exhibited premature stall with a maximum lift coefficient approximately 0.12 lower than the maximum lift coefficient obtained for a smooth NACA 0012 airfoil at similar Reynolds numbers.

Large fin performance calculations were made from both body/wing/fin and body/fin B1F2Be0 configurations to determine the wing downwash effect on the fins. The magnitude of the downwash effect was found to be directly dependent on the angle of attack of the FOMP, greatly reducing the lift performance of the large fins at high angles of attack. Because the wings generated a large destabilizing pitching moment at high angles of attack, the wing downwash greatly reduced the margin of stability of the large fin configurations at high angles of attack.

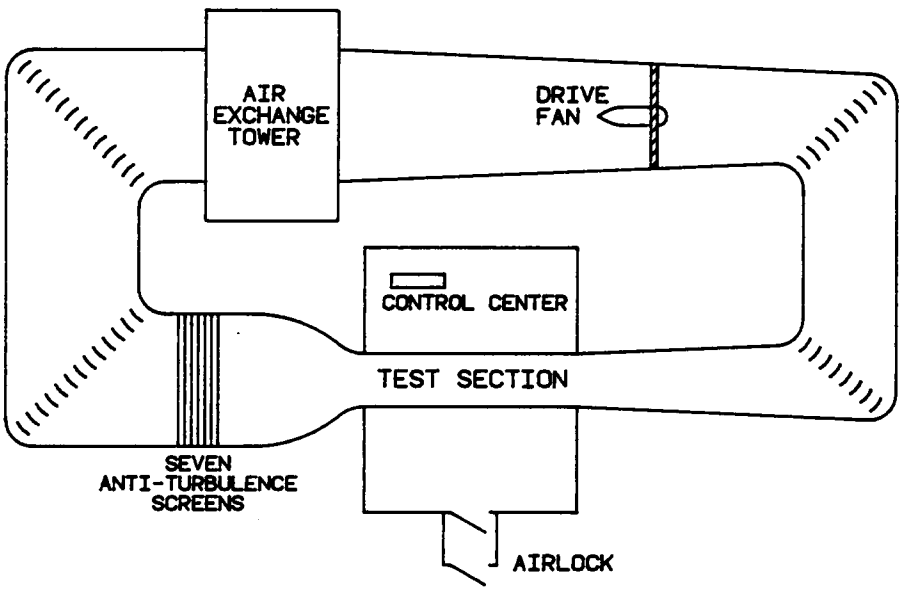

FIGURE 1: VA TECH STABILITY WIND TUNNEL

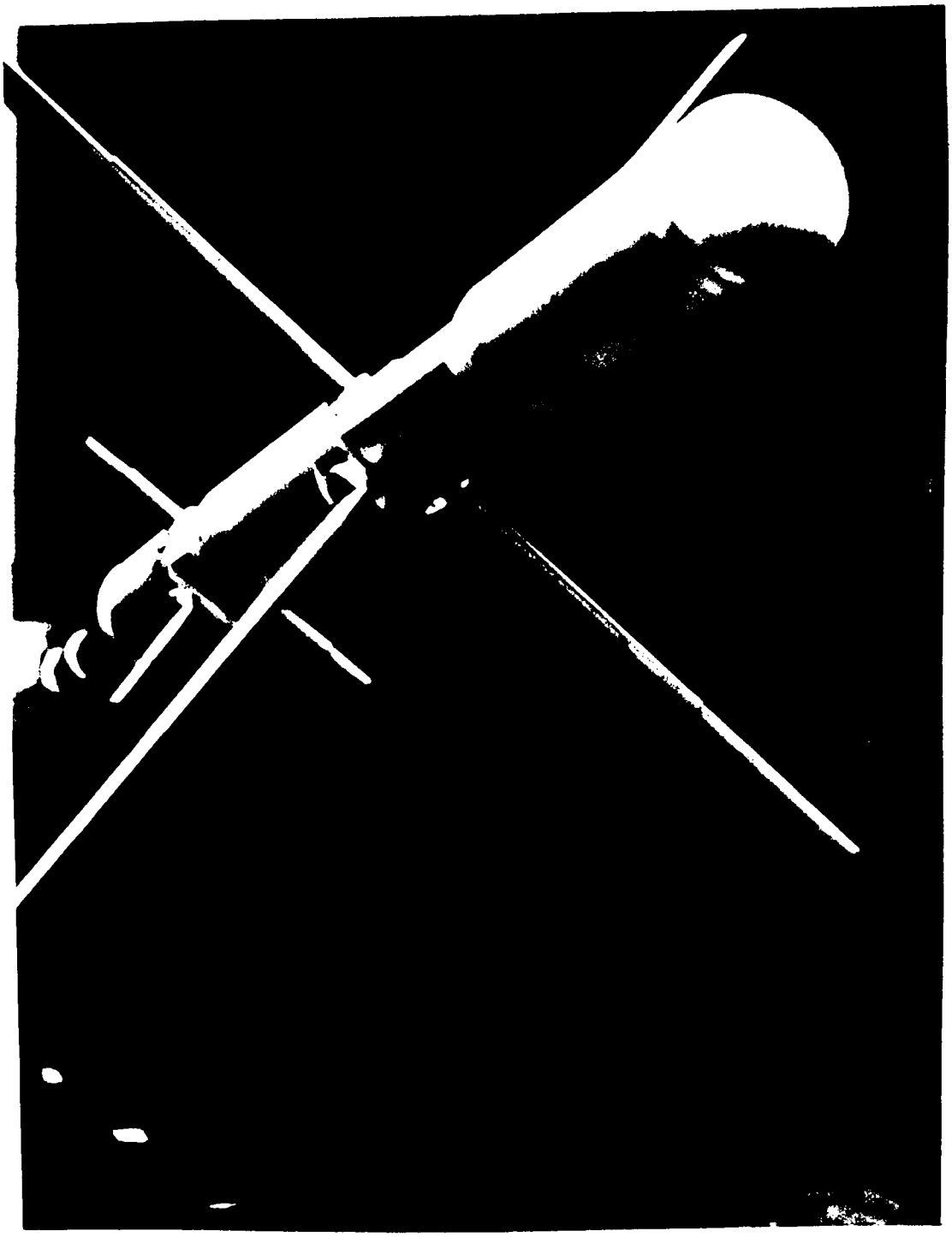

FIGURE 2: PHOTOGRAPH OF FOMP MODEL

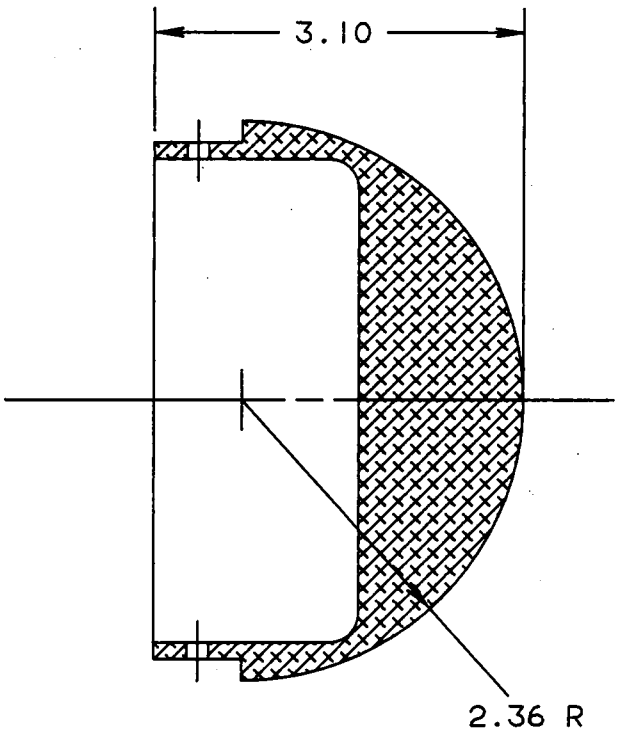

FIGURE 3A: 2.36" NOSE

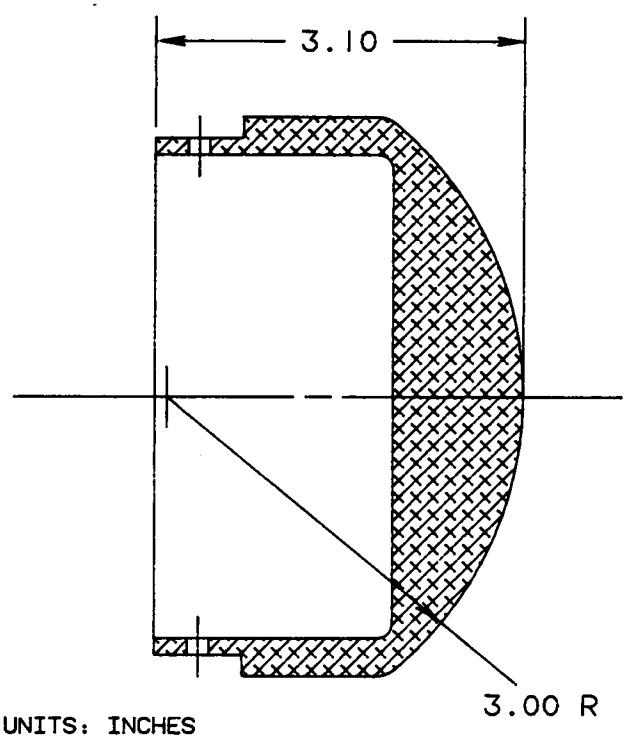

FIGURE 3B: 3.00" NOSE

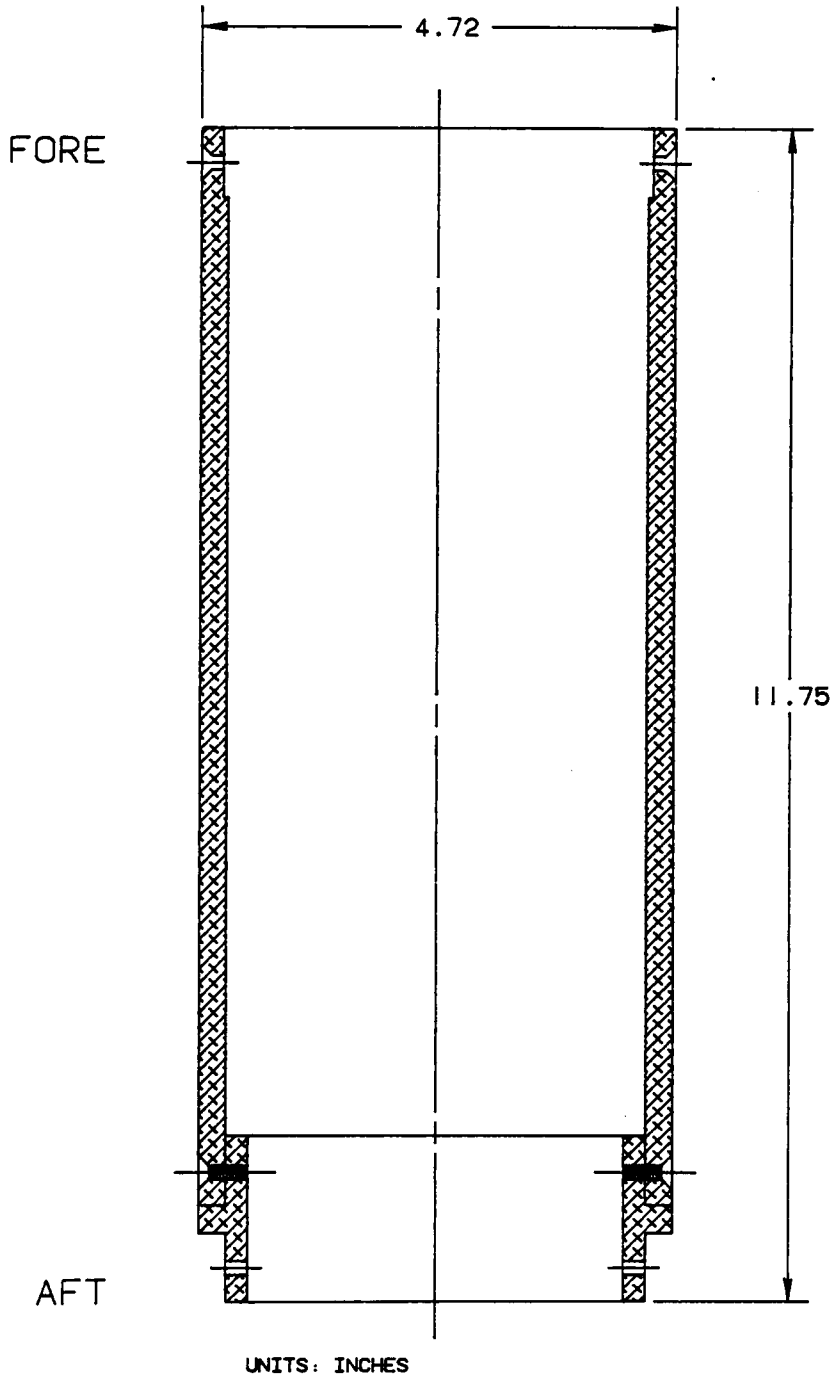

FIGURE 4: FOREBODY CONNECTOR

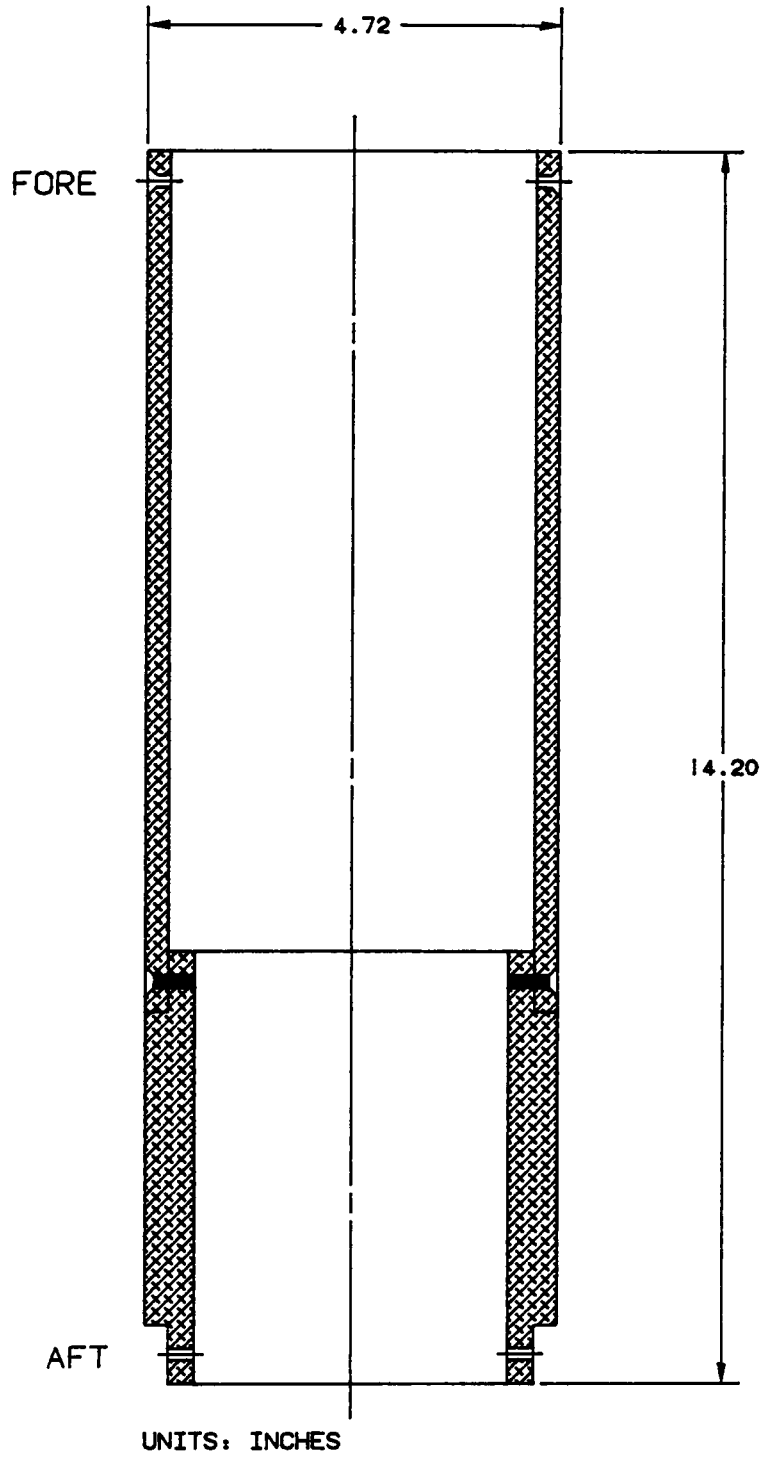

FIGURE 5A: WING SLOT SECTION (WSC)

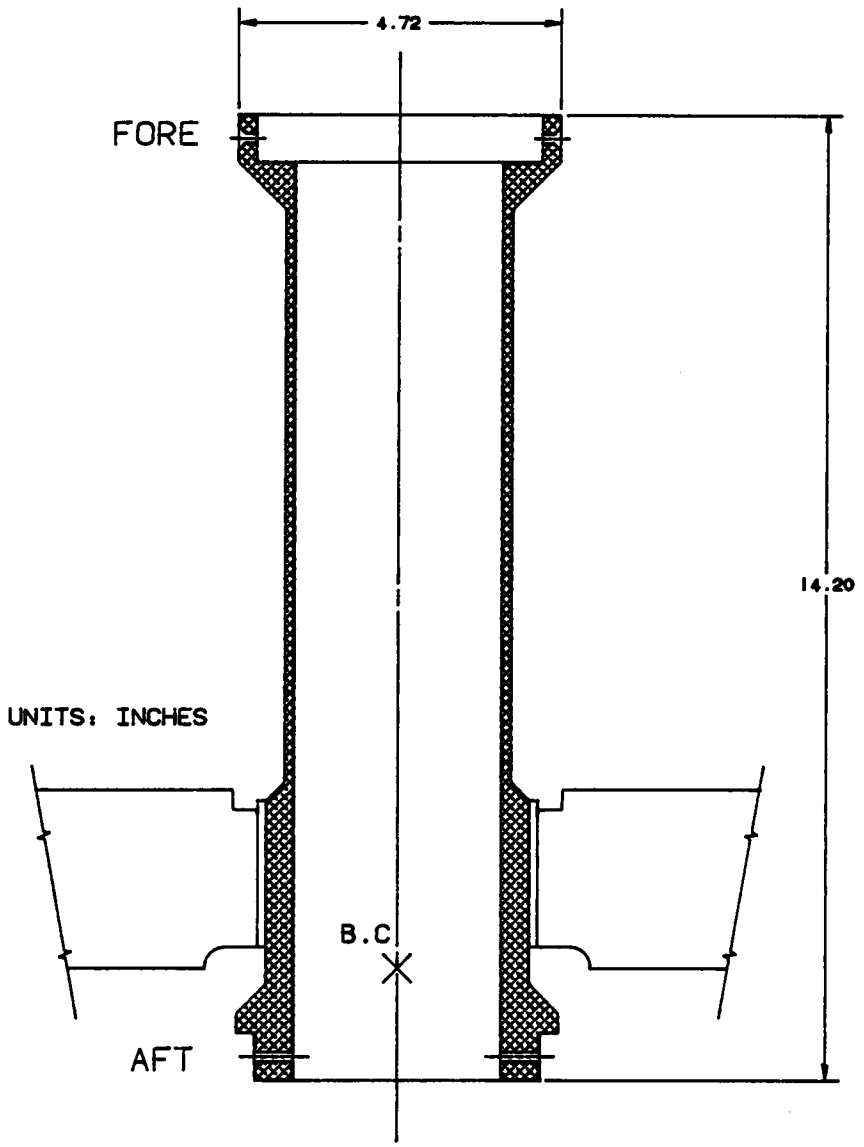

FIGURE 5B: WING SLOT SECTION (ASO)

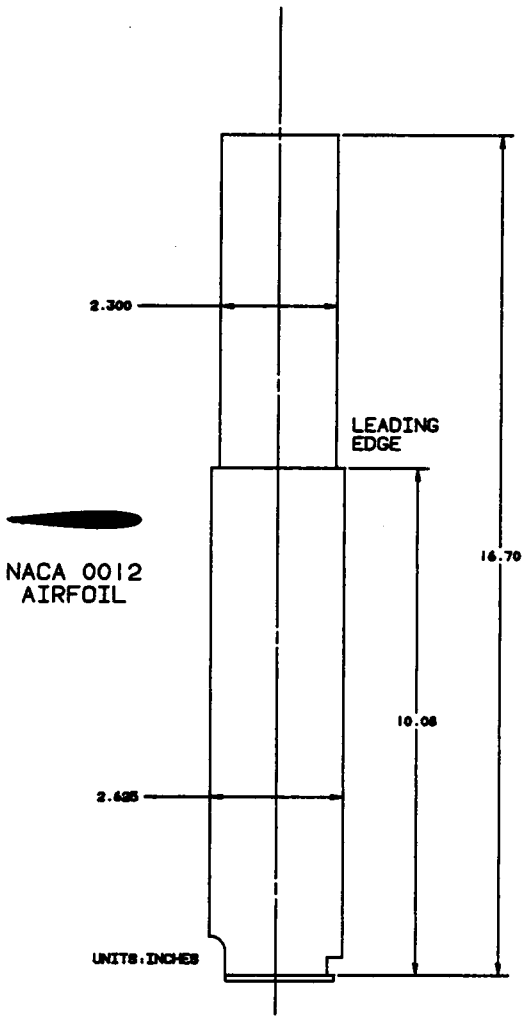

FIGURE 6: WING PLANFORM

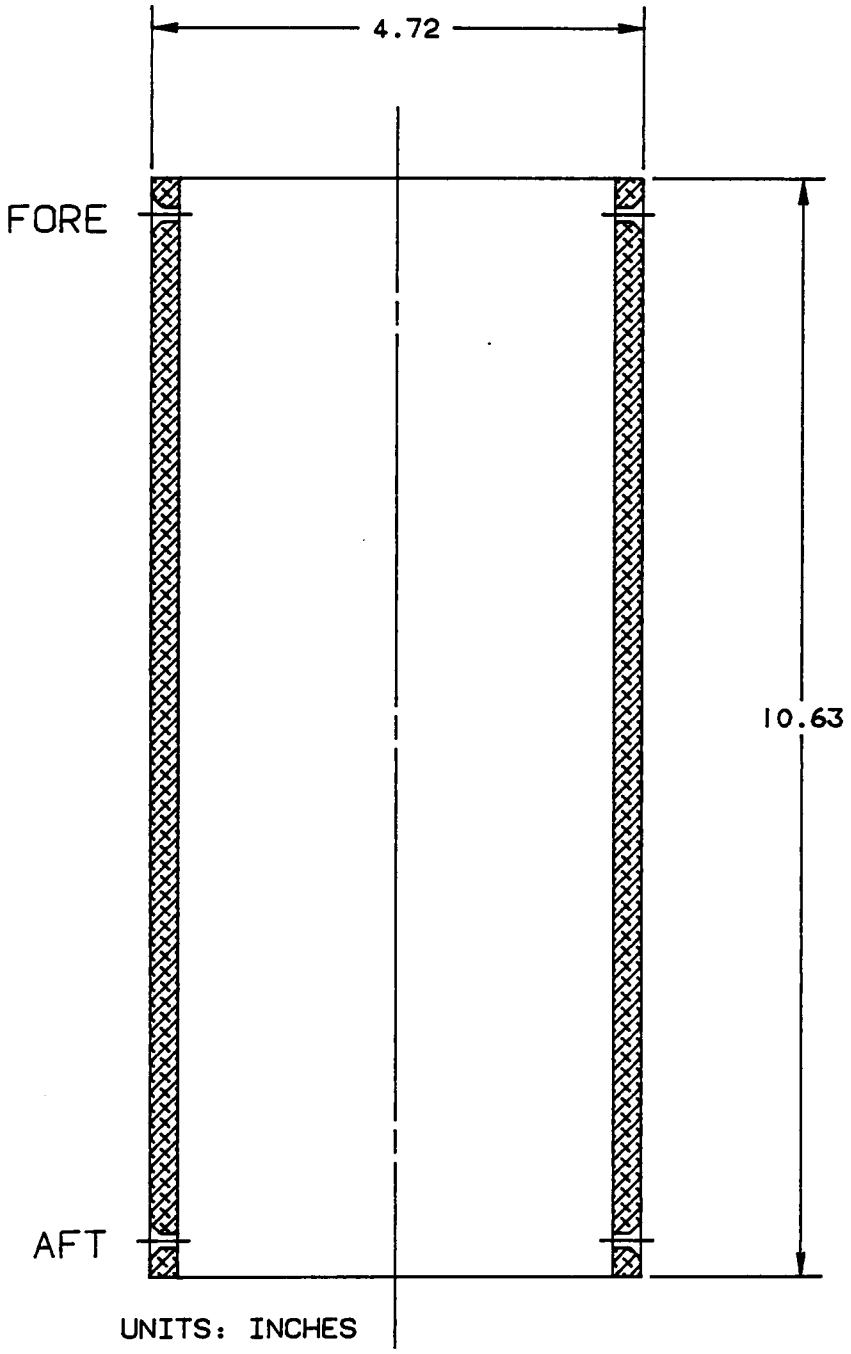

FIGURE 7: AFTBODY CONNECTOR

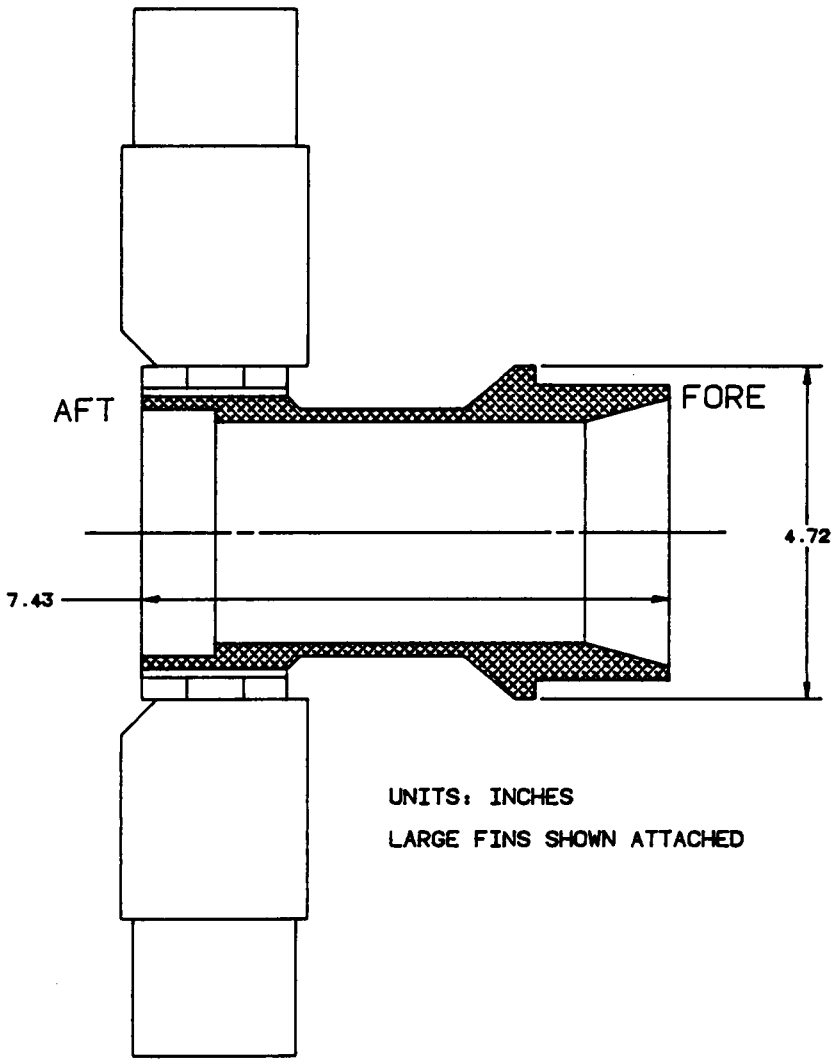

FIGURE 8: FIN SLOT SECTION

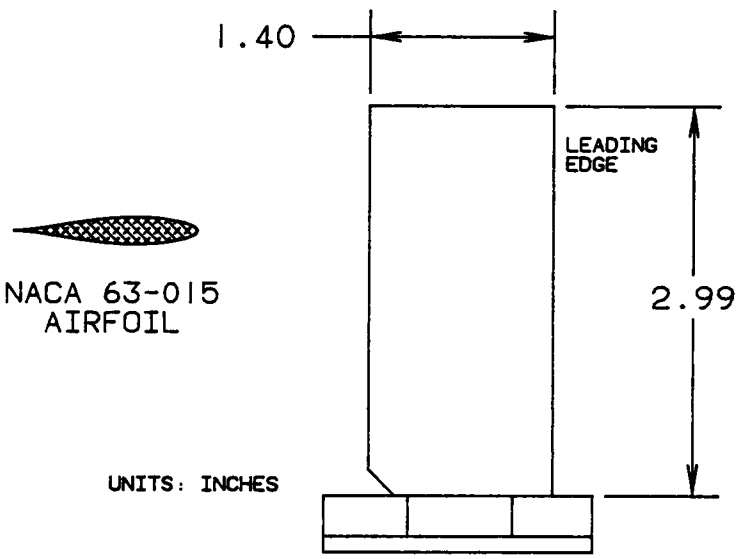

FIGURE 9A: SMALL FIN PLANFORM

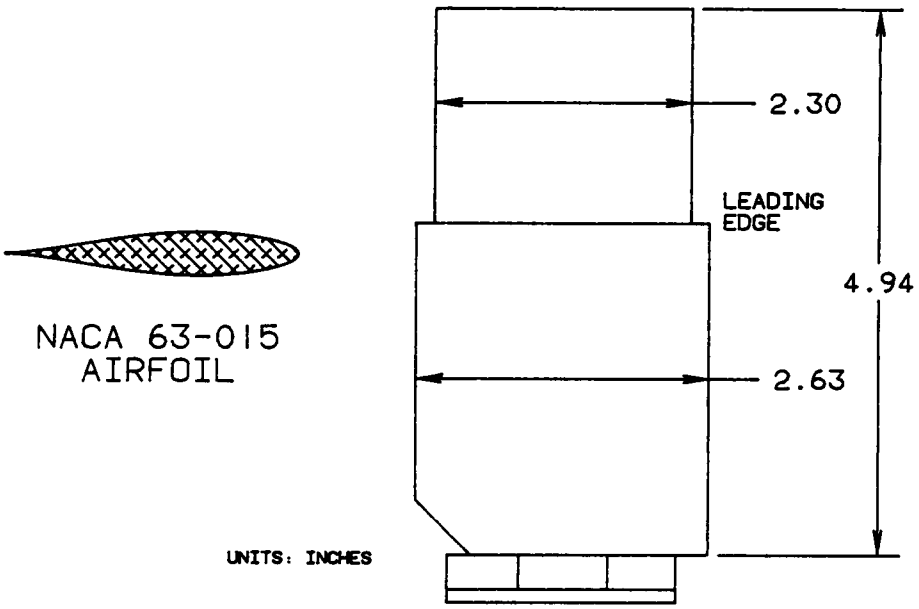

FIGURE 9B: LARGE FIN PLANFORM

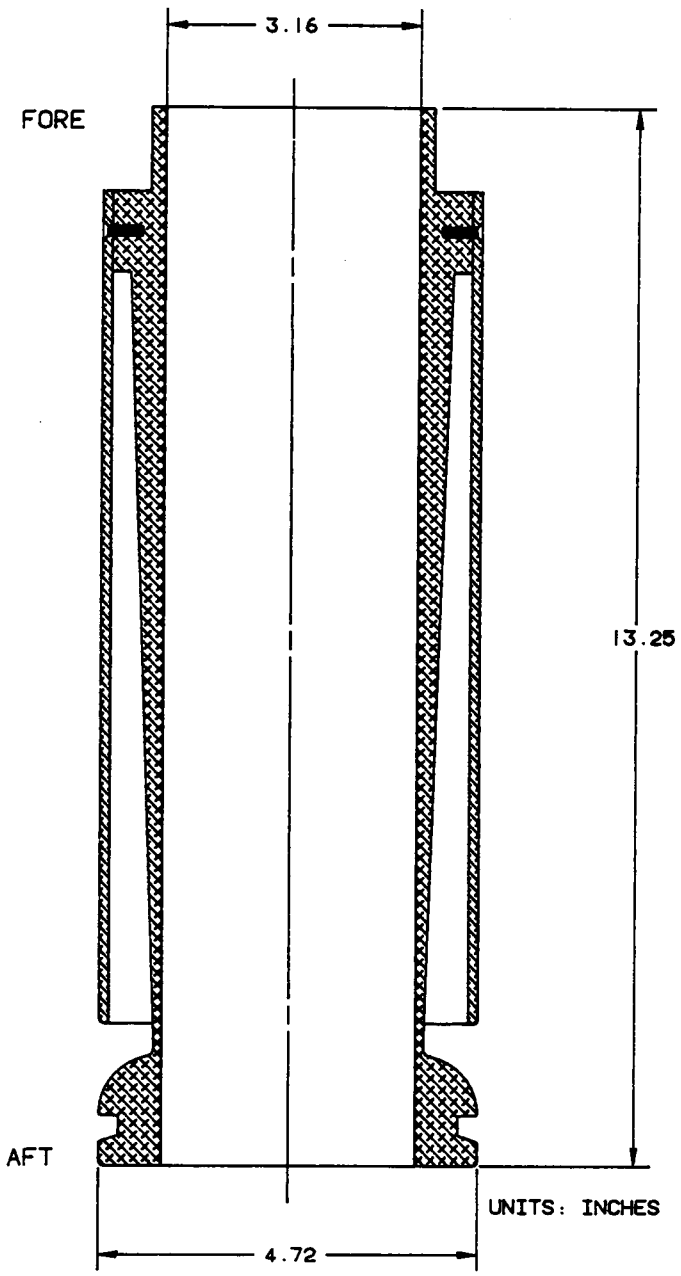

FIGURE 10A: LONG BOBBIN

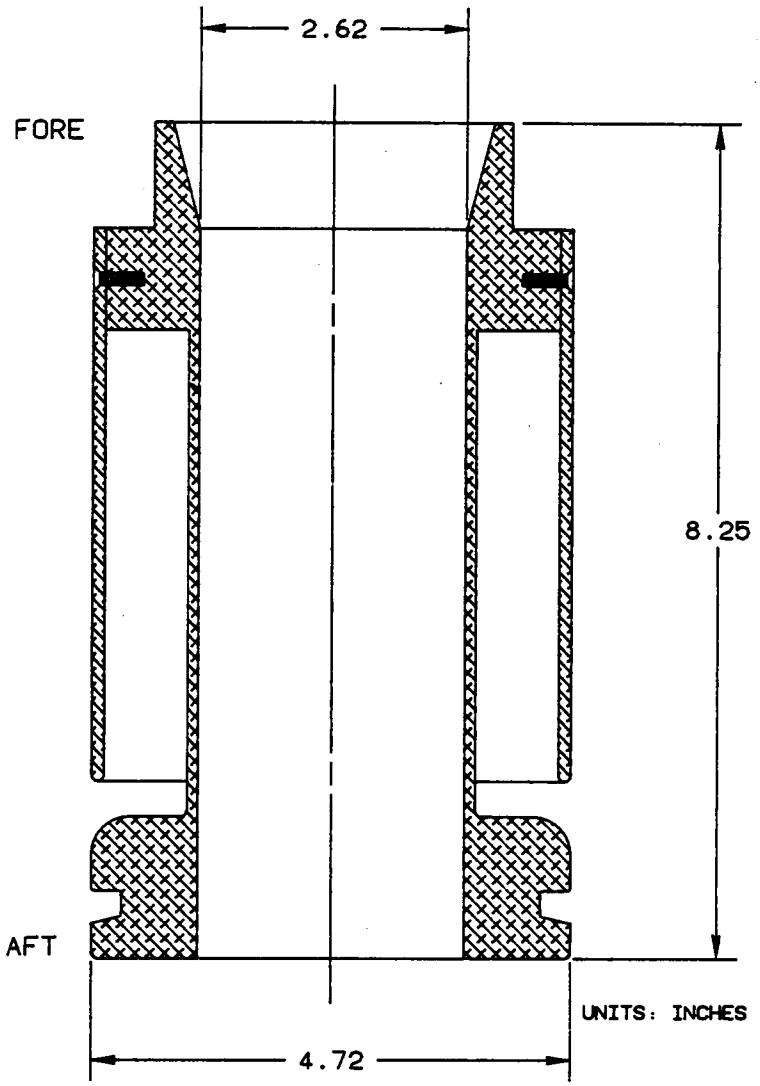

FIGURE 10B: SHORT BOBBIN

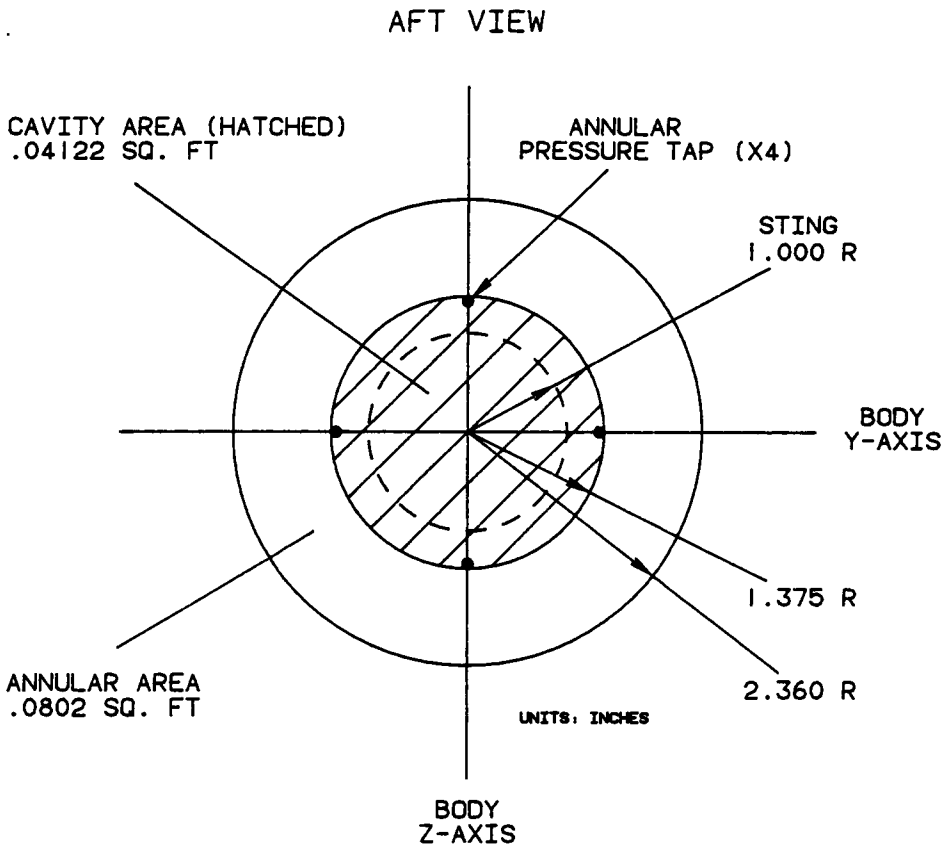

FIGURE 11: GEOMETRY OF THE BASE REGION

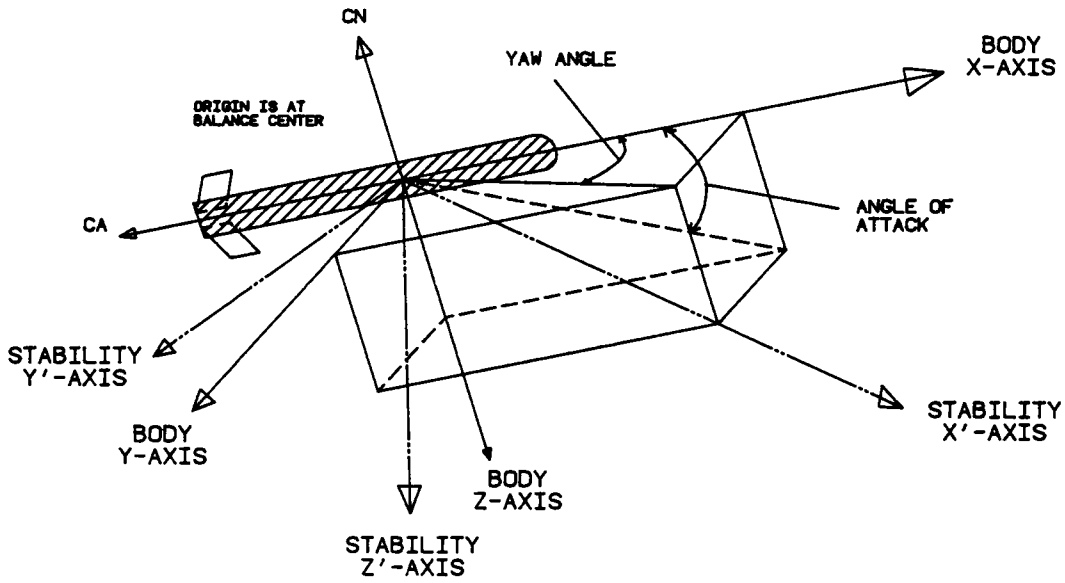

FIGURE 12: BODY AND STABILITY AXIS SYSTEMS

AFT VIEWS OF FOMP

ARROWS INDICATE MOVEMENT DIRECTION OF FIN LEADING EDGE AND DIRECTION OF FORCE VECTOR

THE FIN NUMBERING CONVENTION IS AS SHOWN ON THE PITCH DIAGRAM

A POSITIVE FIN DEFLECTION IS DEFINED AS CLOCKWISE AS VIEWED FROM THE TIP

FOR COMBINATIONS OF PITCH, YAW AND ROLL THE FIN DEFLECTIONS ARE:

$$\Delta 1 = -\Delta e + \Delta r + \Delta a$$
$$\Delta 2 = \Delta e + \Delta r + \Delta a$$
$$\Delta 3 = \Delta e - \Delta r + \Delta a$$
$$\Delta 4 = -\Delta e - \Delta r + \Delta a$$

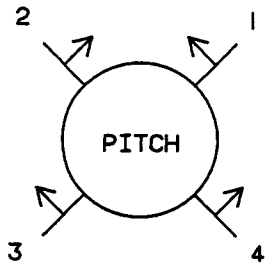

ELEVATOR DEFLECTION

$$\Delta e = \frac{-\Delta 1 + \Delta 2 + \Delta 3 - \Delta 4}{4}$$

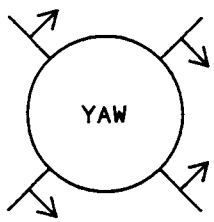

RUDDER DEFLECTION

$$\Delta r = \frac{\Delta 1 + \Delta 2 - \Delta 3 - \Delta 4}{4}$$

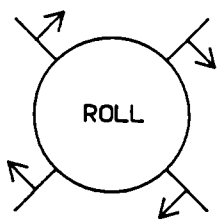

AILERON DEFLECTION

$$\Delta a = \frac{\Delta 1 + \Delta 2 + \Delta 3 + \Delta 4}{4}$$

FIGURE 13: PITCH, YAW AND ROLL FIN DEFLECTIONS

FRONT VIEW

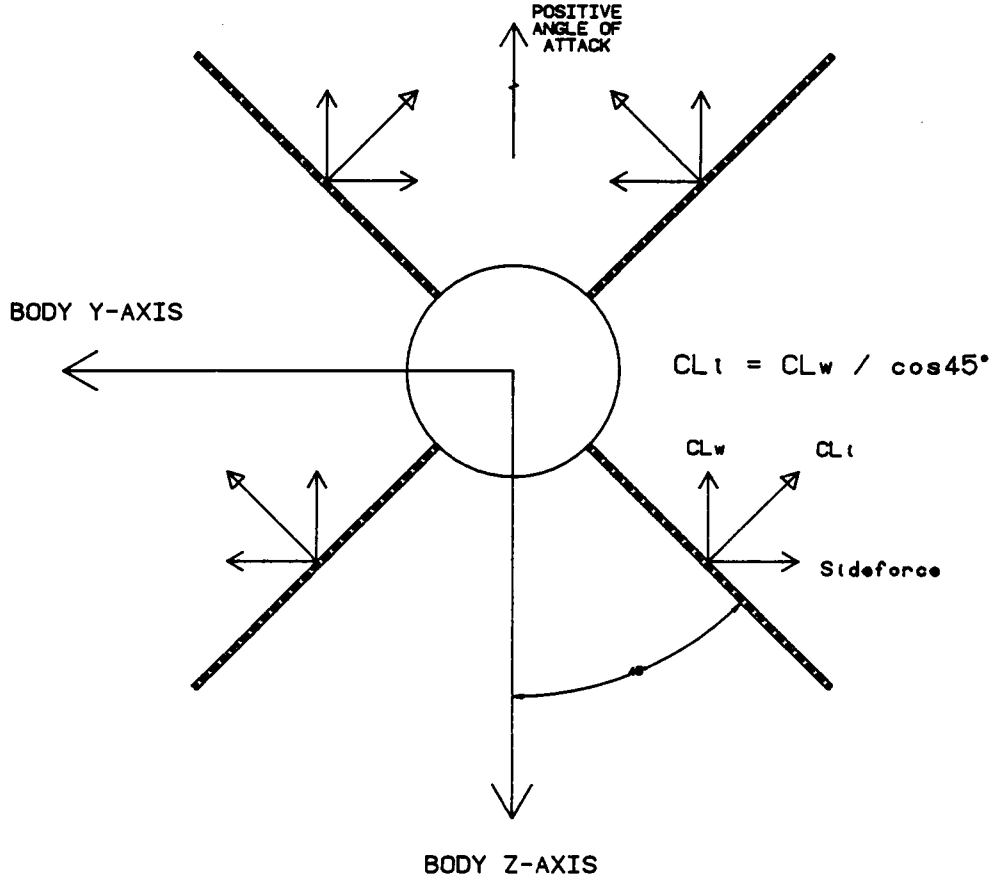

FIGURE 14: LIFT CONTRIBUTION OF WING PLANFORM

FRONT VIEW

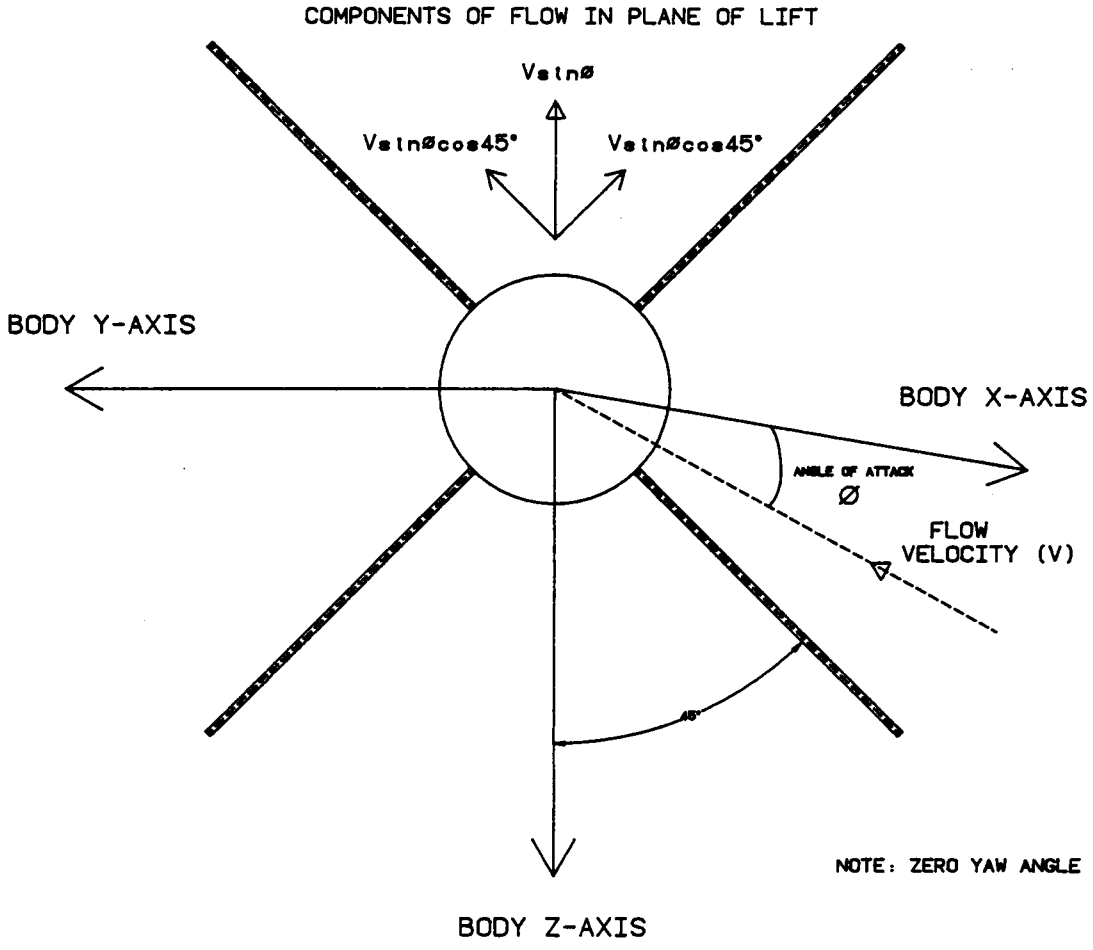

FIGURE 15: EFFECTIVE ANGLE OF ATTACK IN X-CONFIGURATION

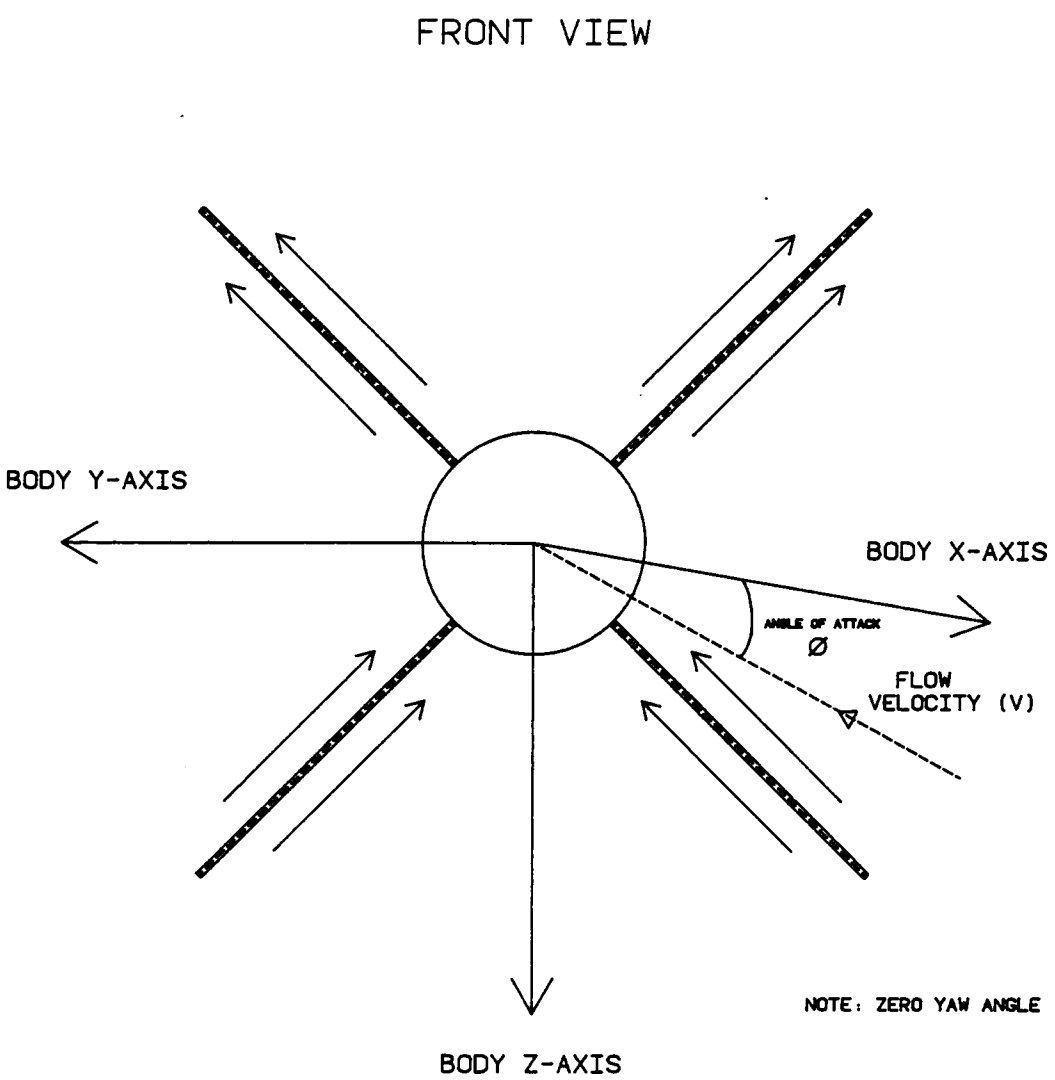

FIGURE 16: SPANWISE COMPONENT OF FREE STREAM

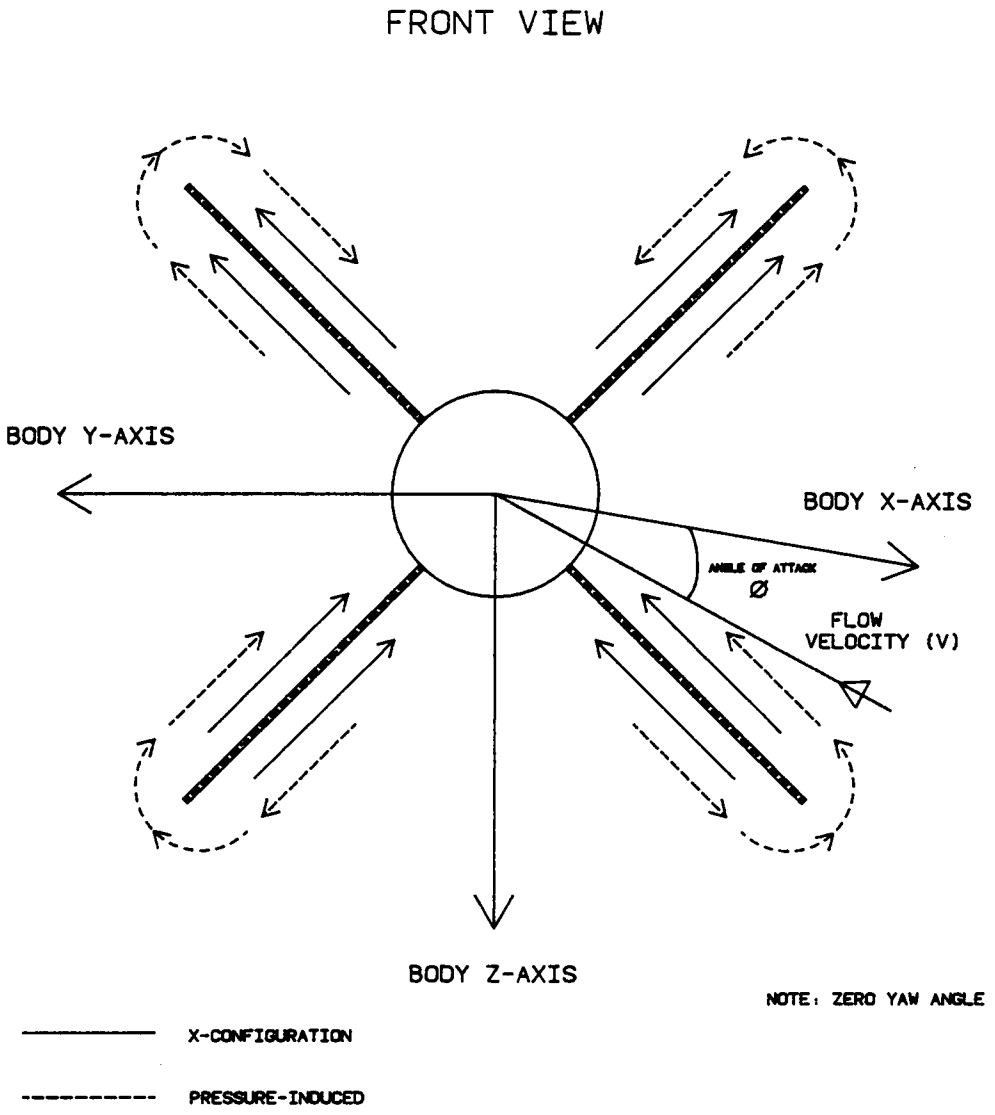

FIGURE 17: SUPERPOSITION OF X-CONFIGURATION AND PRESSURE-INDUCED SPANWISE FLOWS

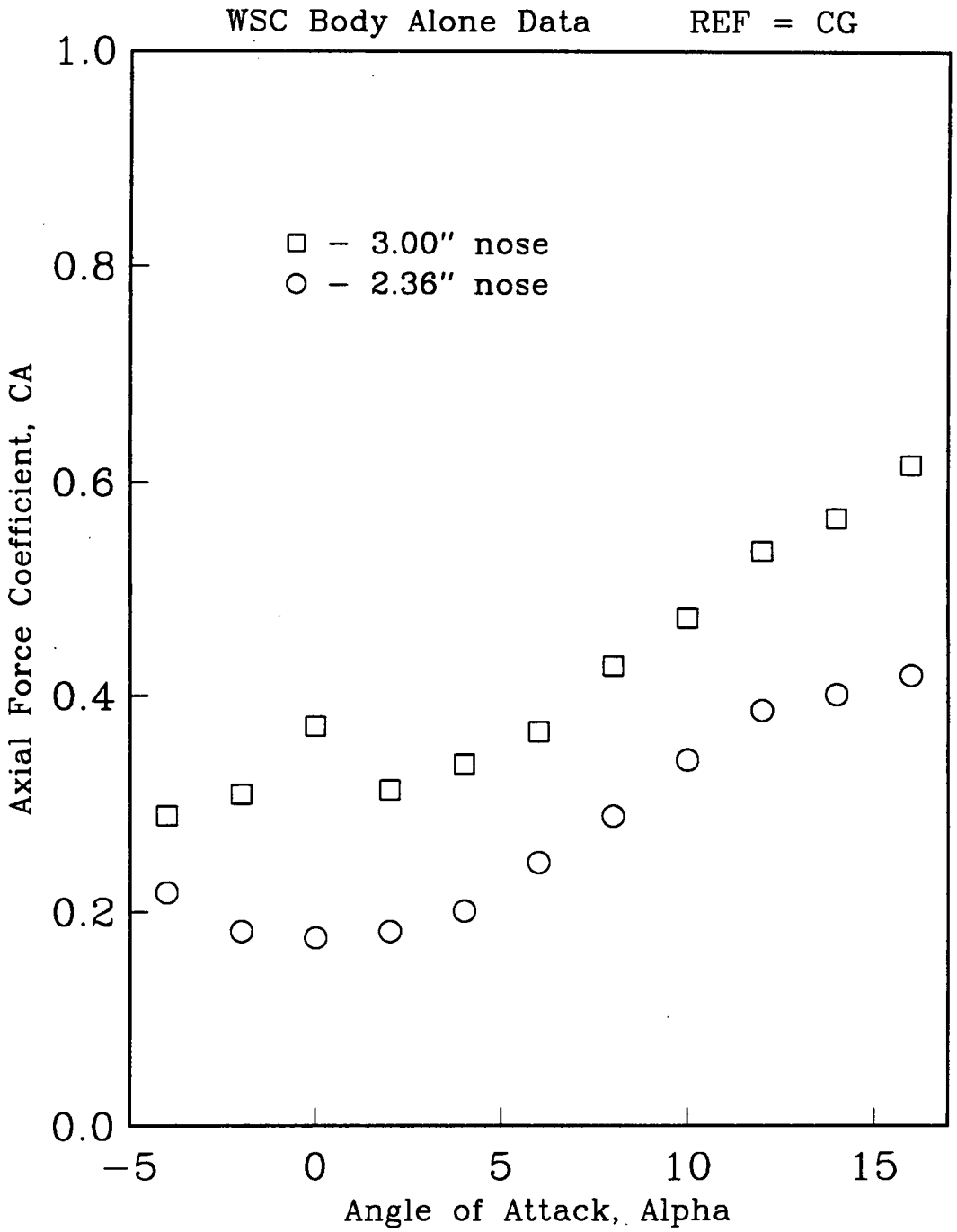

Figure 18a: Nose Effect on CA (B1)

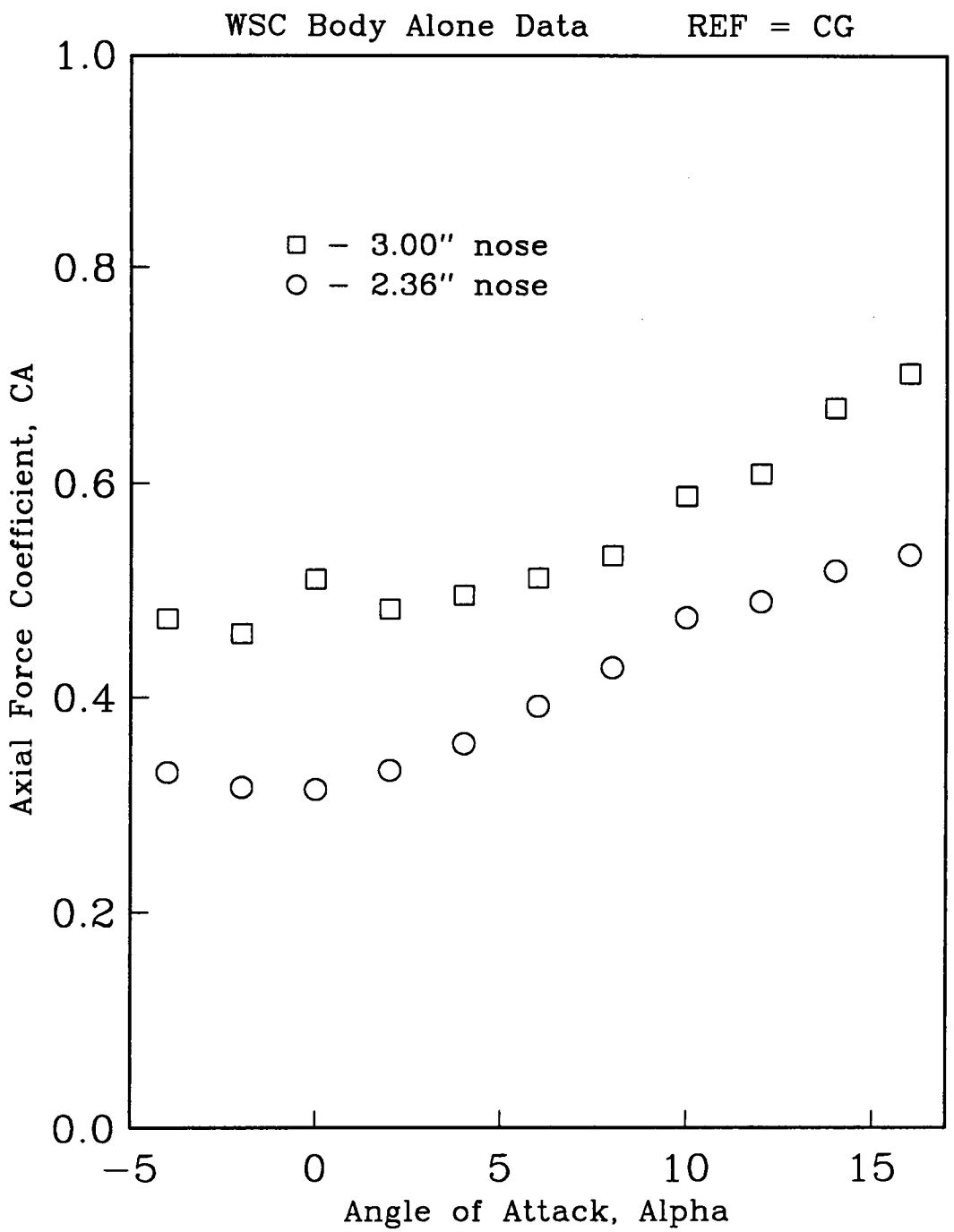

Figure 18b: Nose Effect on CA (B2)

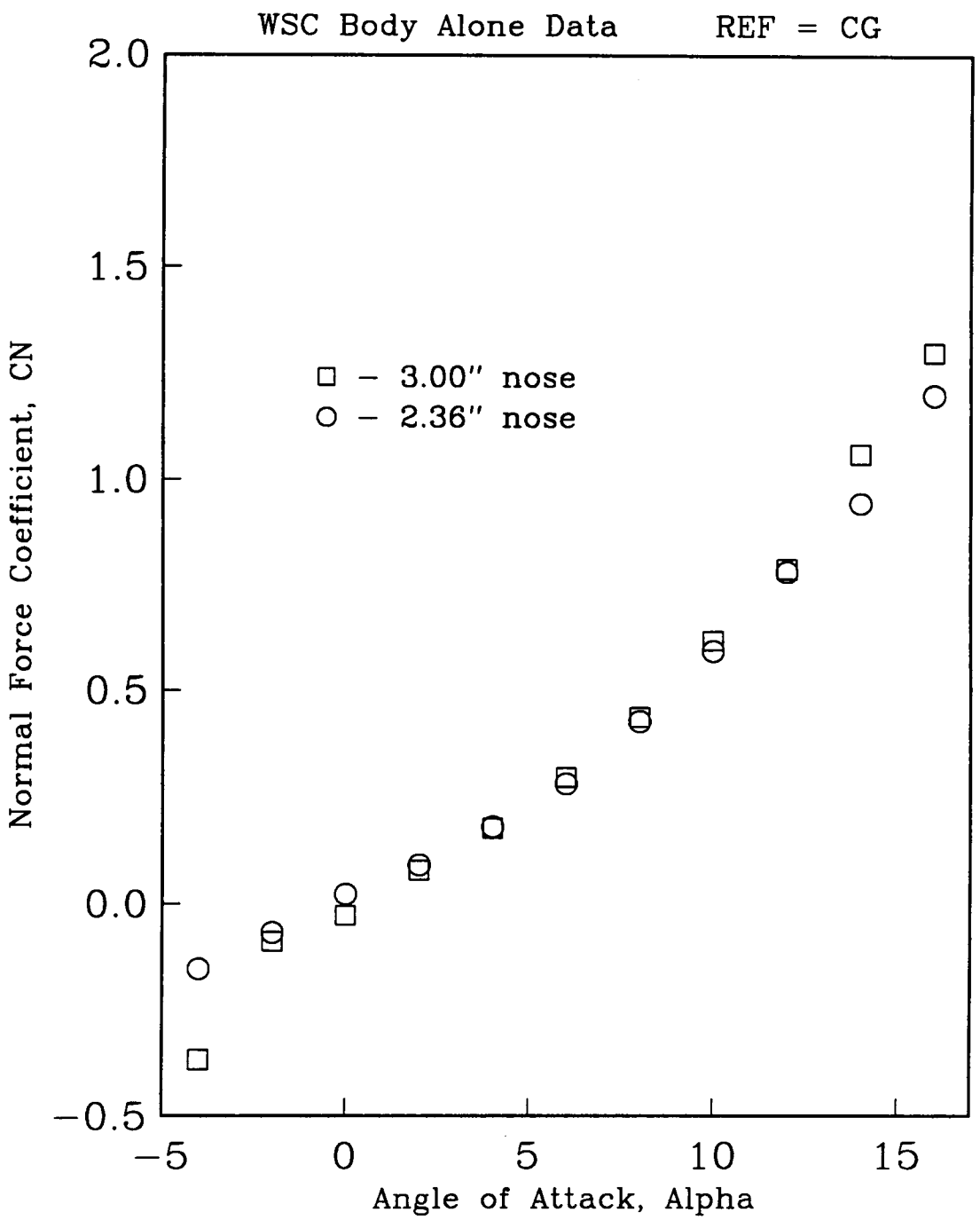

Figure 19a: Nose Effect on CN (B1)

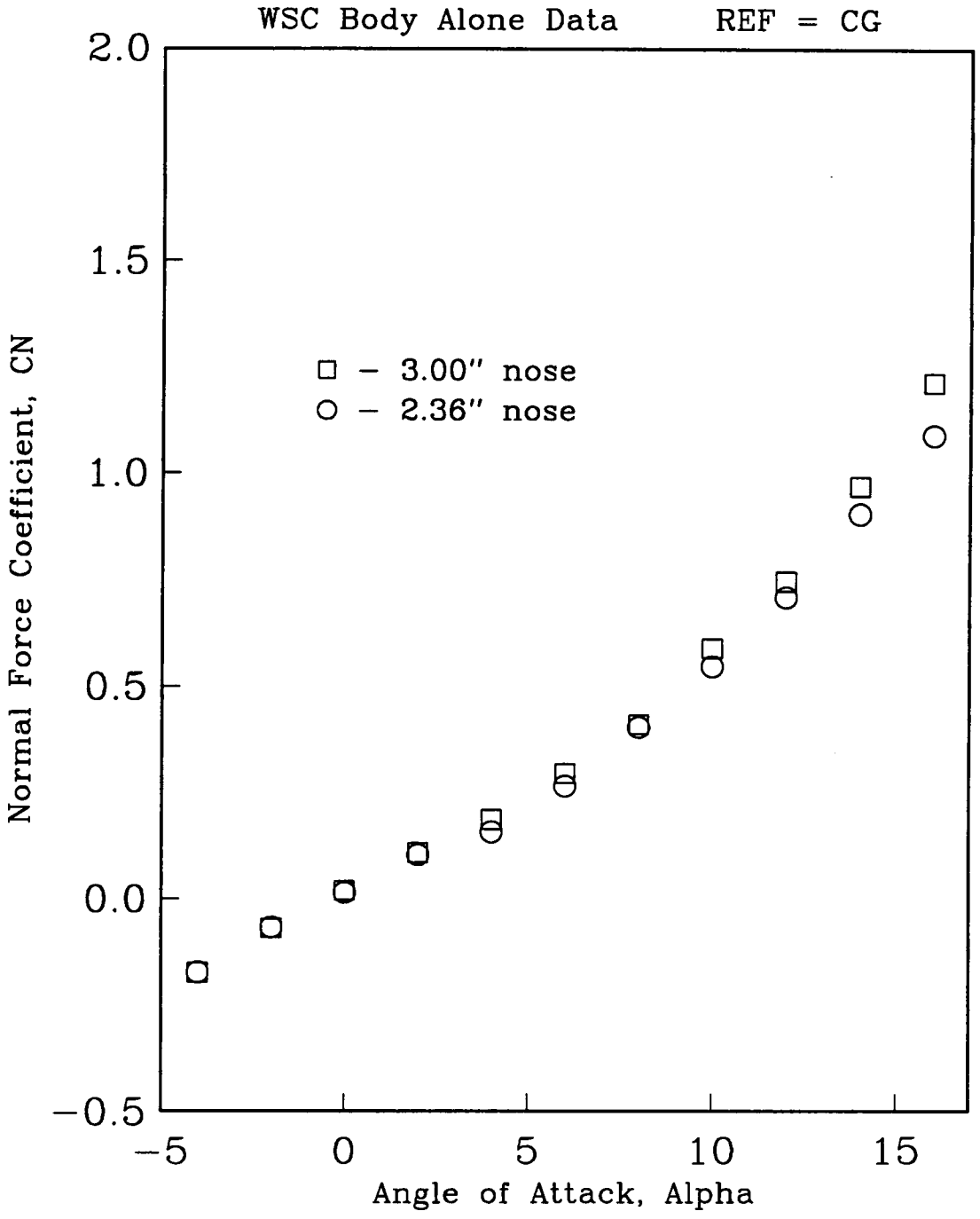

Figure 19b: Nose Effect on CN (B2)

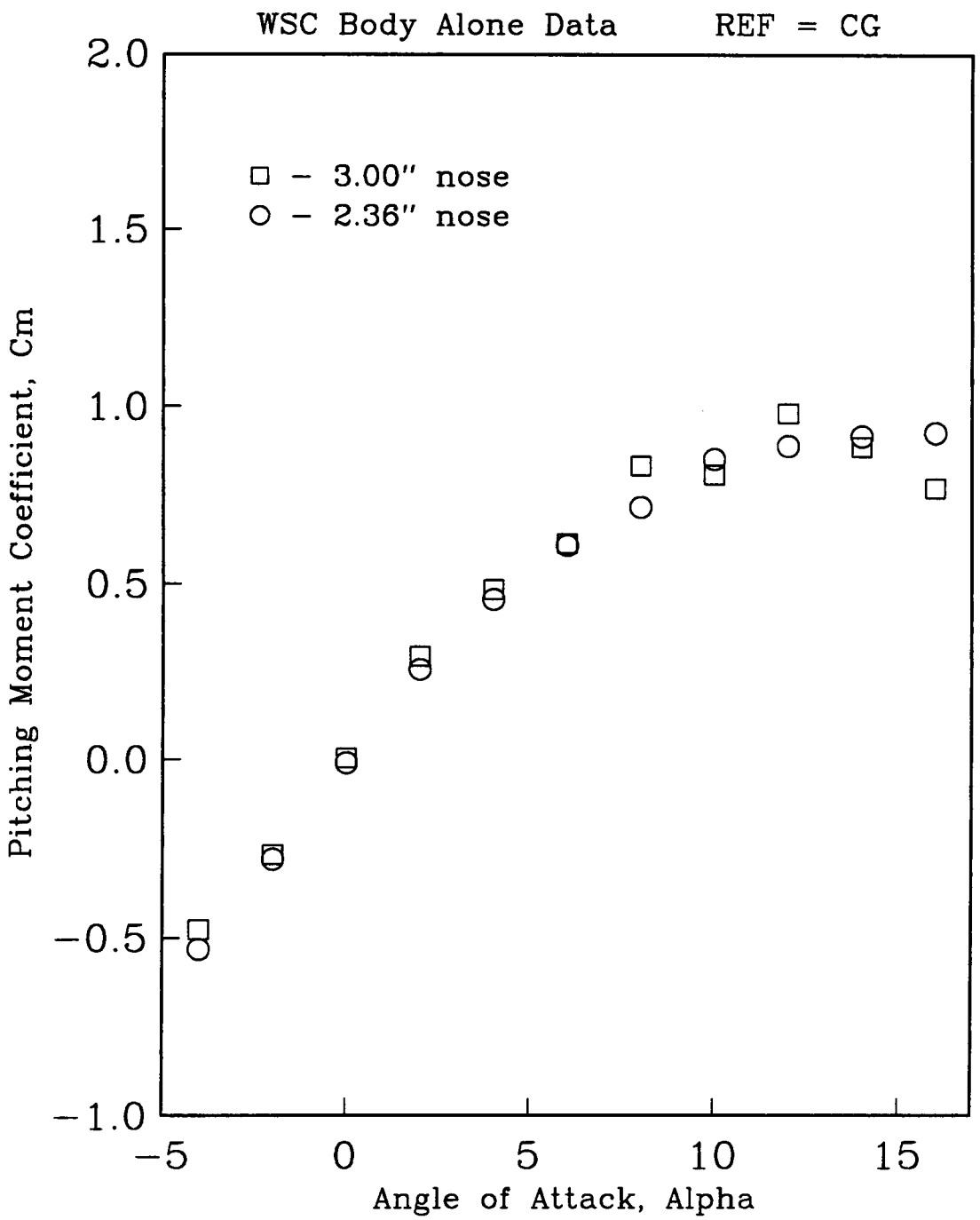

Figure 20a: Nose Effect on Cm (B1)

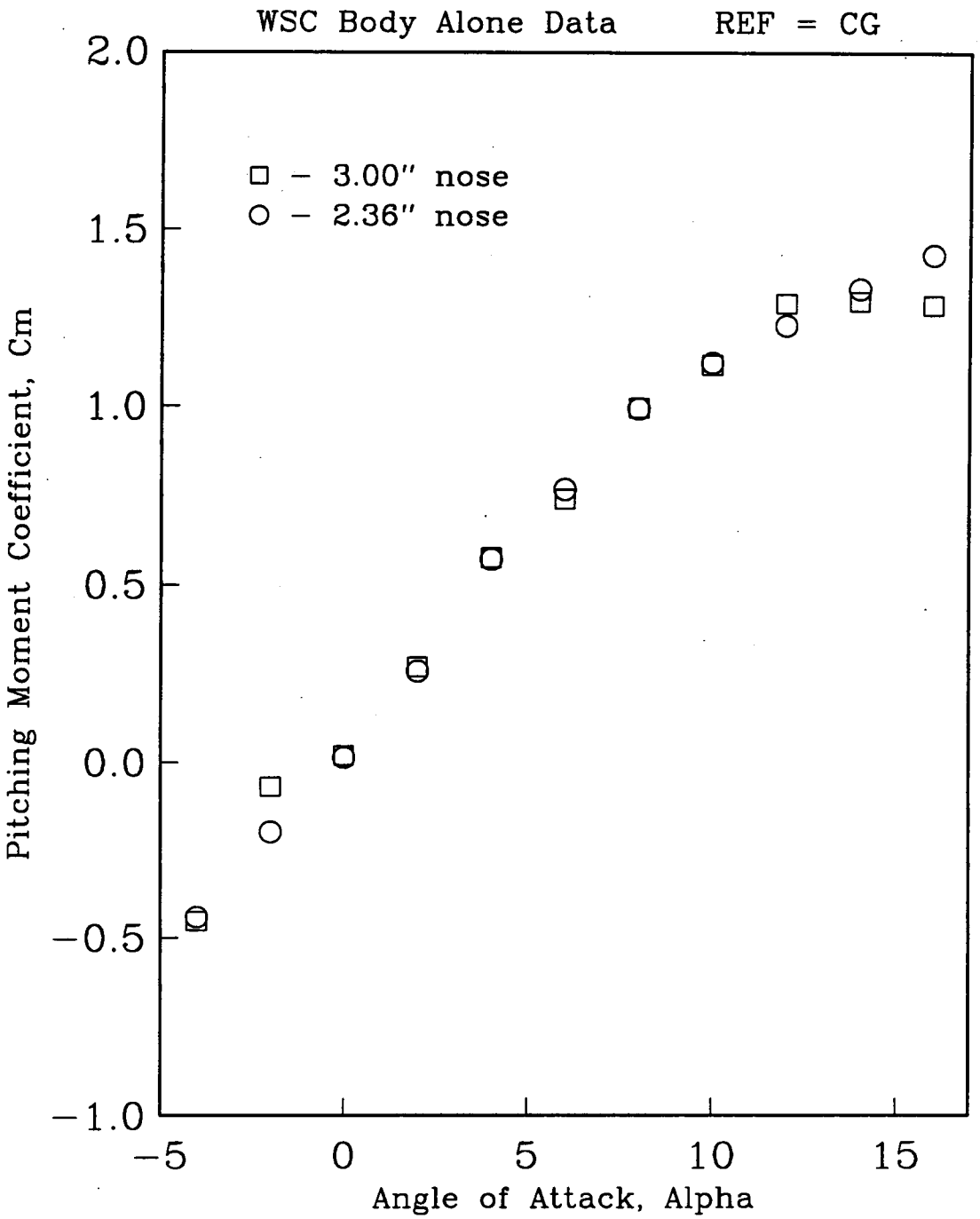

Figure 20b: Nose Effect on Cm (B2)

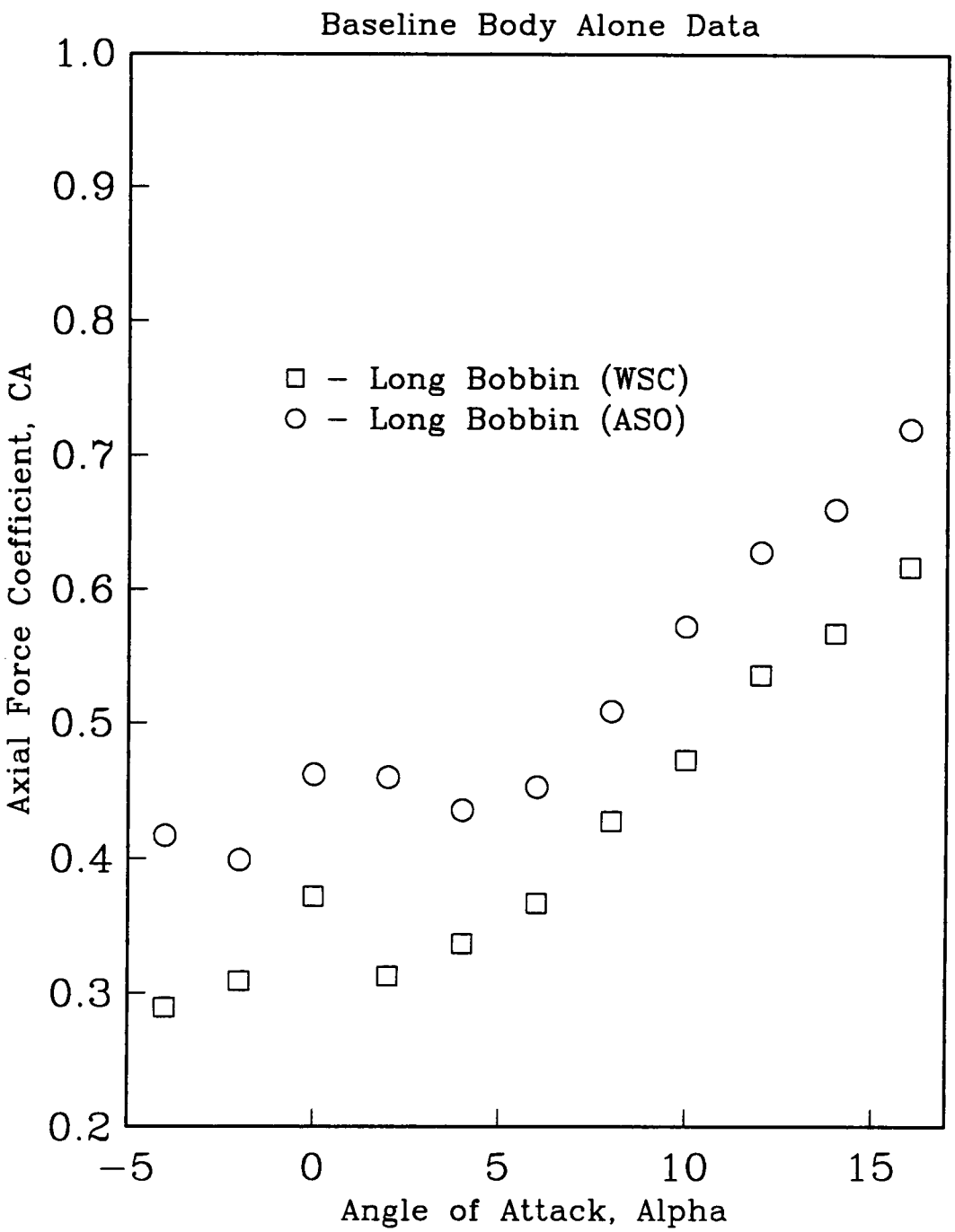

Figure 21a: Wing Slot Effect on CA (B1)

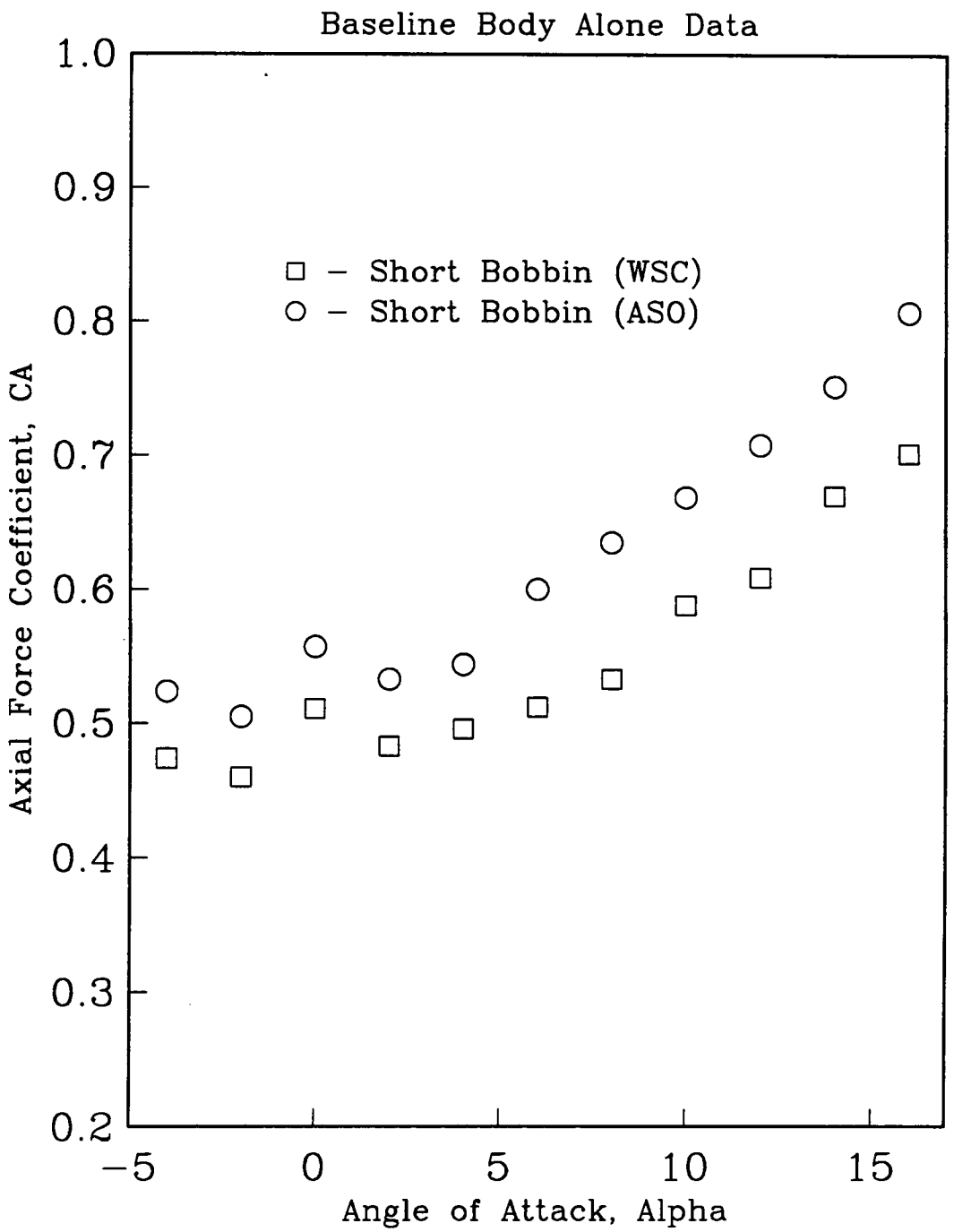

Figure 21b: Wing Slot Effect on CA (B2)

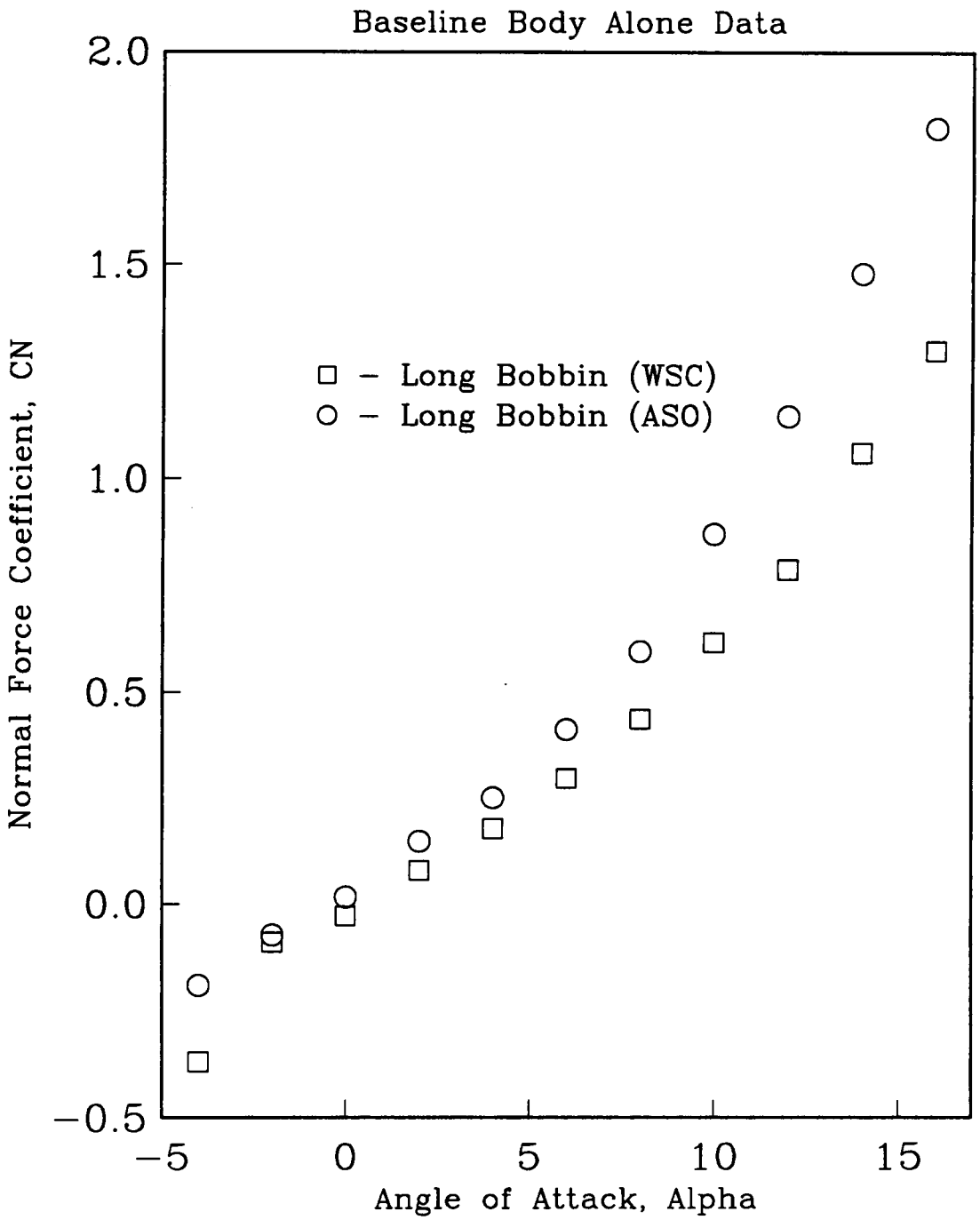

Figure 22a: Wing Slot Effect on CN (B1)

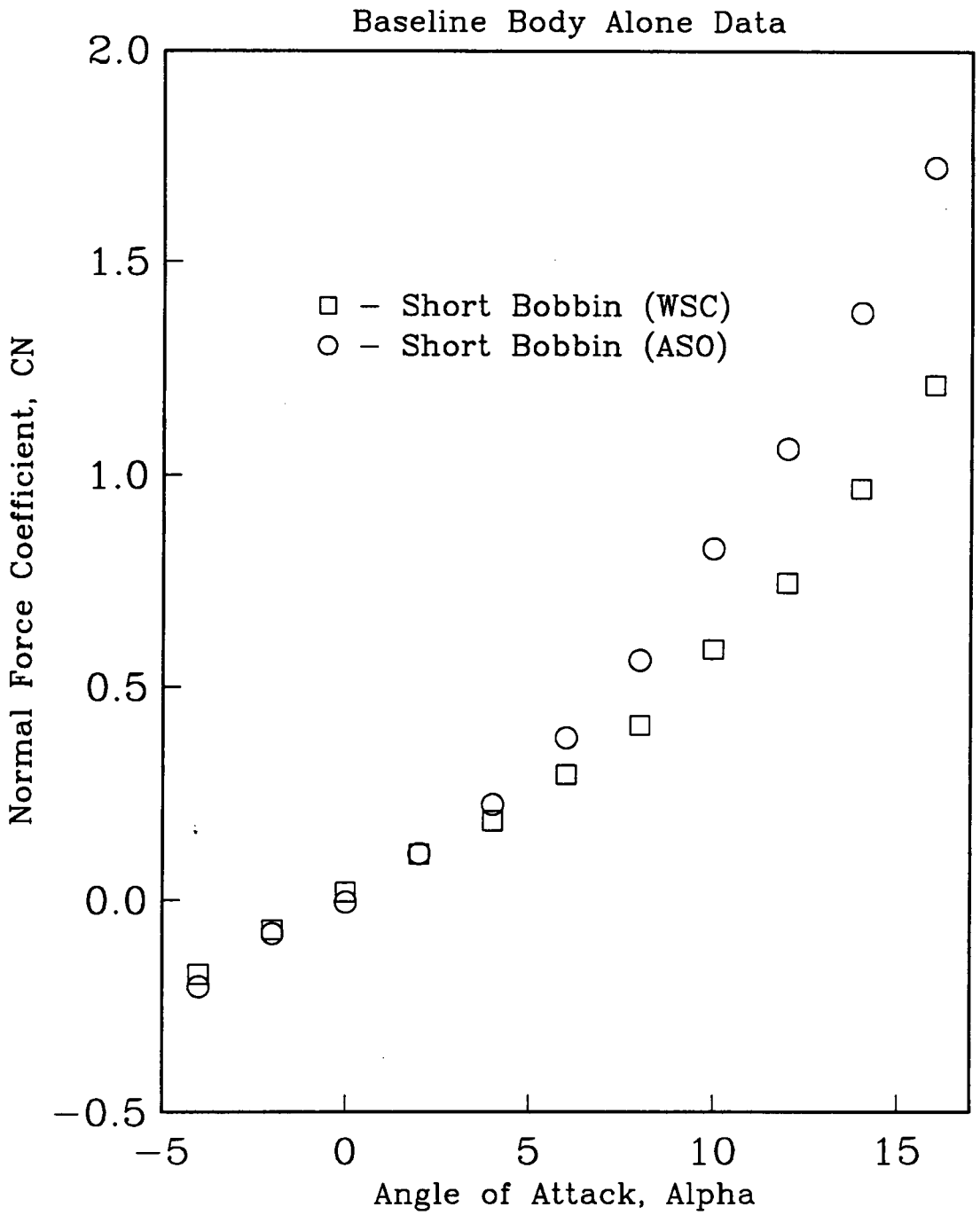

Figure 22b: Wing Slot Effect on CN (B2)

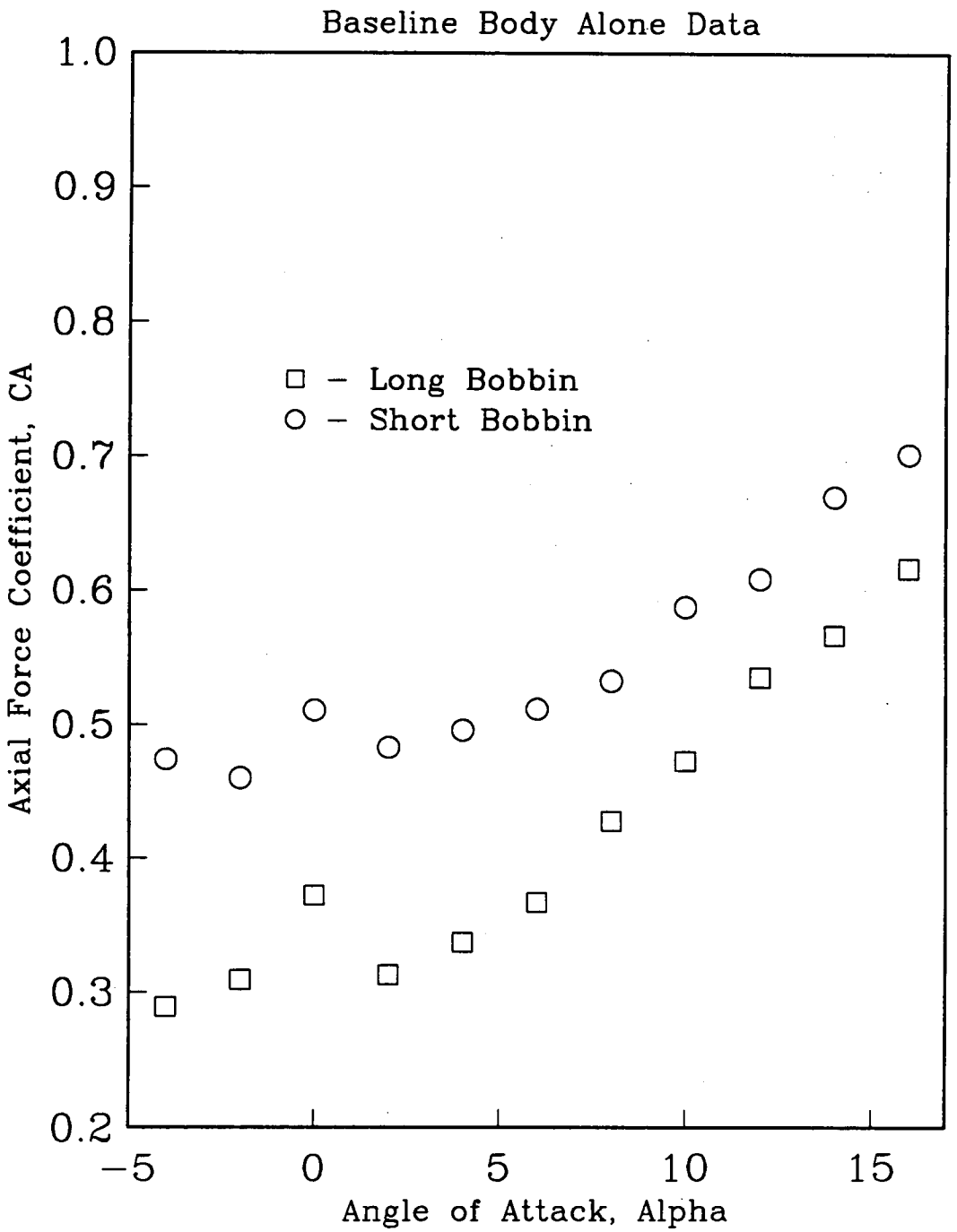

Figure 23a: Bobbin Effect on CA (WSC)

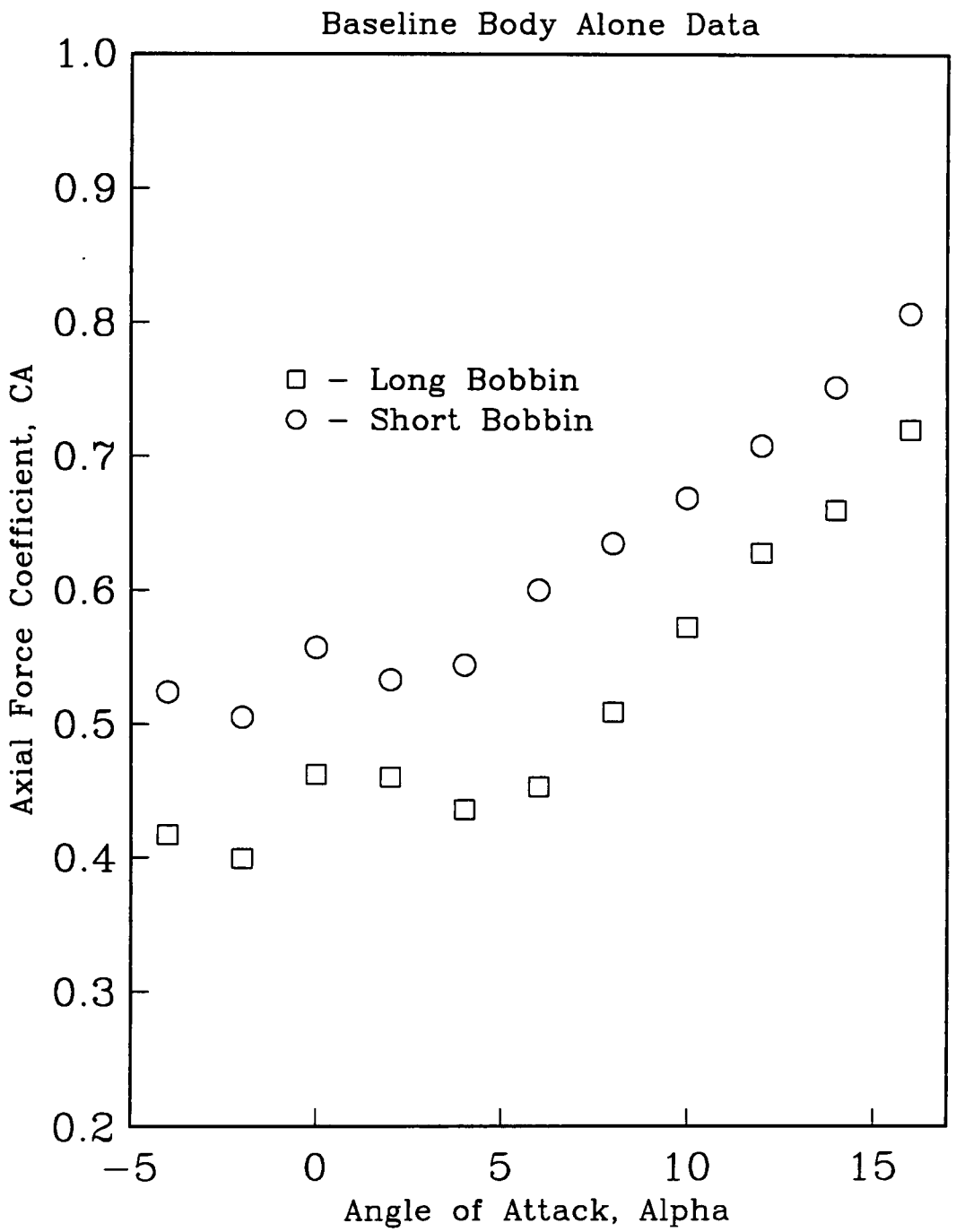

Figure 23b: Bobbin Effect on CA (ASO)

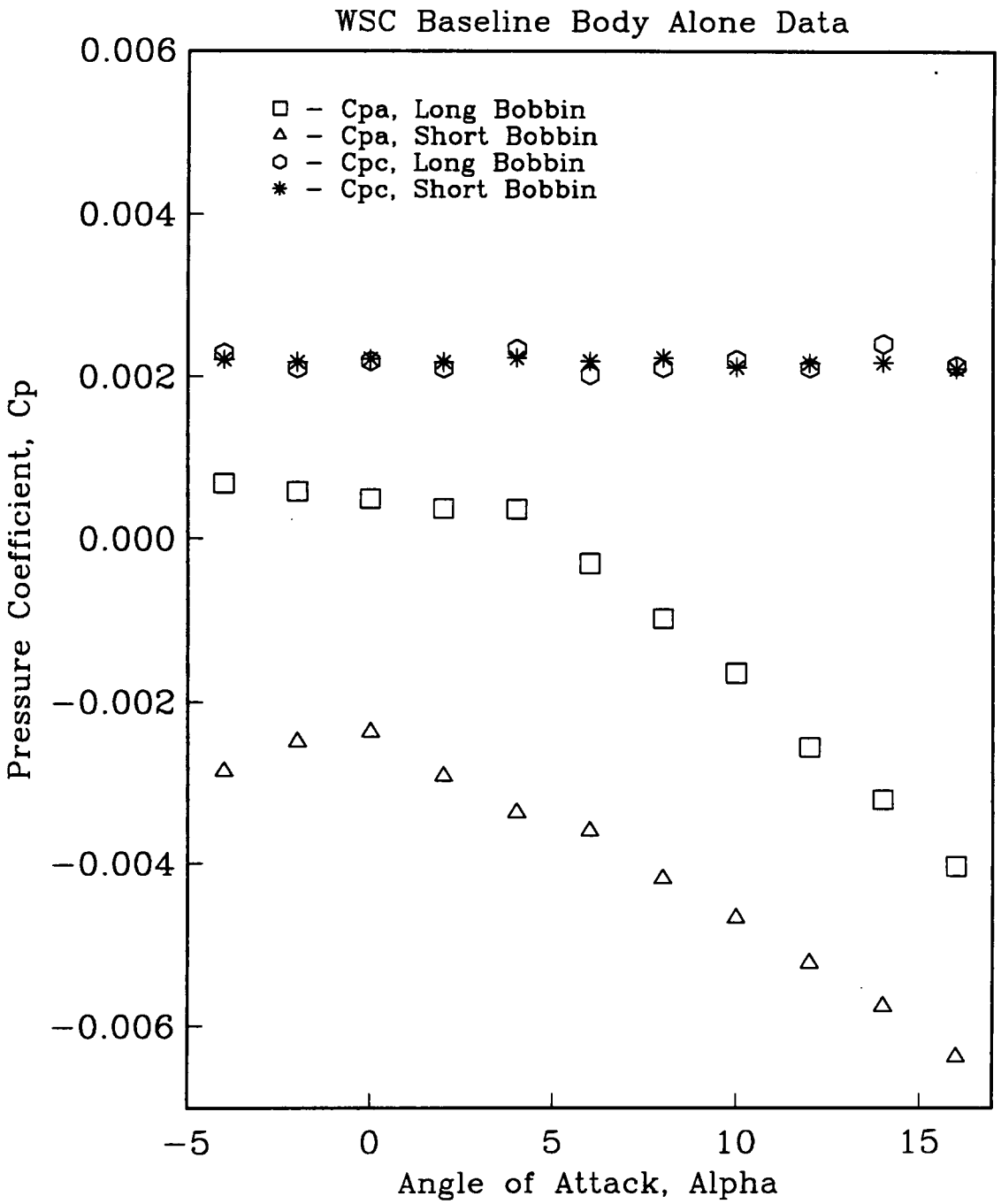

Figure 24: Annular & Cavity Pressure Readings

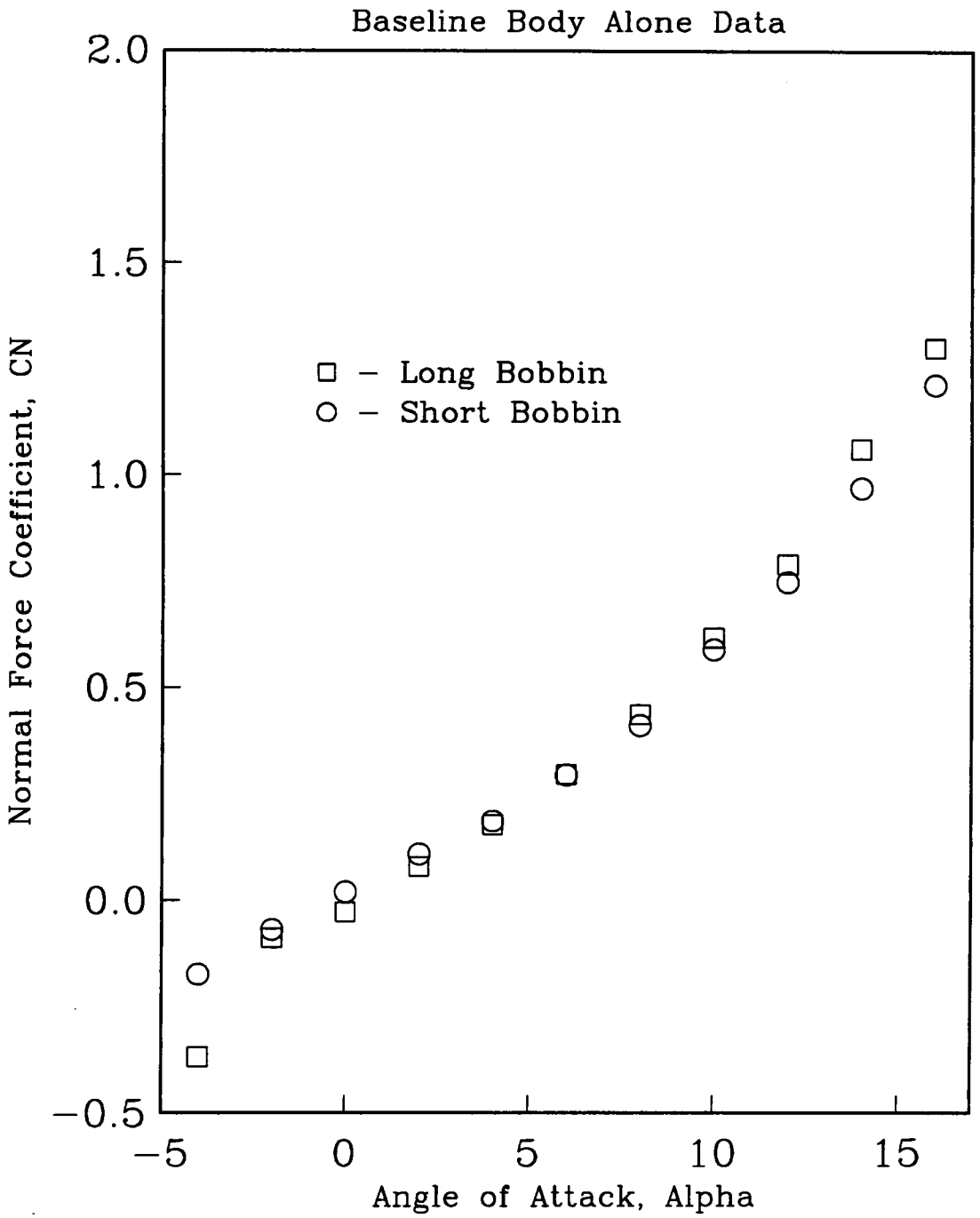

Figure 25a: Bobbin Effect on CN (WSC)

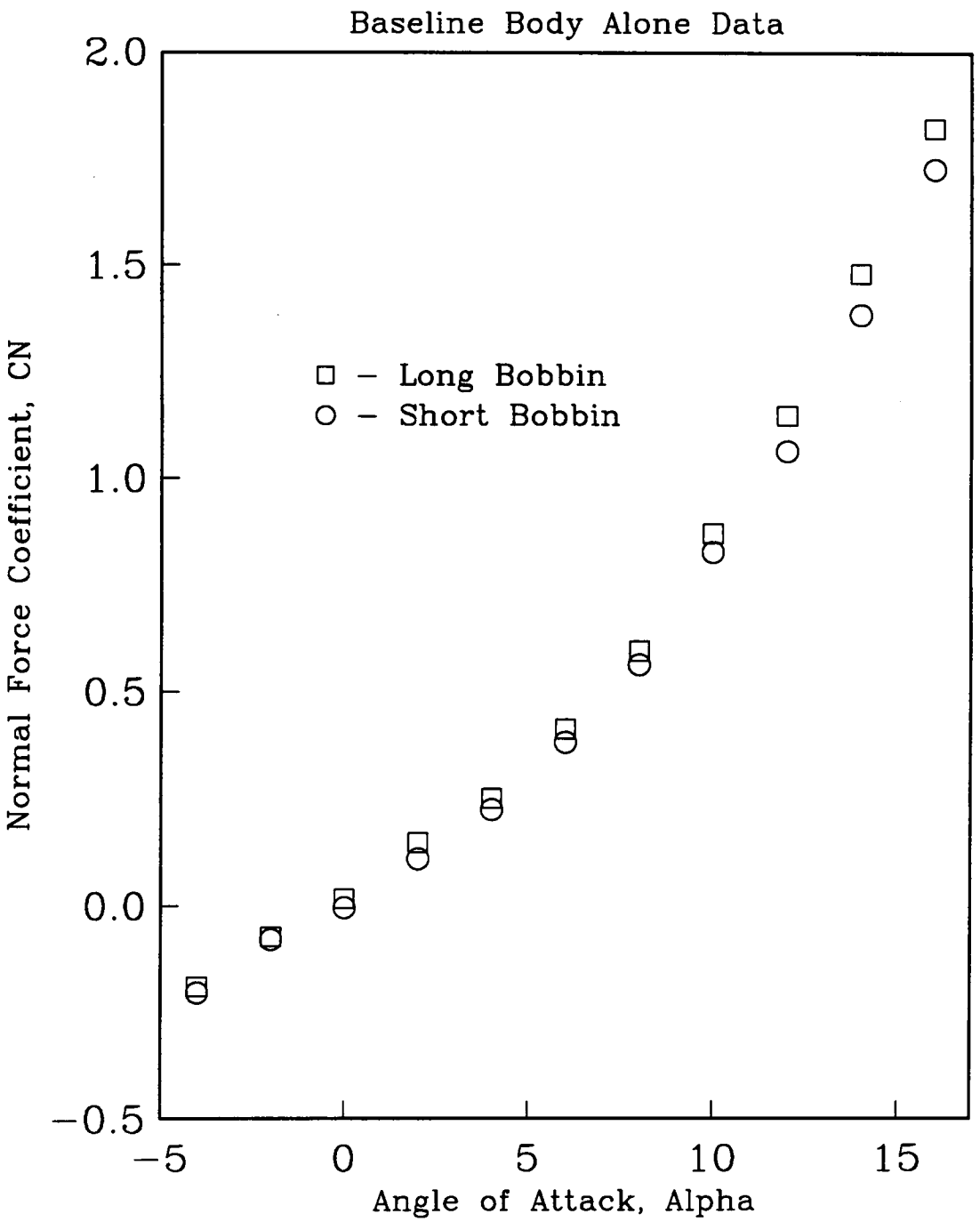

Figure 25b: Bobbin Effect on CN (ASO)

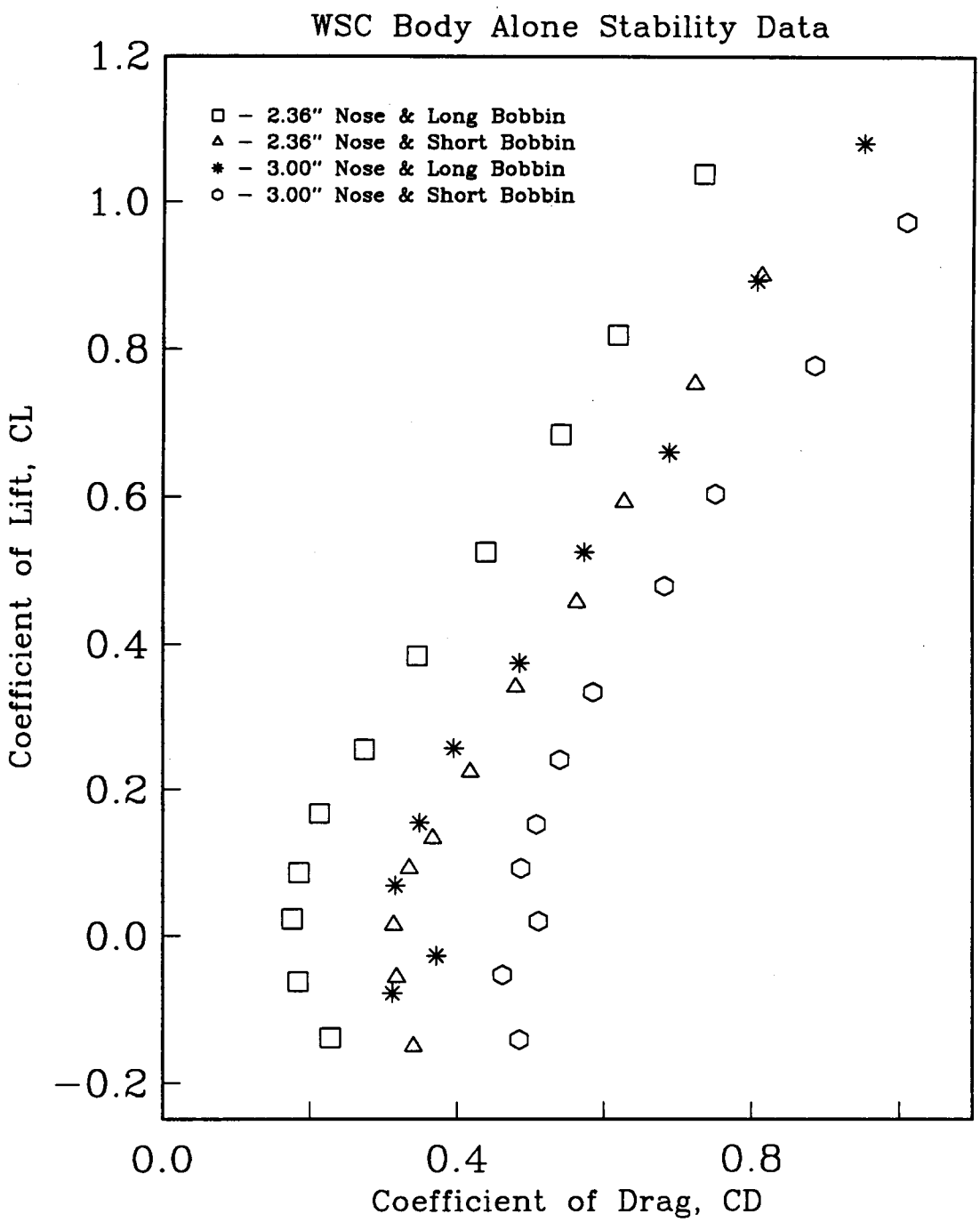

Figure 26: CL vs CD Body-Alone Data

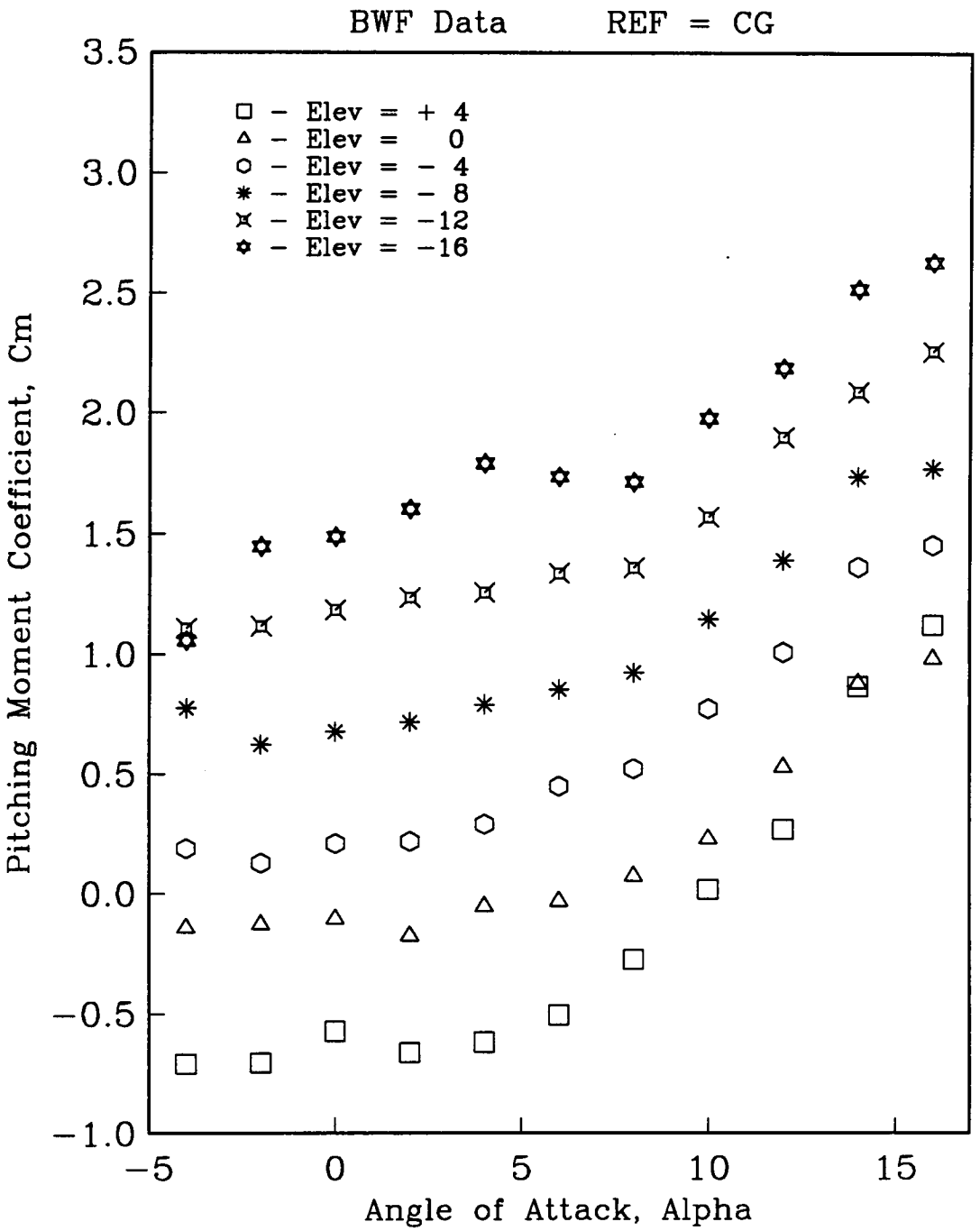

Figure 27a: Cm Elevator Deflection B1F1Be0

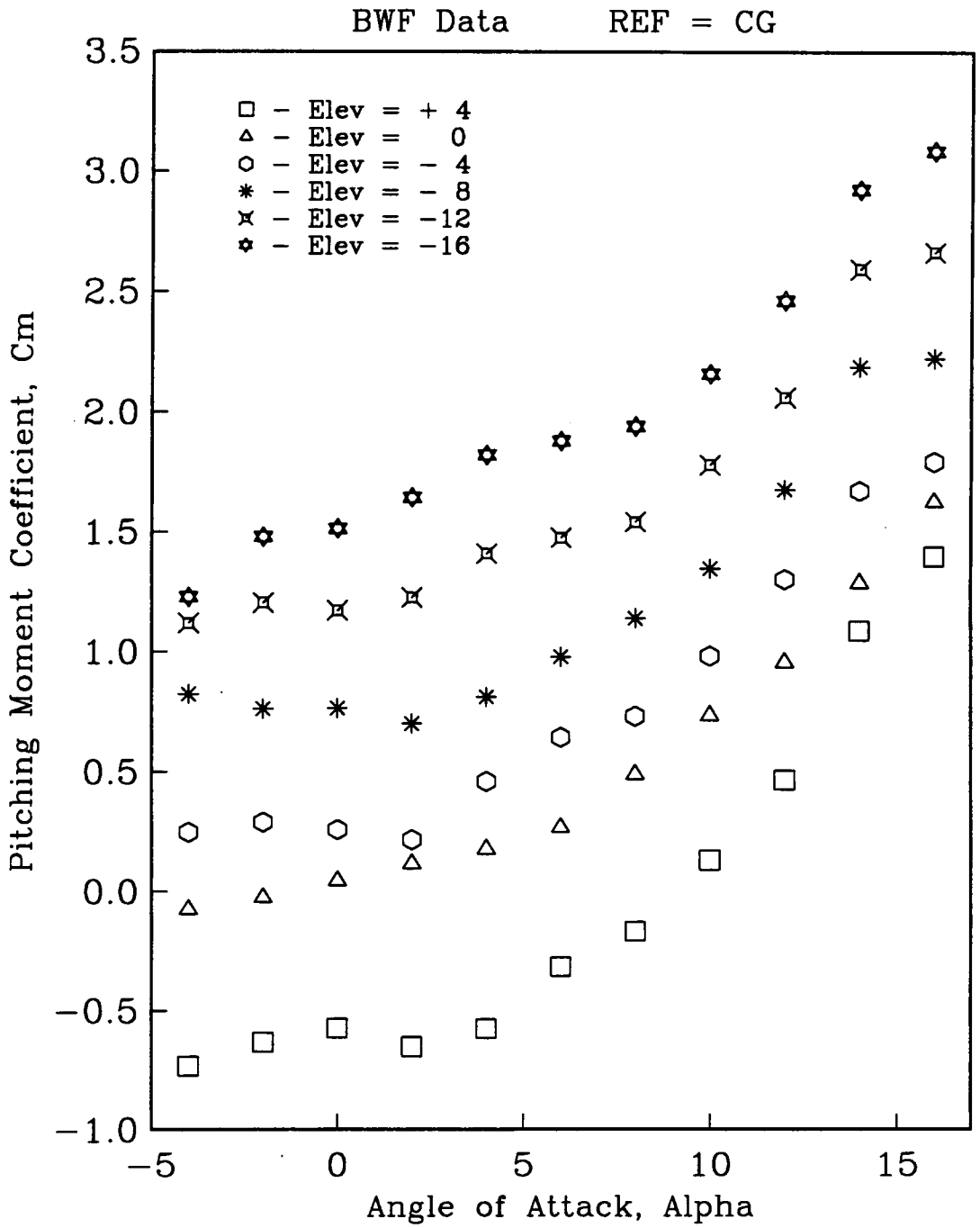

Figure 27b: Cm Elevator Deflection B2F1Be0

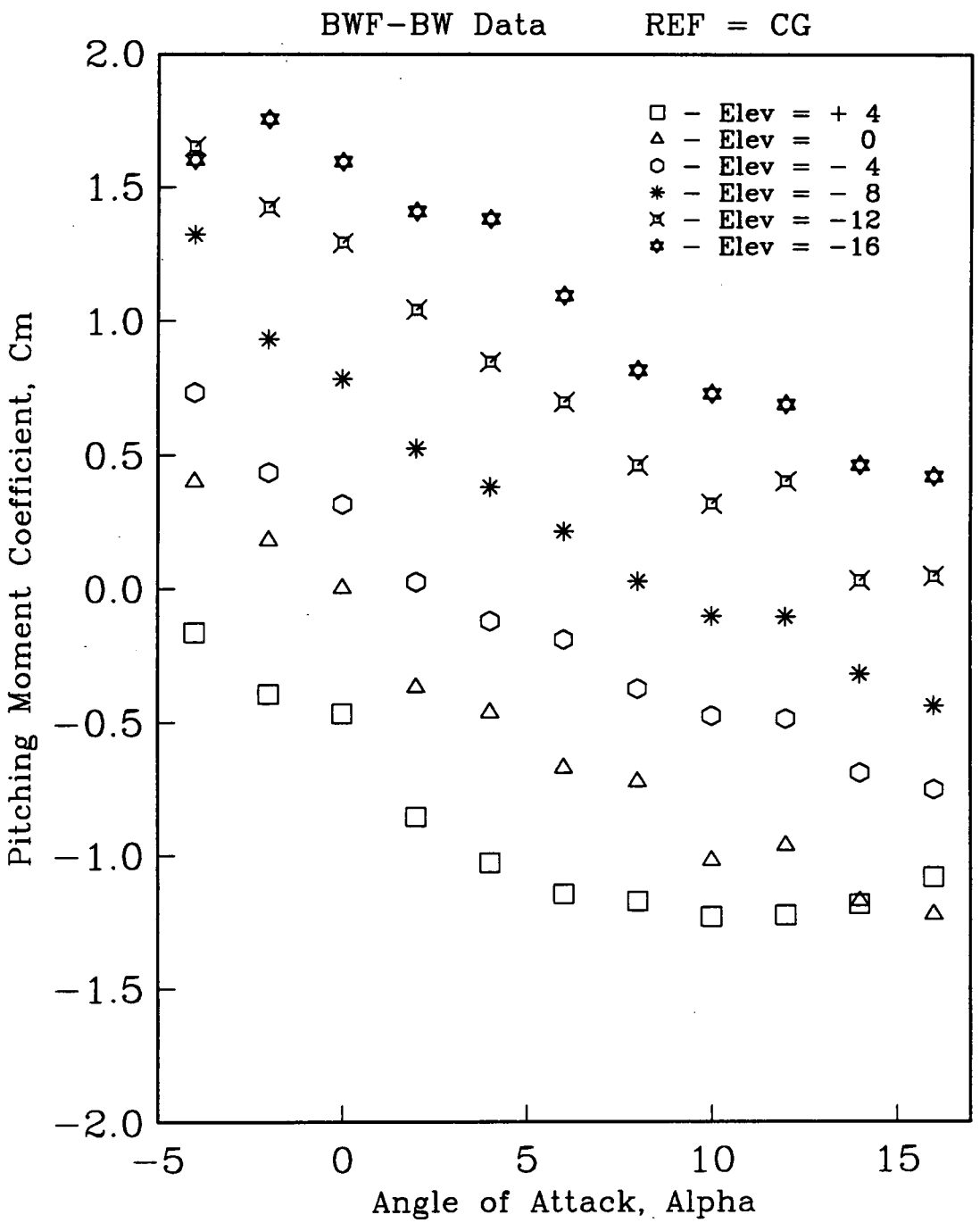

Figure 28a: Cm Fin Effectiveness B1F1Be0

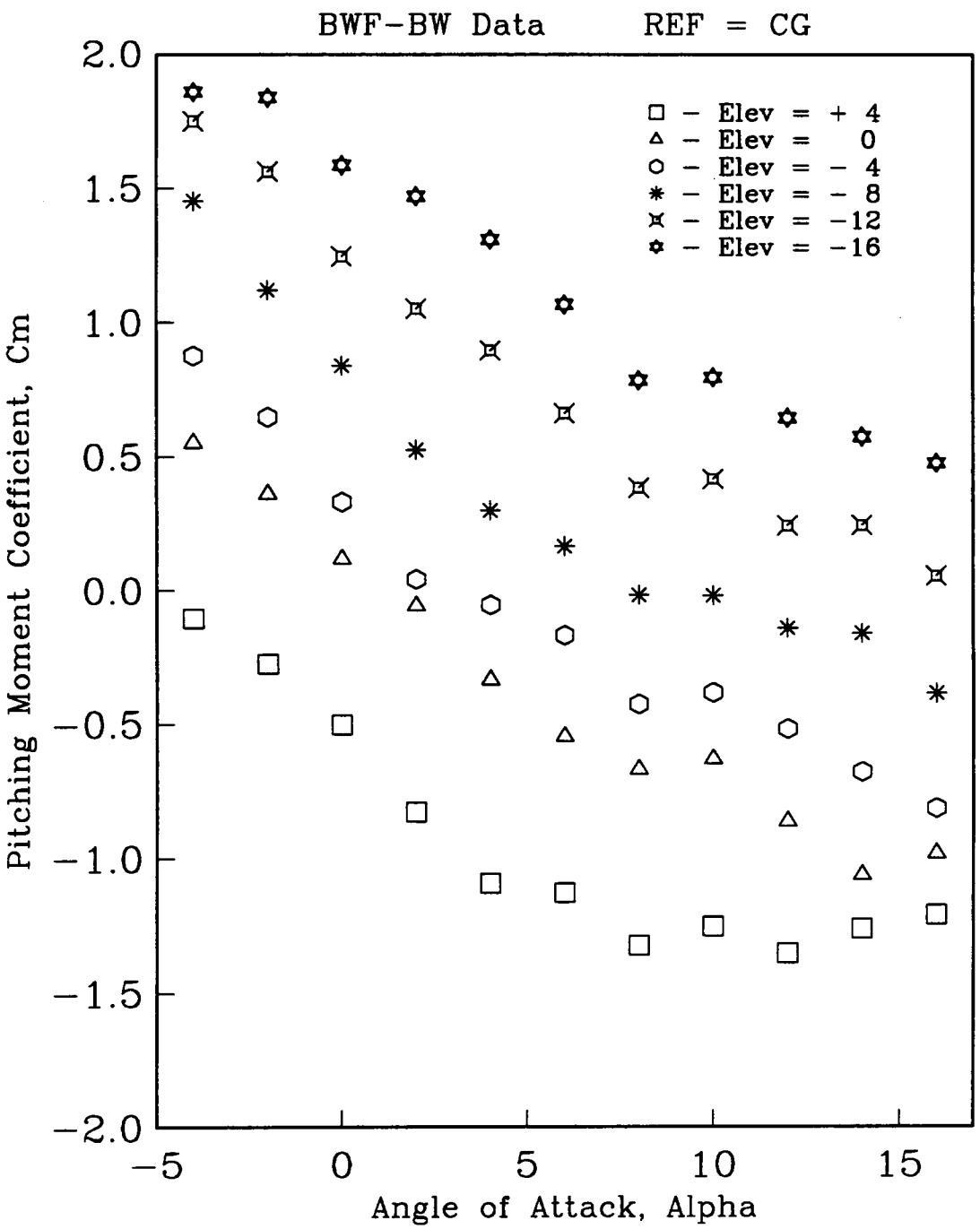

Figure 28b: Cm Fin Effectiveness B2F1Be0

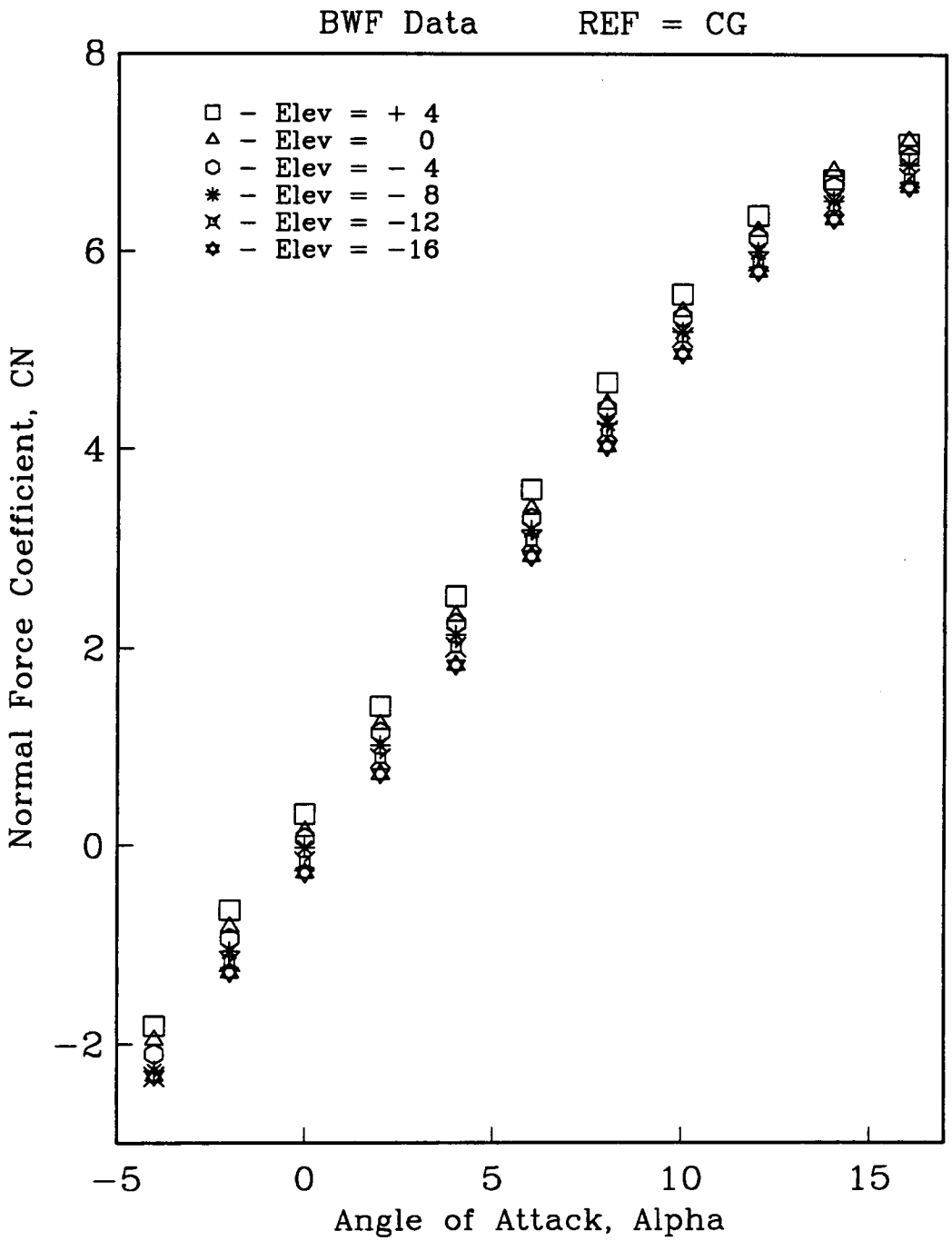

Figure 29a: CN Elevator Deflection B1F1Be0

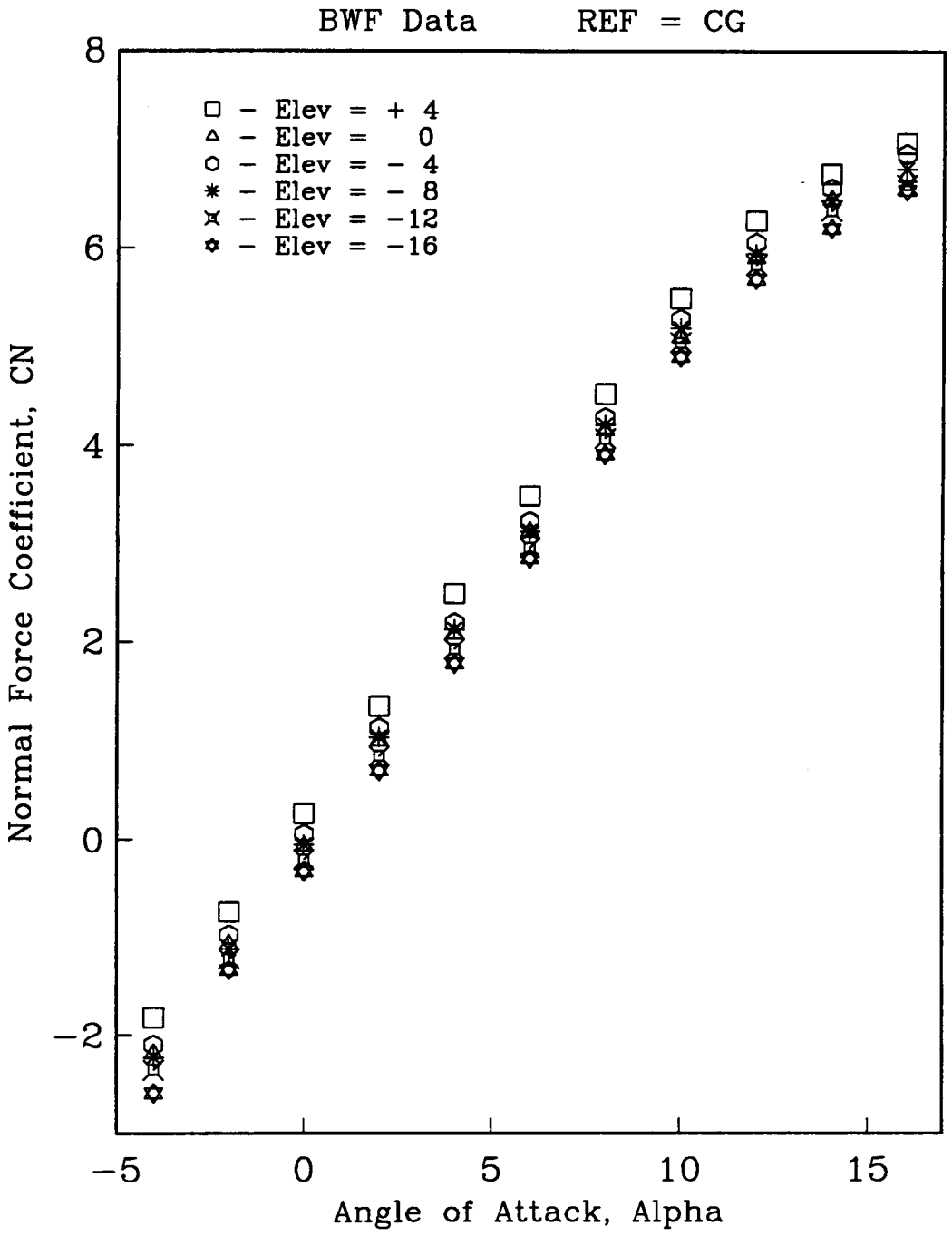

Figure 29b: CN Elevator Deflection B2F1Be0

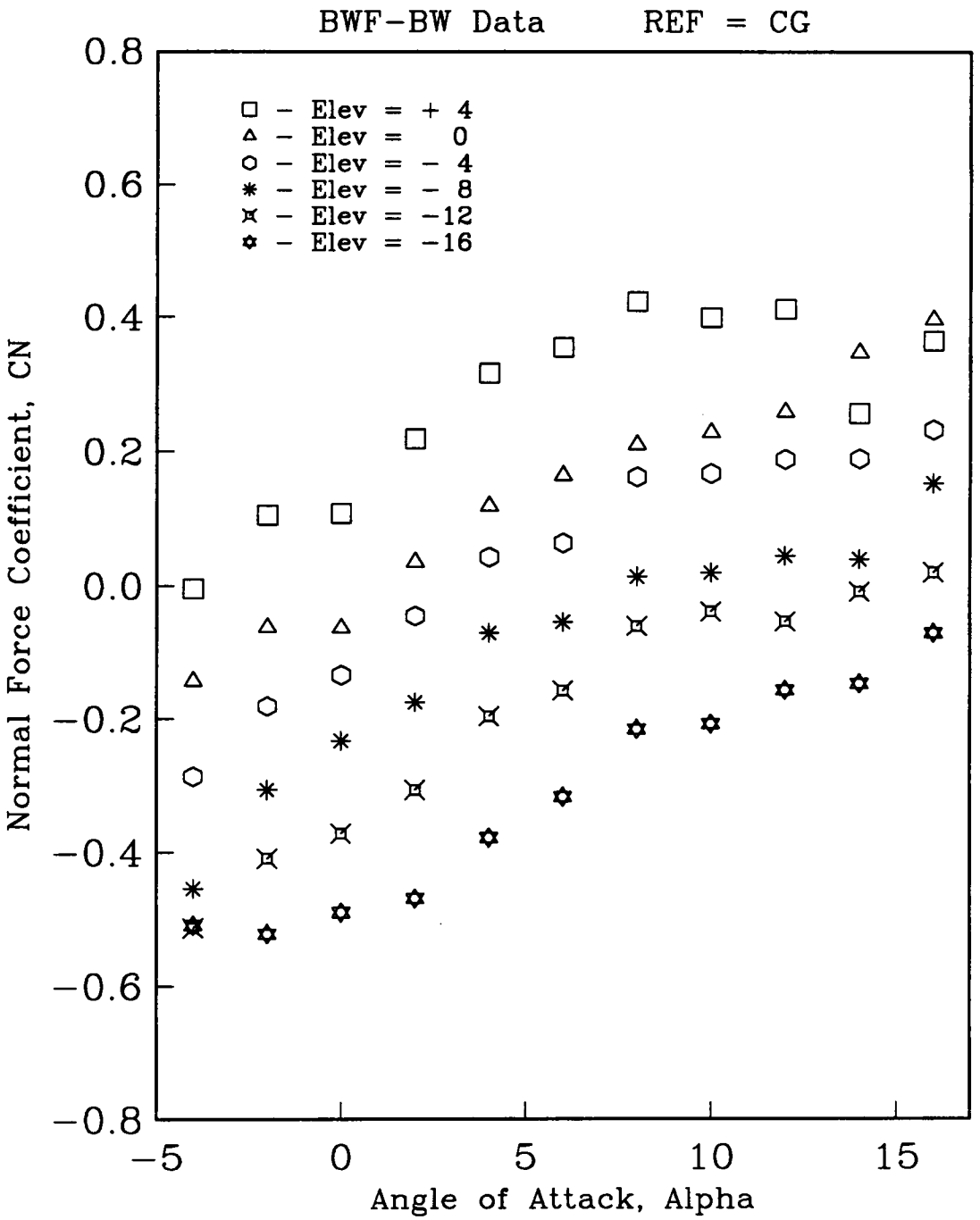

Figure 30a: CN Fin Effectiveness B1F1Be0

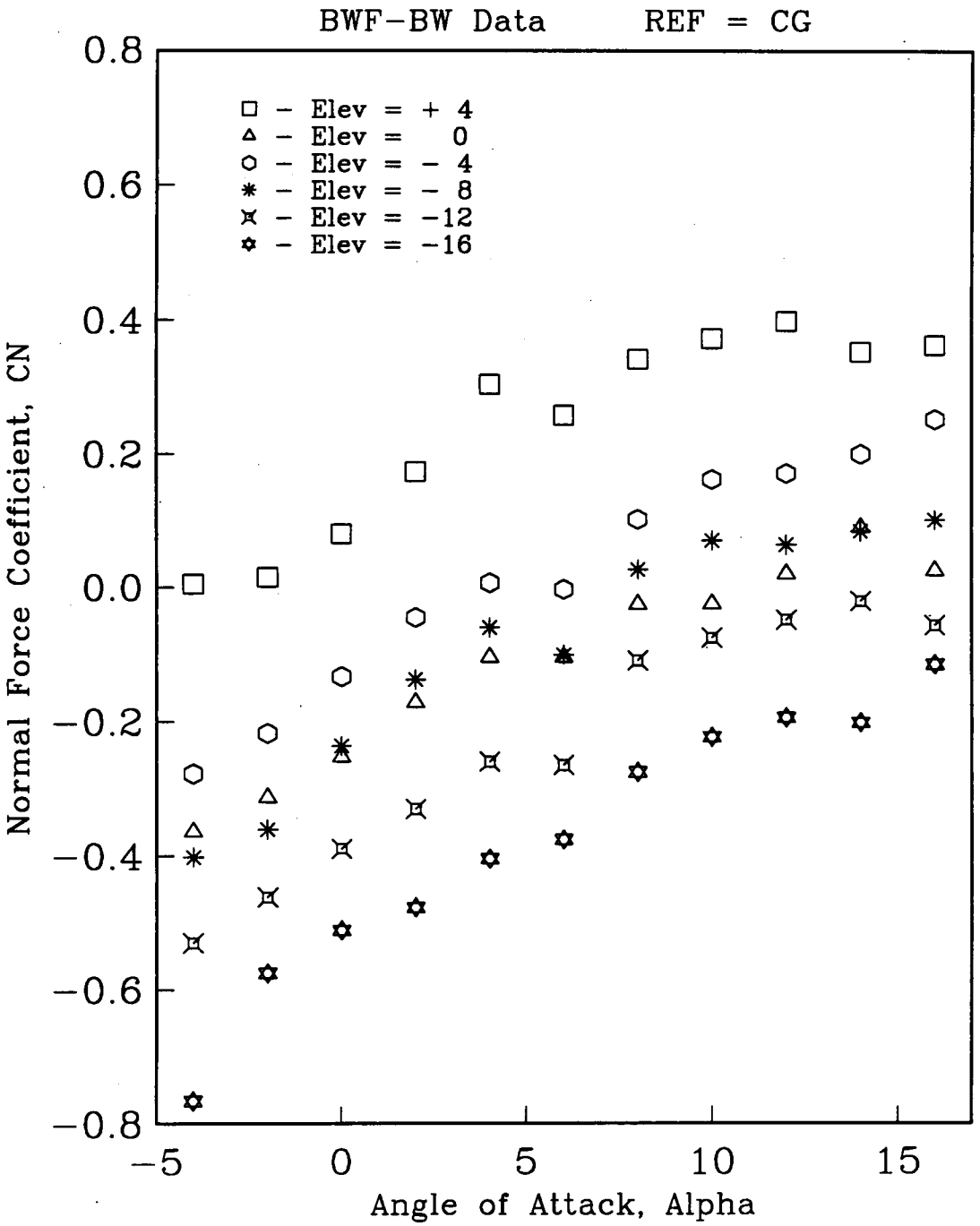

Figure 30b: CN Fin Effectiveness B2F1Be0

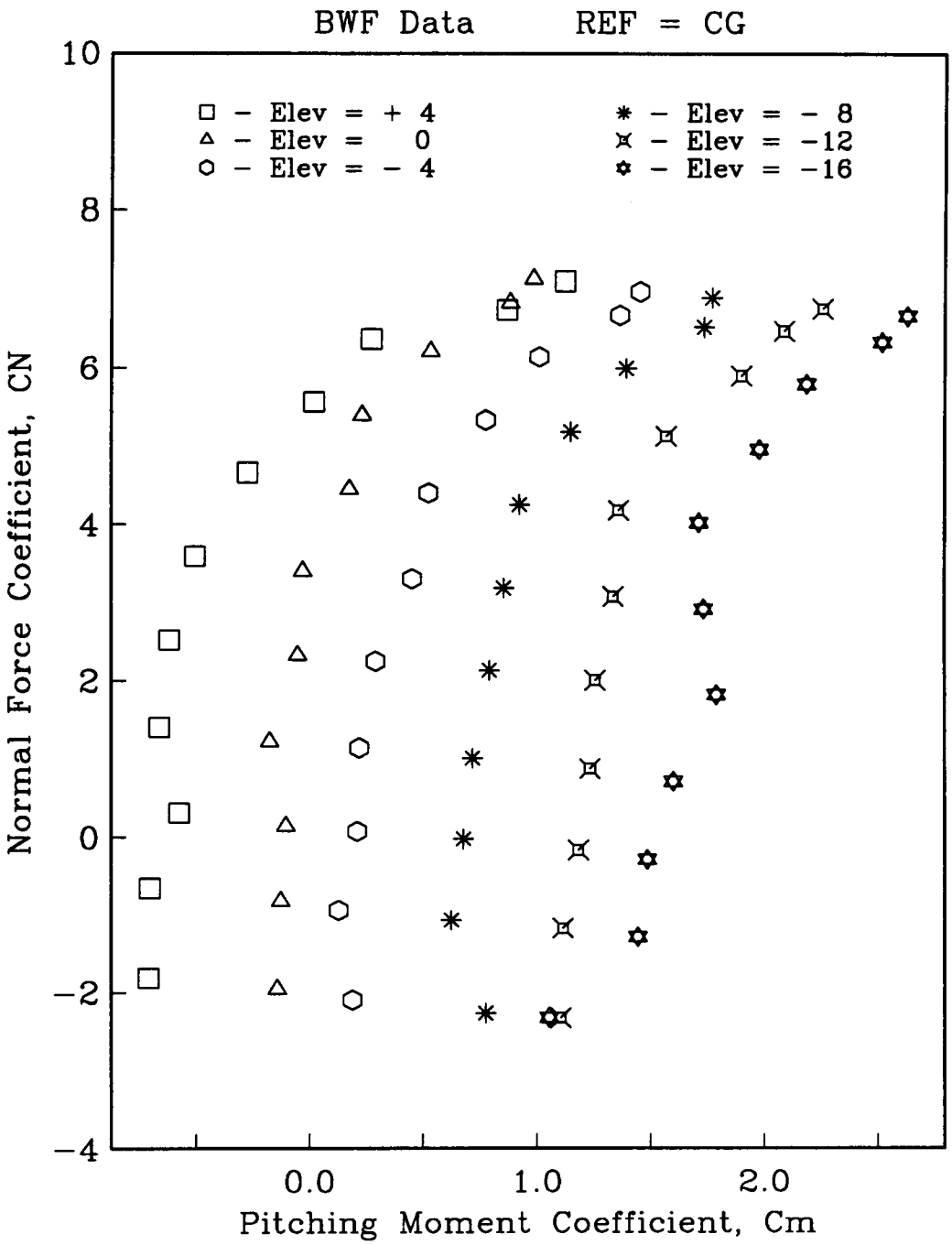

Figure 31a: CN vs Cm Elevator Deflection B1F1Be0

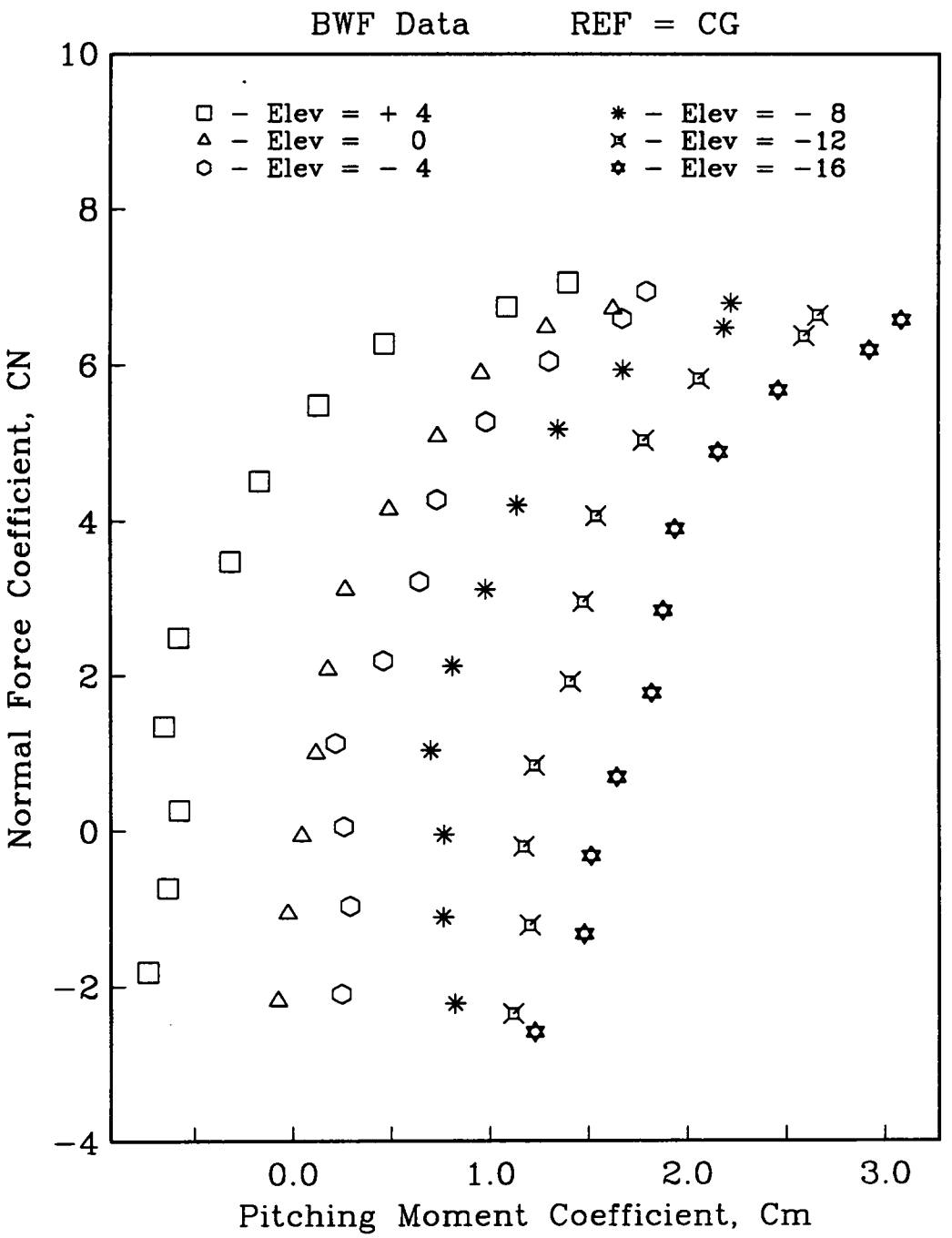

Figure 31b: CN vs Cm Elevator Deflection B2F1Be0

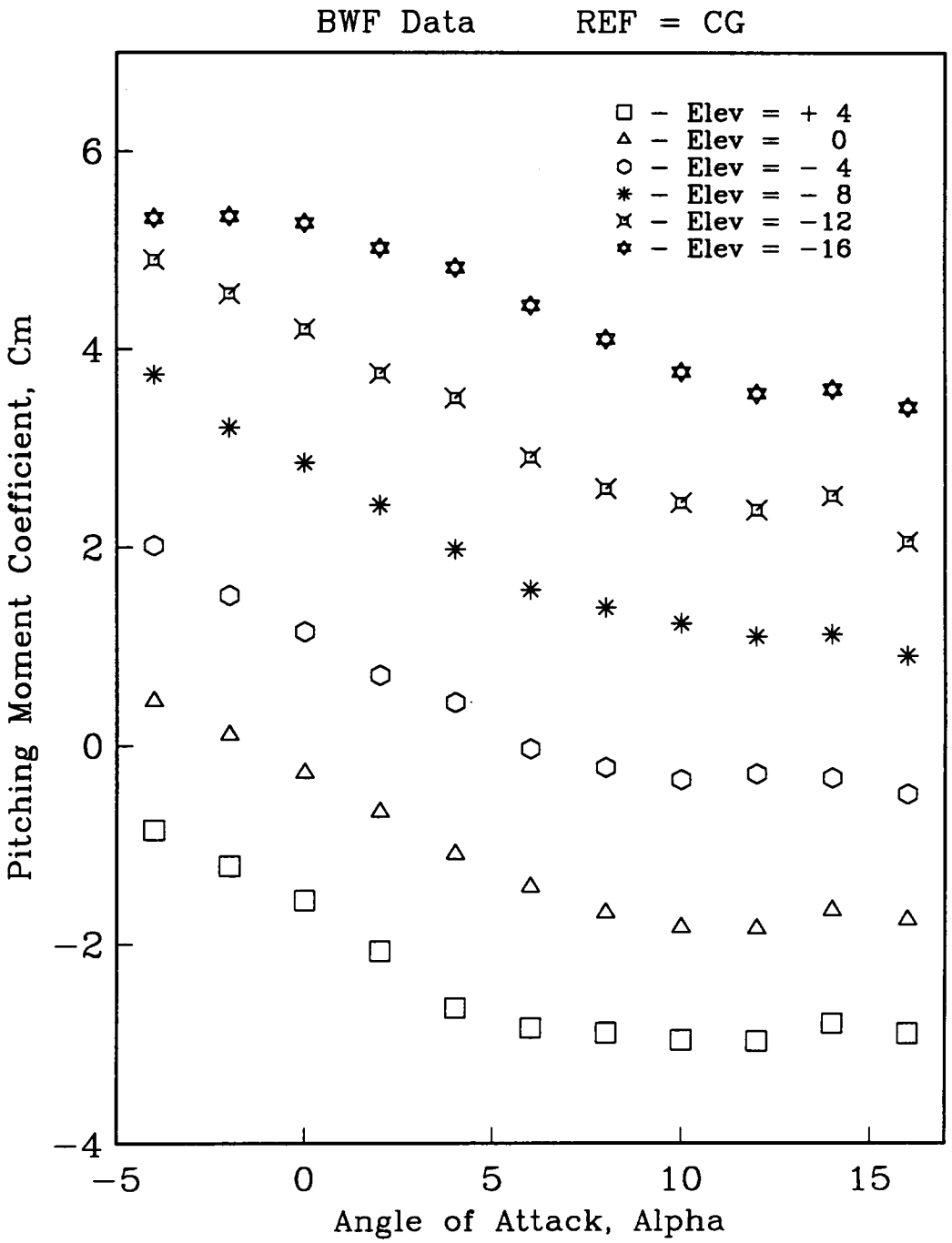

Figure 32a: Cm Elevator Deflection B1F2Be0

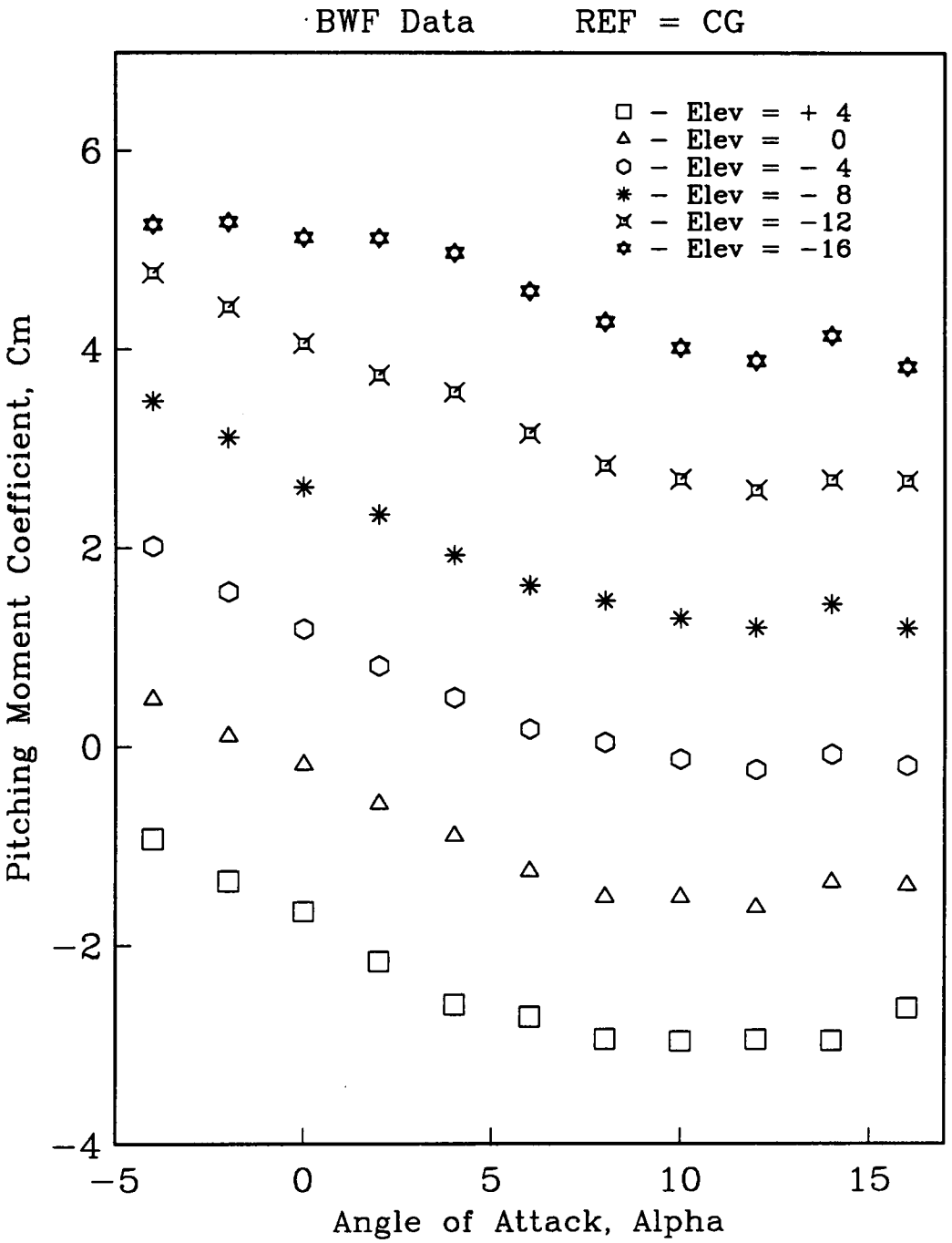

Figure 32b: Cm Elevator Deflection B2F2Be0

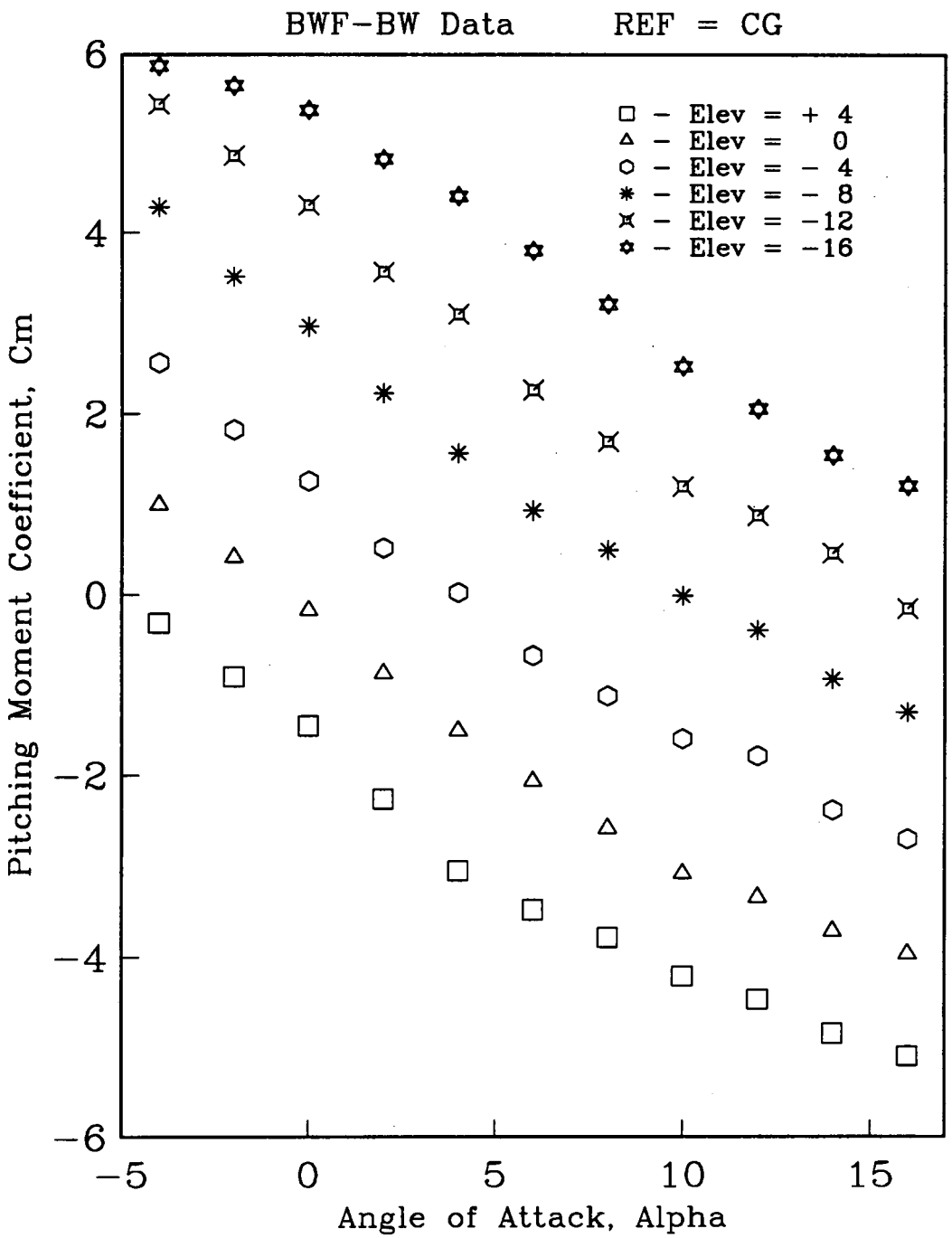

Figure 33a: Cm Fin Effectiveness B1F2Be0

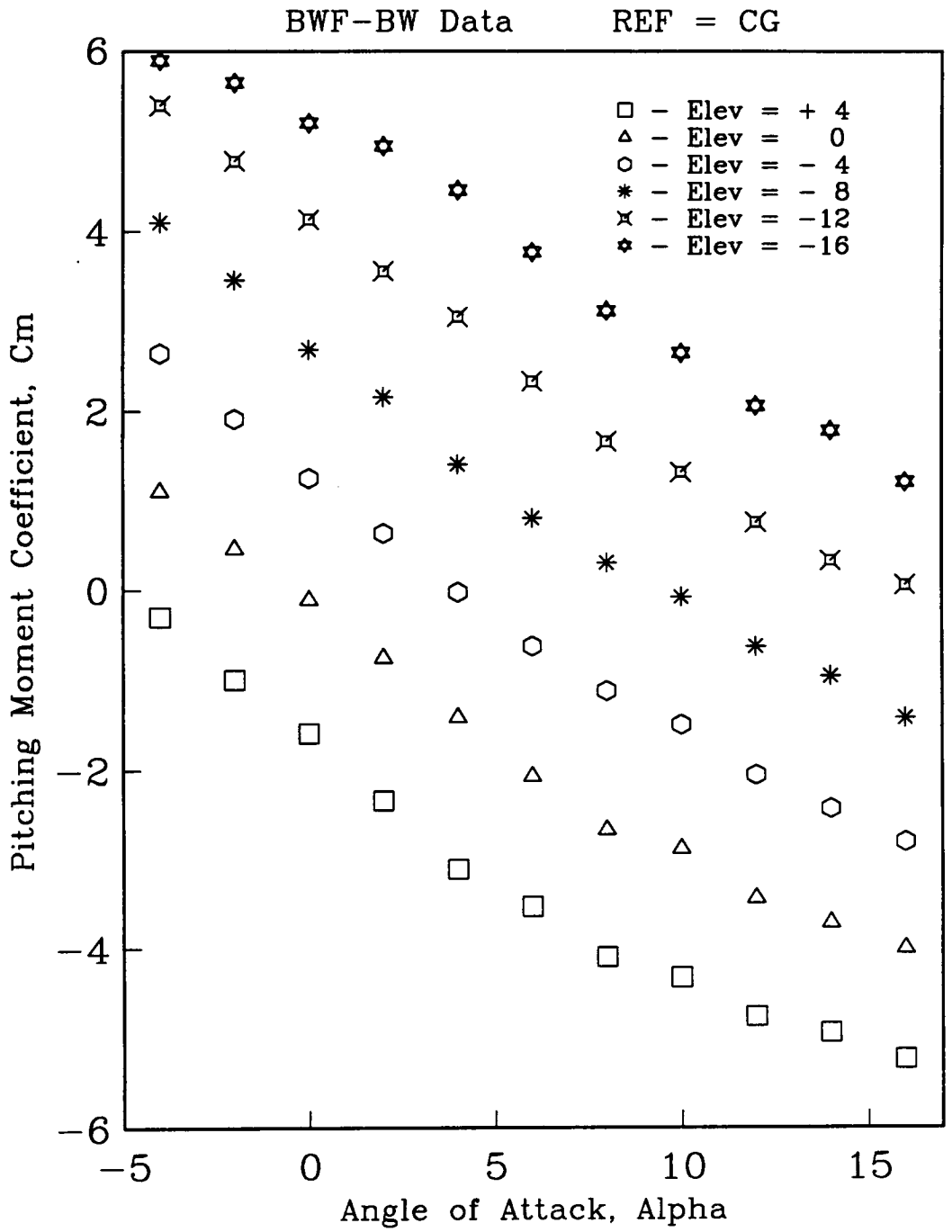

Figure 33b: Cm Fin Effectiveness B2F2Be0

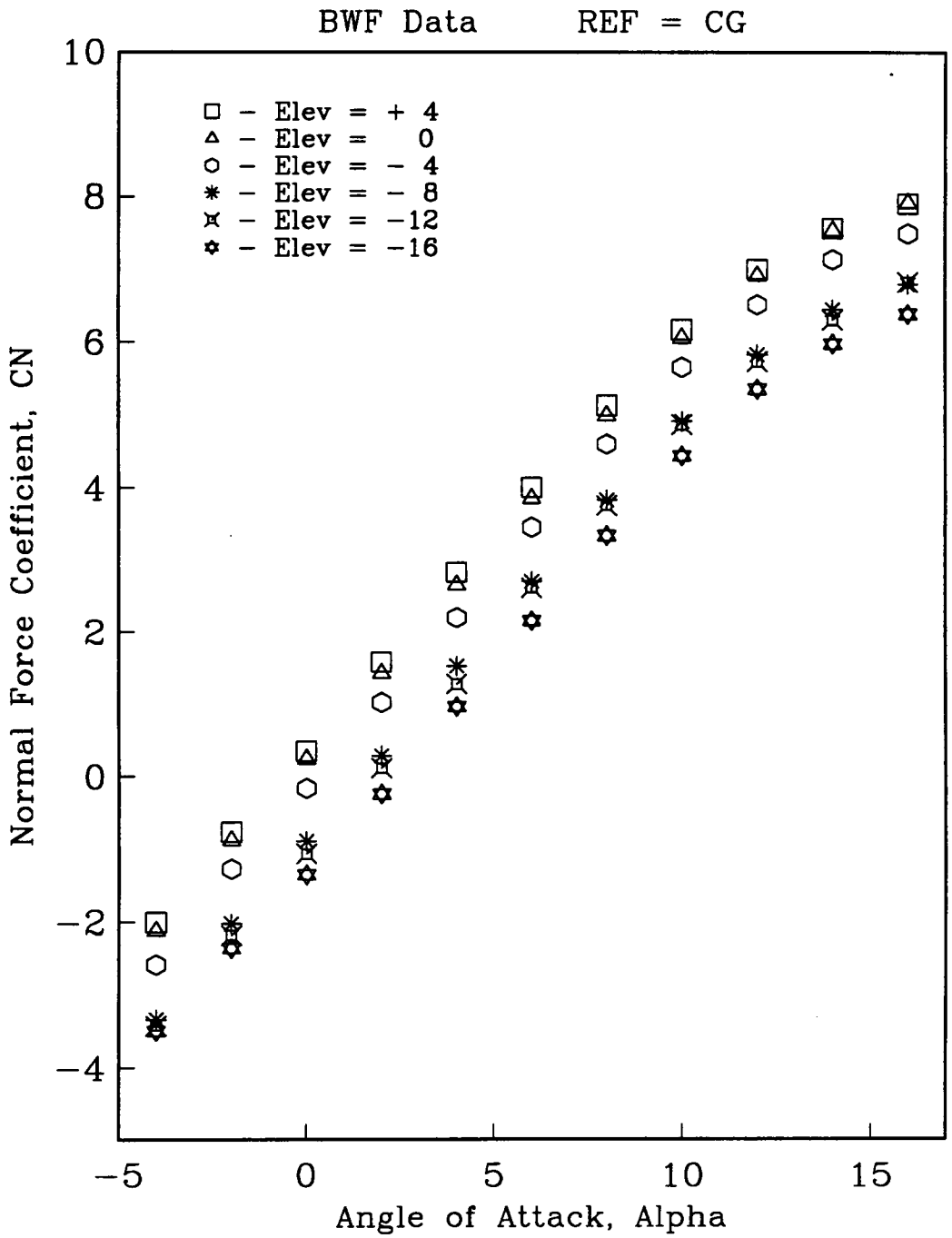

Figure 34a: CN Elevator Deflection B1F2Be0

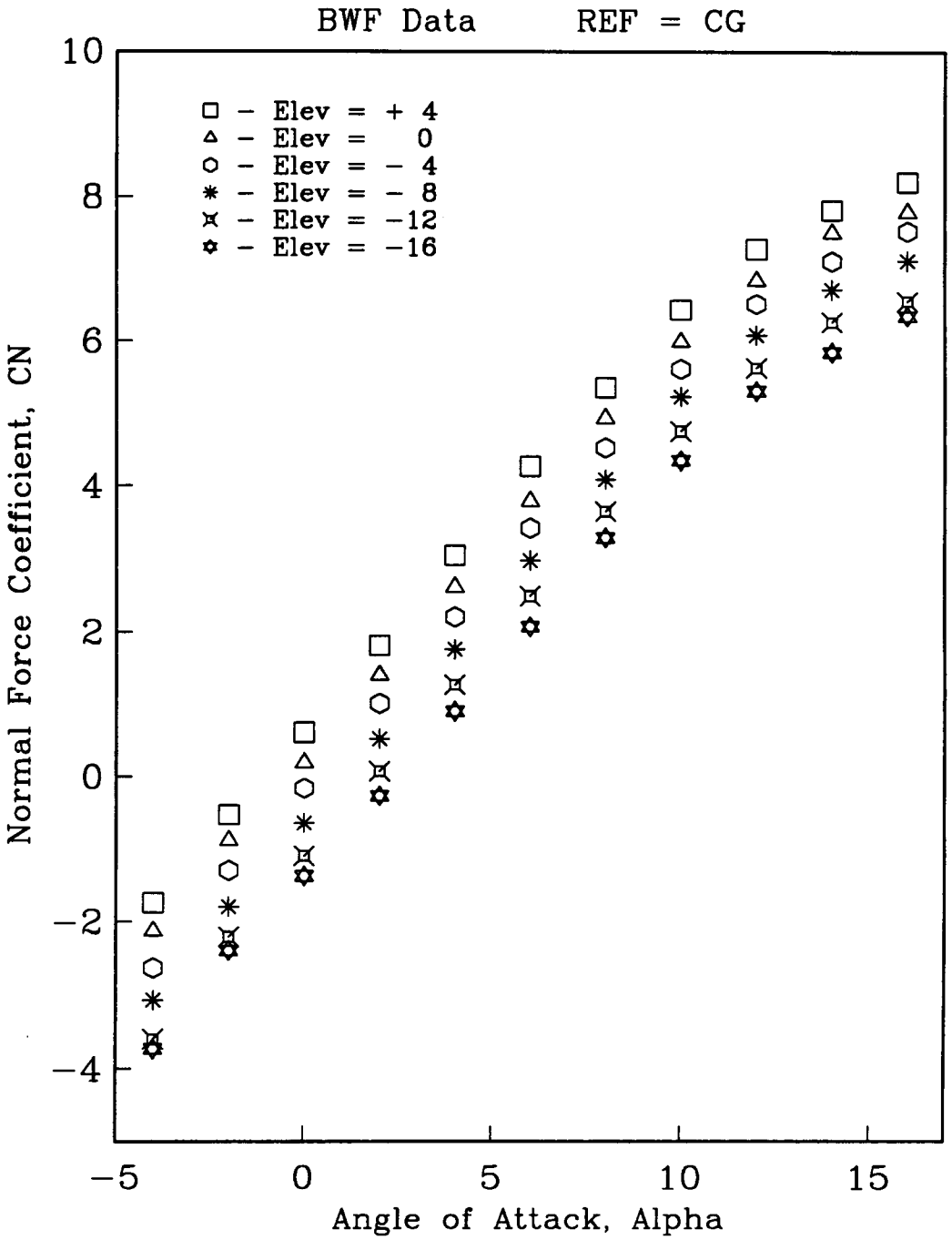

Figure 34b: CN Elevator Deflection B2F2Be0

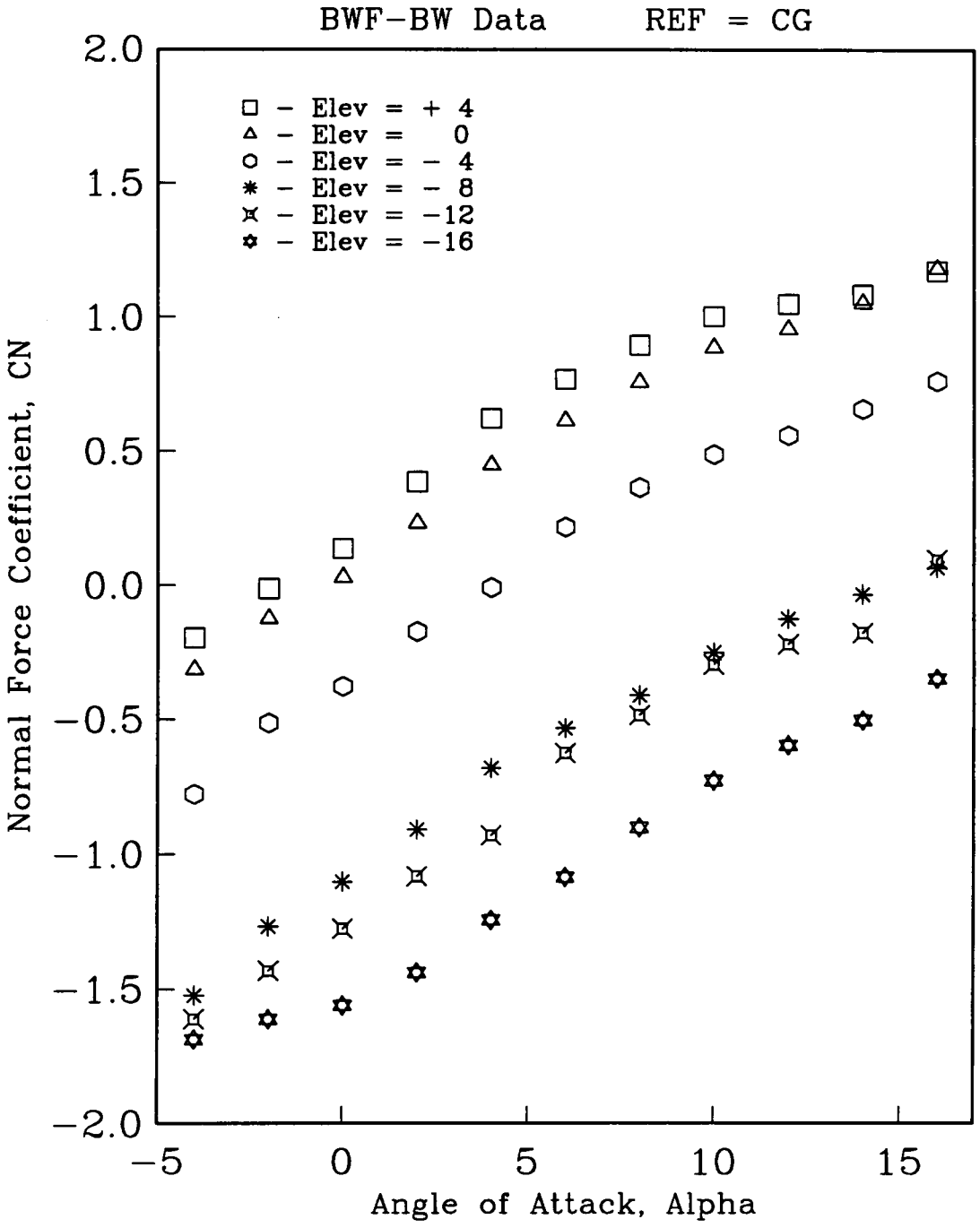

Figure 35a: CN Fin Effectiveness B1F2Be0

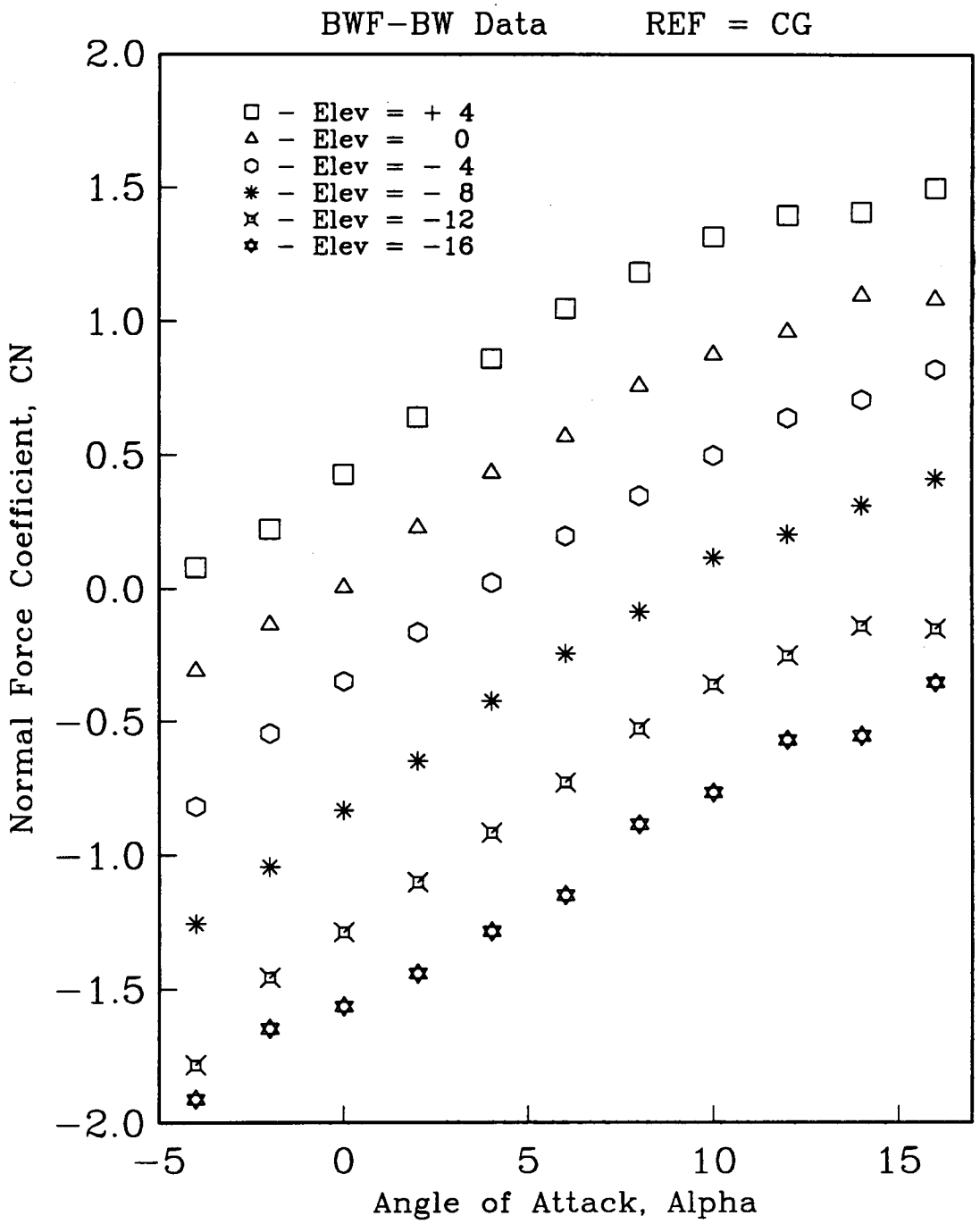

Figure 35b: CN Fin Effectiveness B2F2Be0

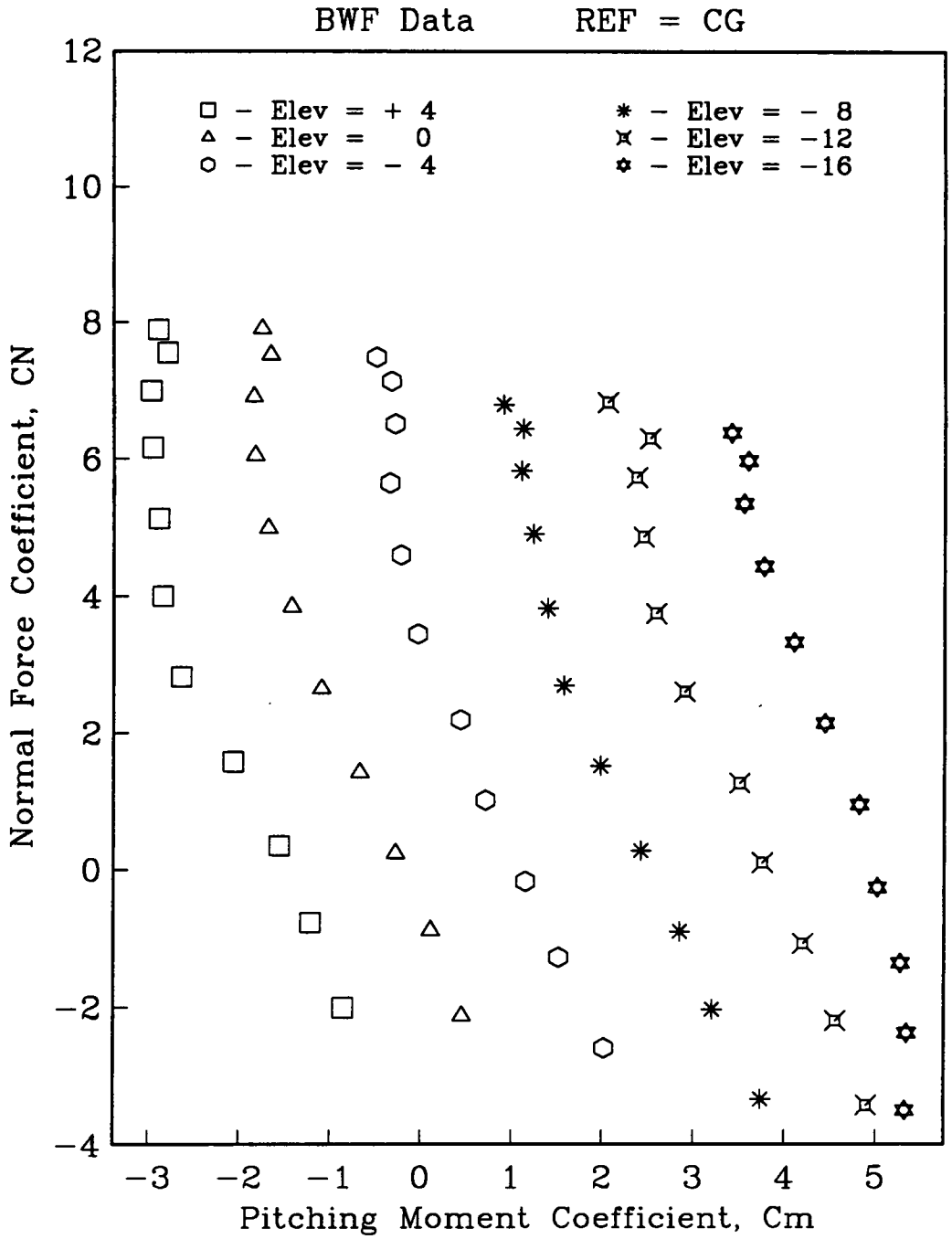

Figure 36a: CN vs Cm Elevator Deflection B1F2Be0

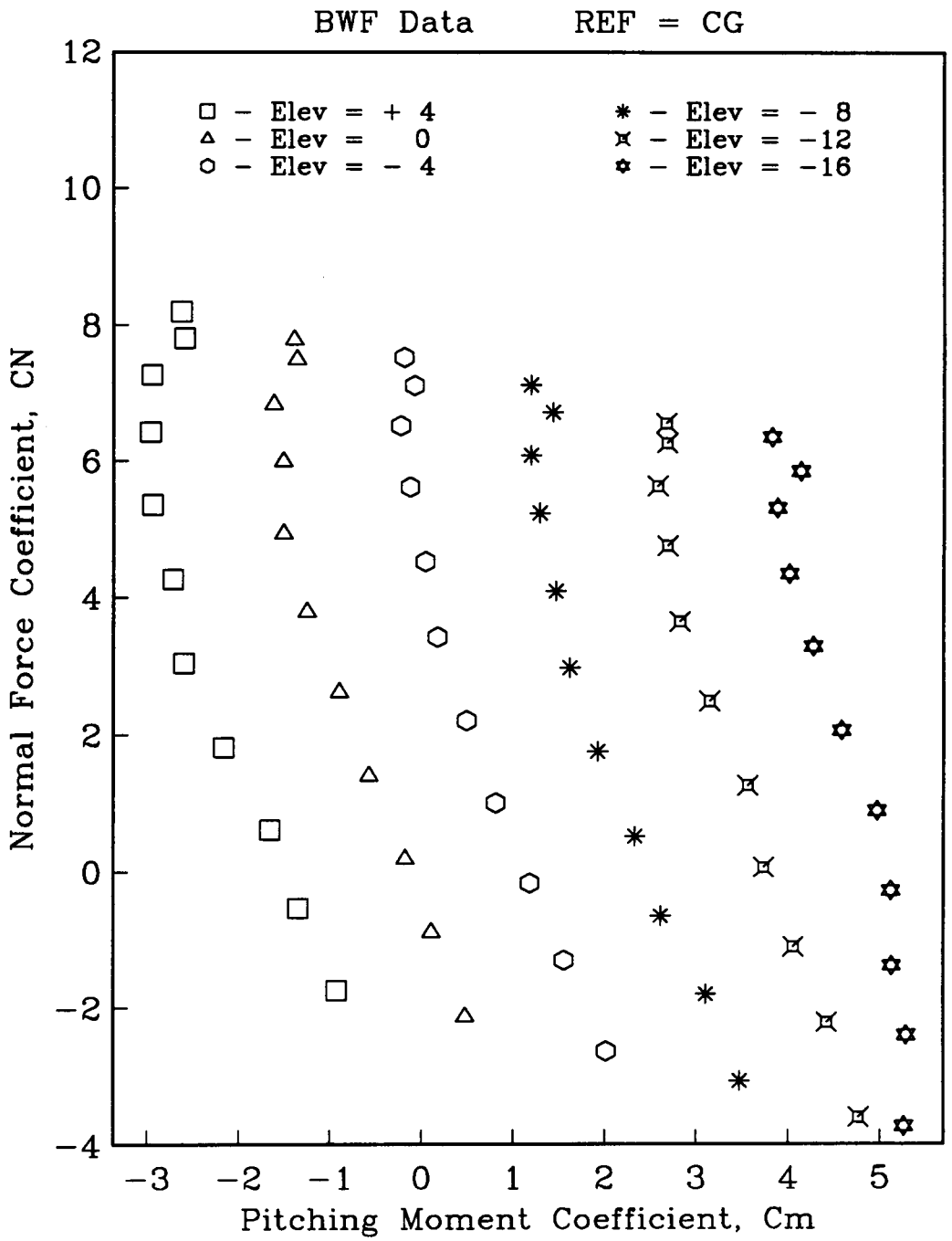

Figure 36b: CN vs Cm Elevator Deflection B2F2Be0

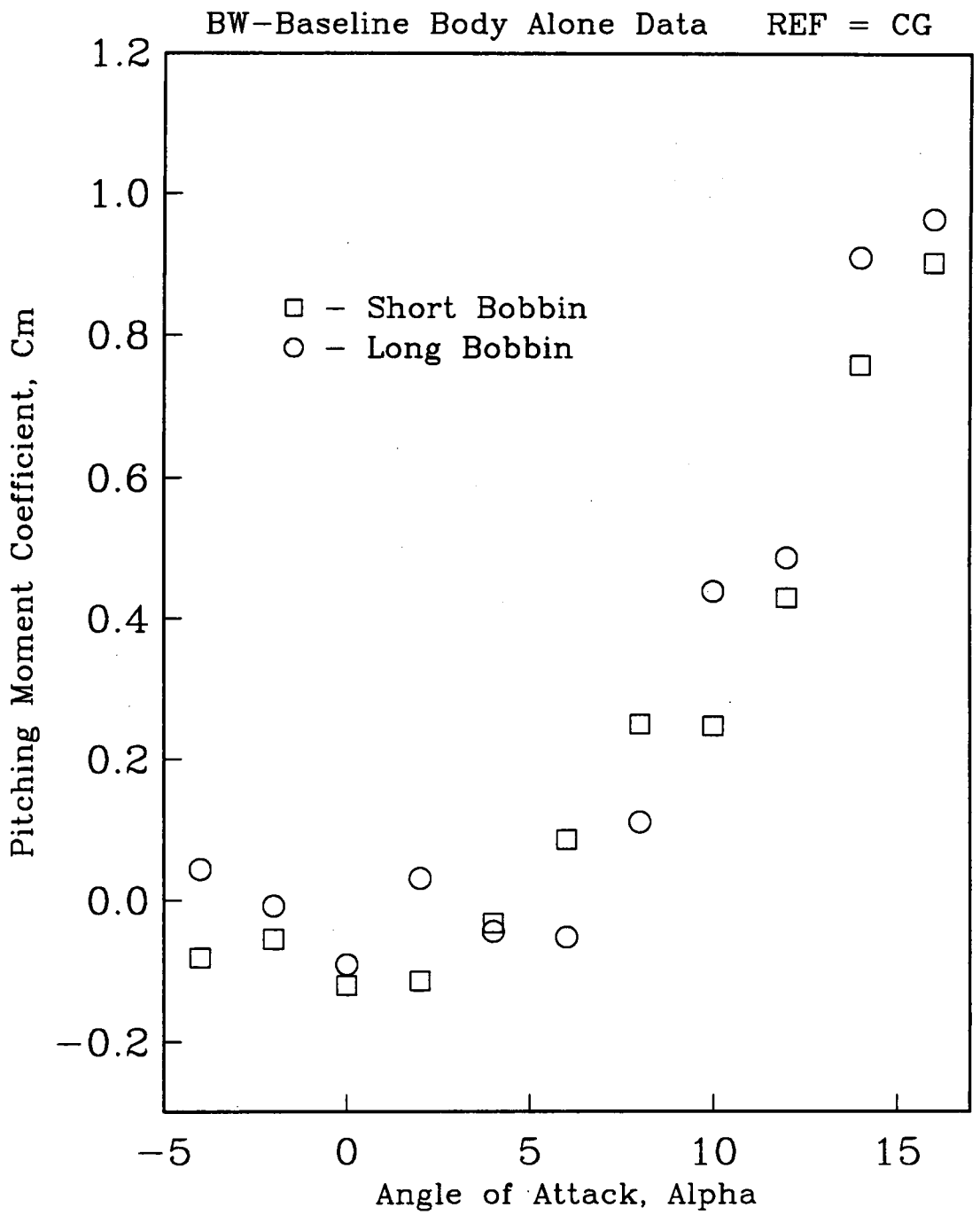

Figure 37a: Cm Wing Effectiveness

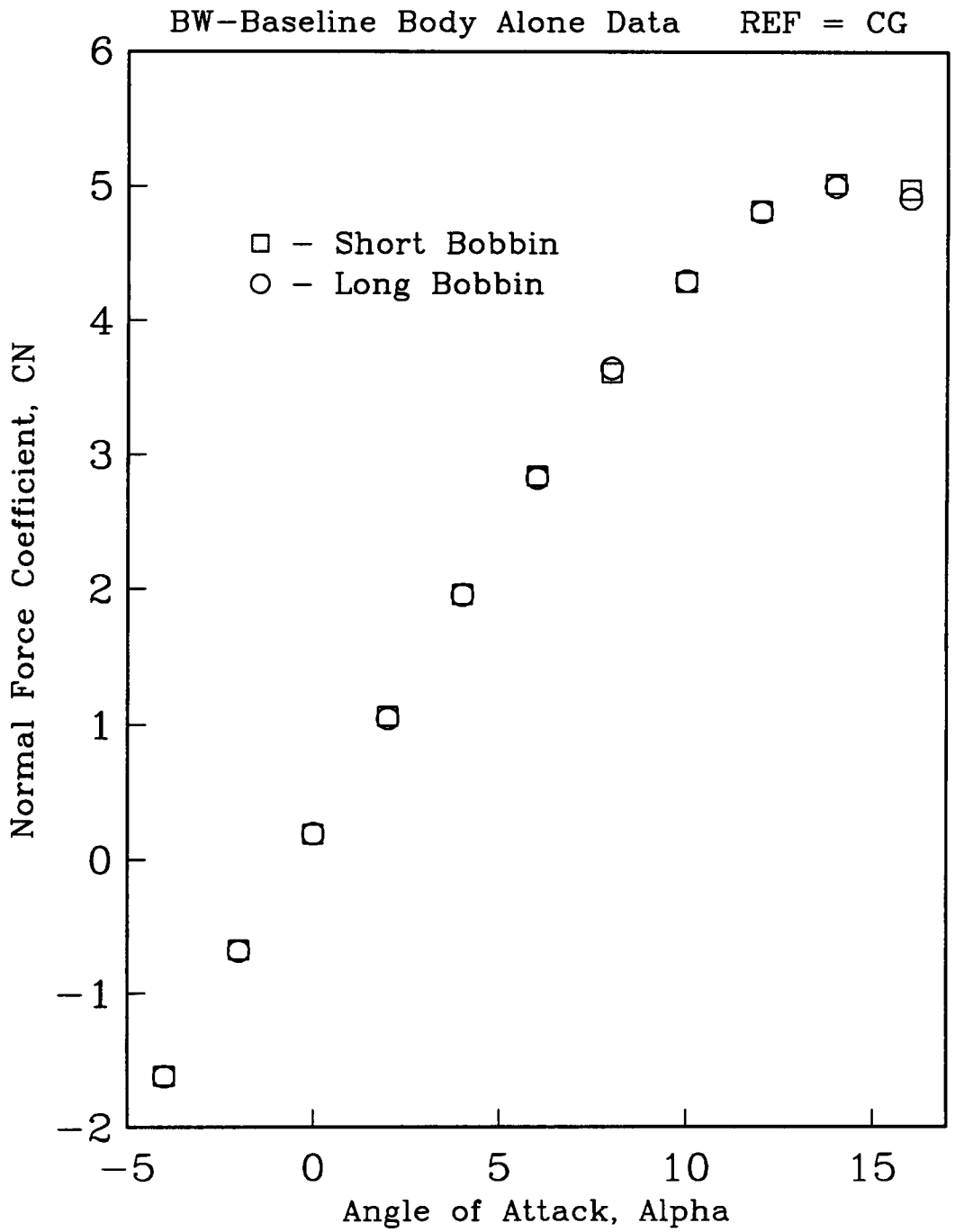

Figure 37b: CN Wing Effectiveness

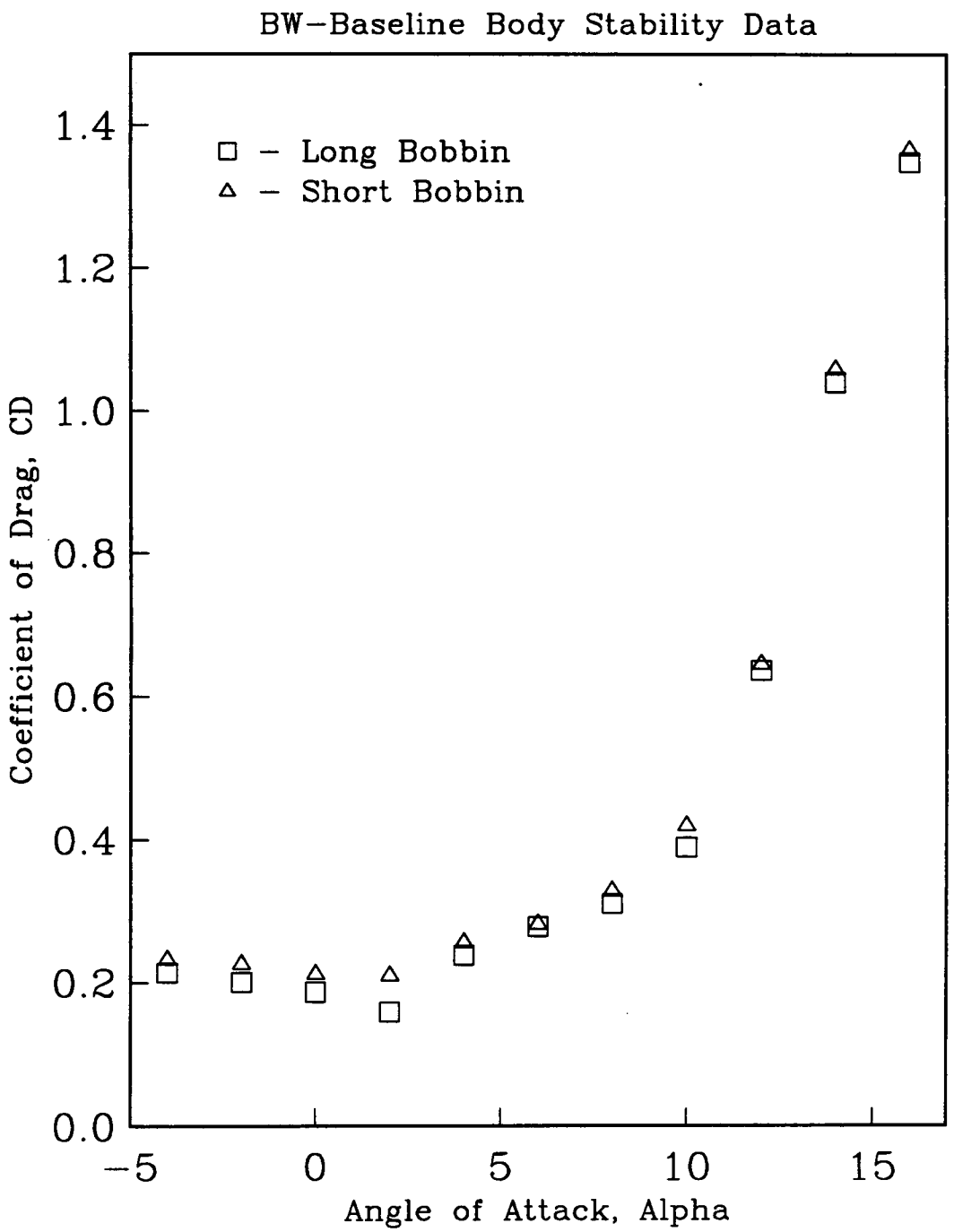

Figure 38a: CD Wing Effectiveness

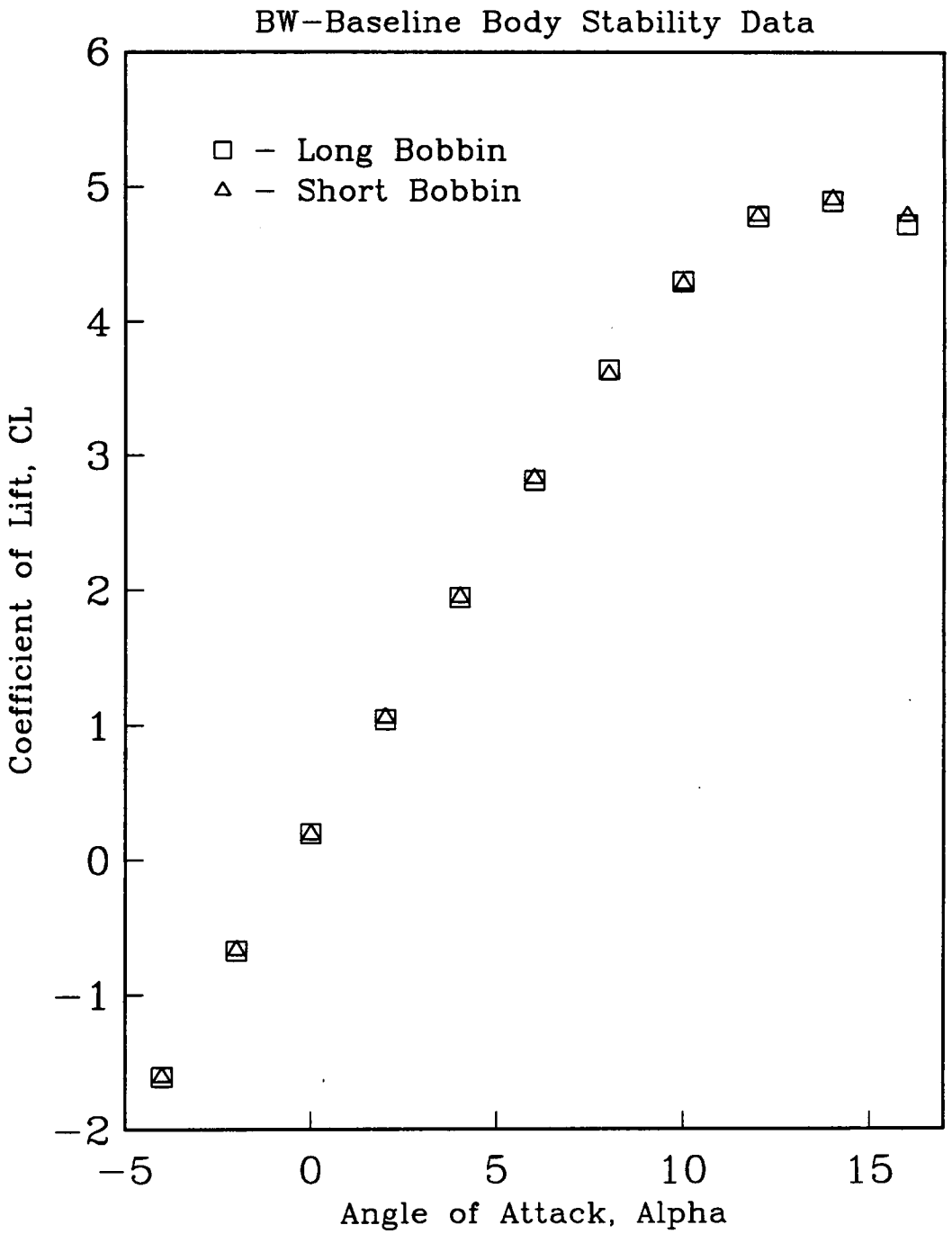

Figure 38b: CL Wing Effectiveness

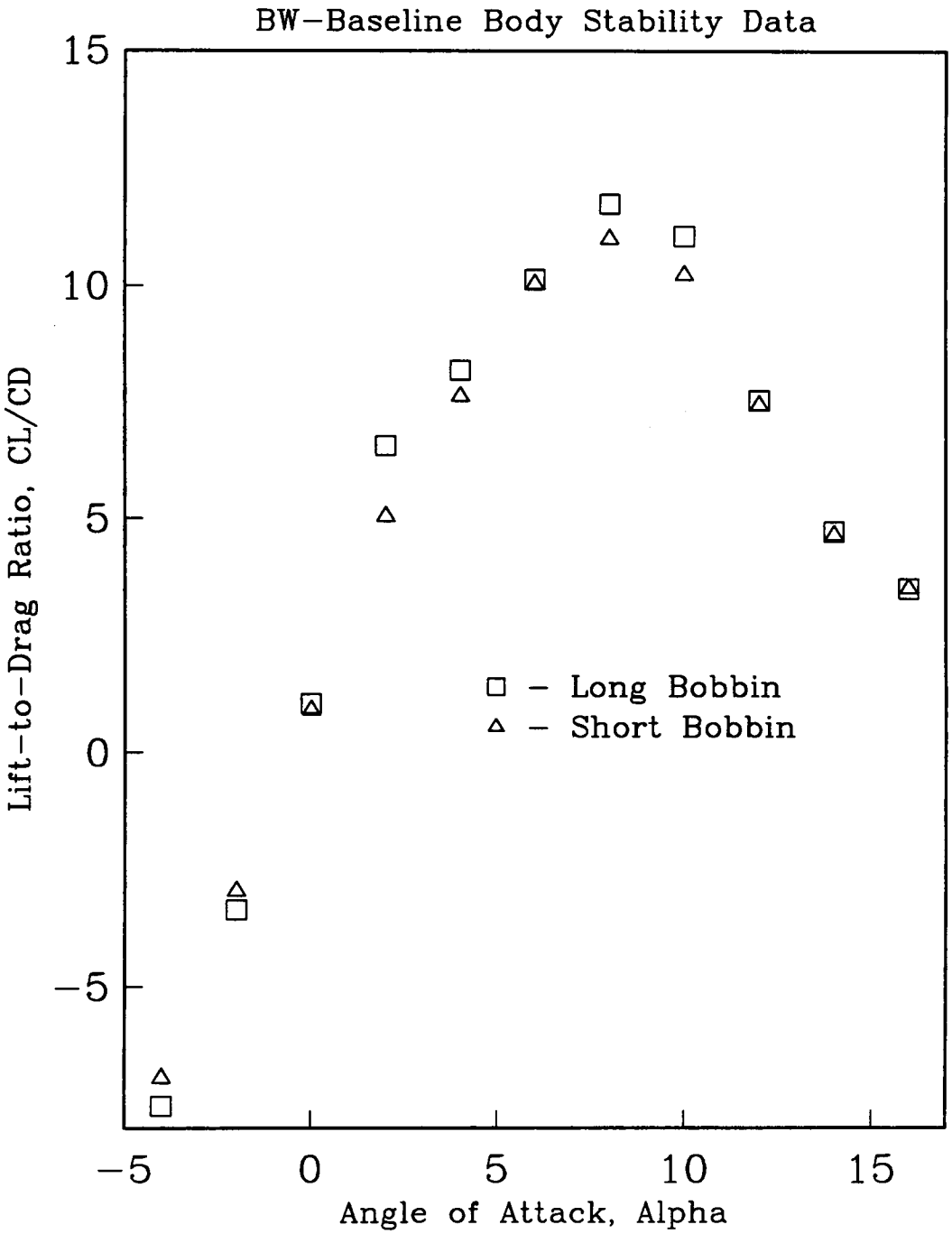

Figure 38c: CL/CD Wing Effectiveness

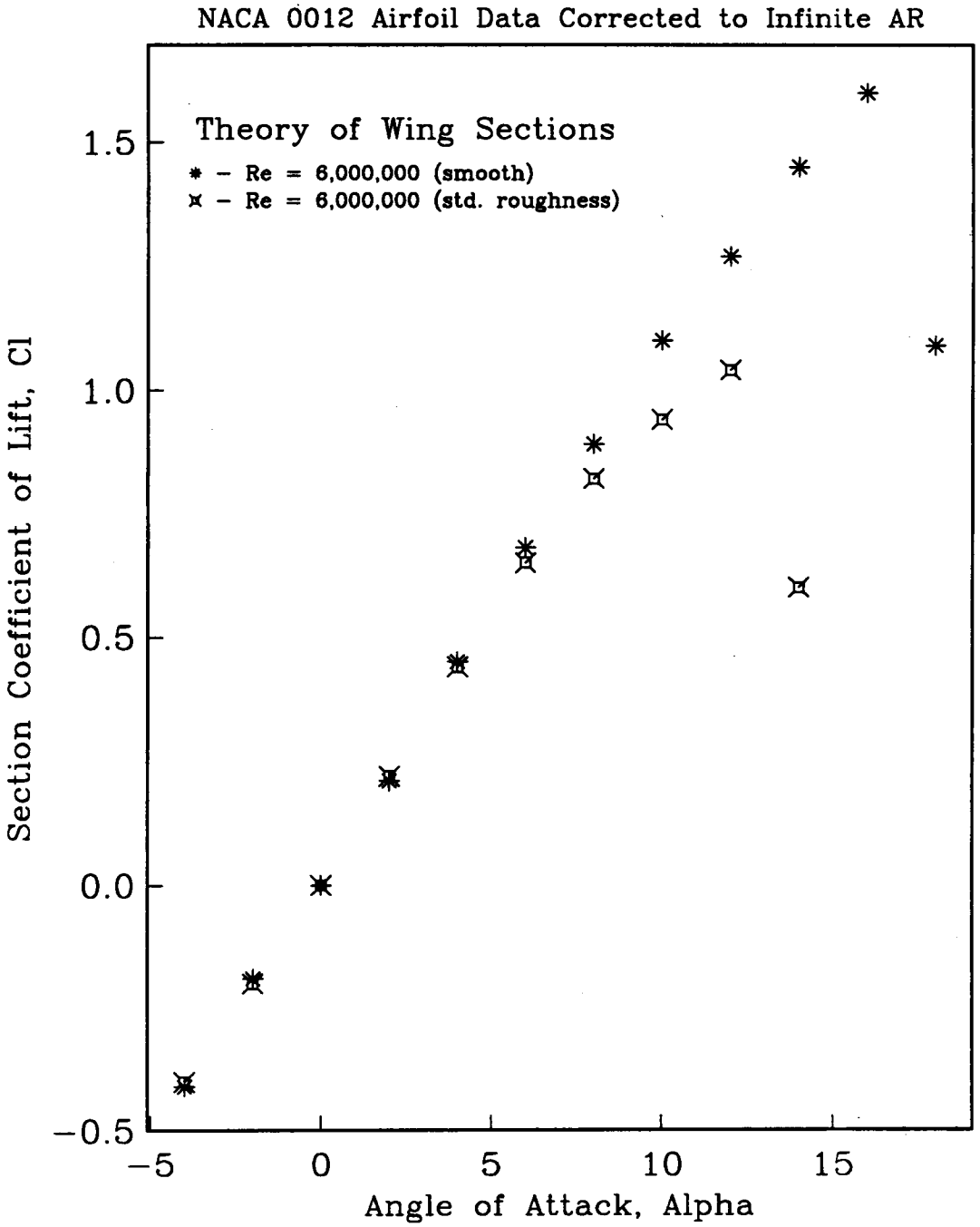

Figure 39: Effect of Airfoil Surface Roughness

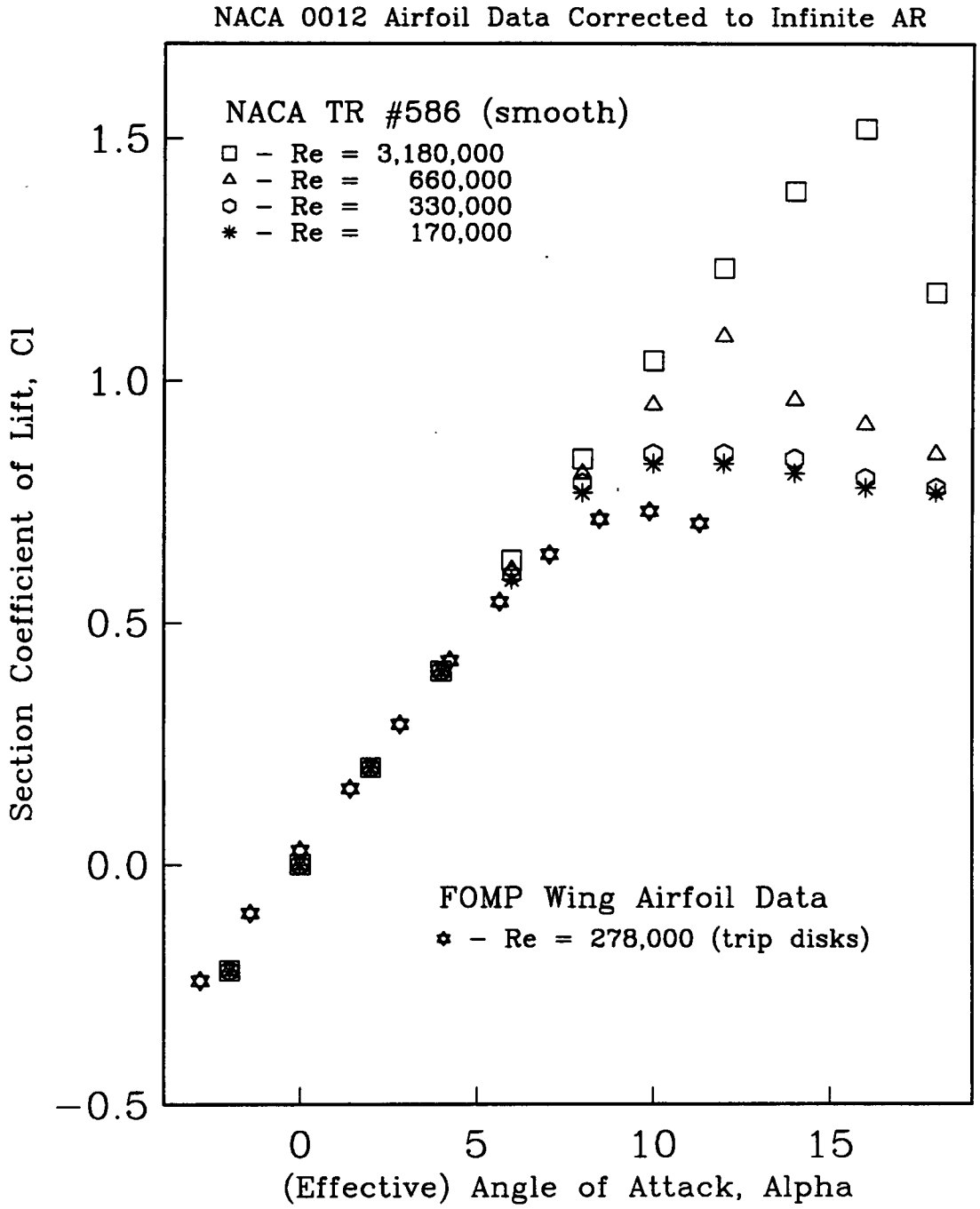

Figure 40: Wing Airfoil Performance

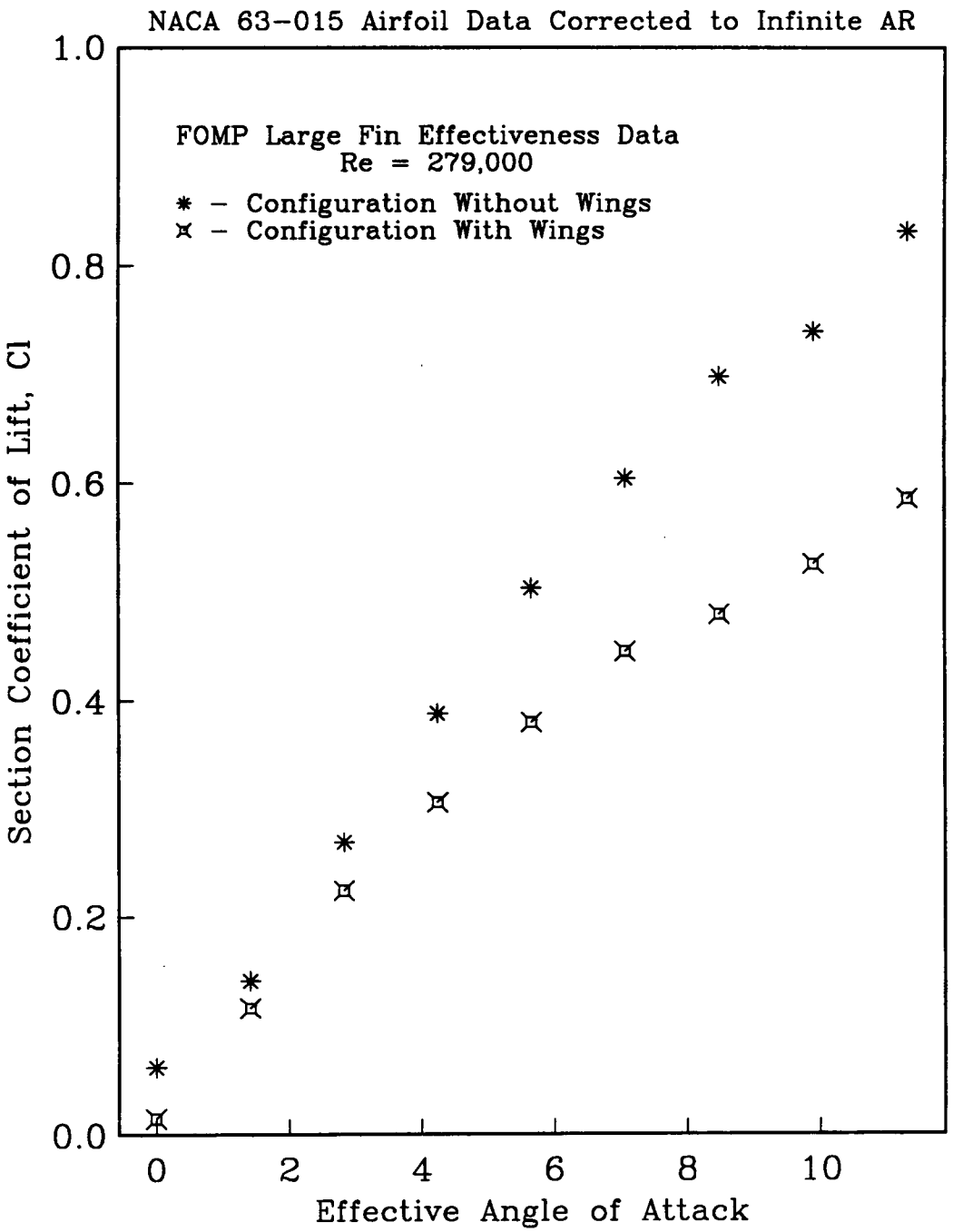

Figure 41: Effect of Wing Downwash on Fins

REFERENCES

[1] Ayers, Theodore G. "Review of the 1980 Wind Tunnel / Flight Correlation Panel." Wind Tunnel / Flight Correlation - 1981: NASA Conference Publication 2225. L. Wayne McKinney and Donald D. Baals (eds.) November, 1981.

[2] Cronvich, L.L. Tactical Missile Aeodynamics: Progress in Astronautics and Aeronautics (Vol. 104). Hemsch and Nielsen (eds.)

[3] Abbott, Ira H. and Albert E. Von Doenhoff. Theory of Wing Sections, pp. 143-148. Dover Publications, Inc. New York, 1959.

[4] Hooker, Ray W. "The Aerodynamic Characteristics of Airfoils as Affected by Surface Roughness." NACA Technical Note #457, April, 1933.

[5] Bertin, John J. and Michael L. Smith. Aerodynamics for Engineers, pp. 203-204. Prentice-Hall, Inc. Englewood Cliffs, New Jersey, 1979.

[6] Lowry, John G. and Edward C. Polhamus. "A Method for Predicting Lift Increments Due to Flap Deflection at Low Angles of Attack in Incompressible Flow." NACA Technical Note #3911, 1957.

[7] Jacobs, Eastman N. and Albert Sherman. "Airfoil Section Characteristics as Affected by Variations of the Reynolds Number." NACA Technical Report #586, 1937.

The vita has been removed from the scanned document